Planetary obliquity evolution: excited retrograde rotators and tidal resonant encounters

*Presented in Partial Fulfillment of
the Requirements for the Degree of*

Doctor of Philosophy

with a Major in

Physics

in the

College of Graduate Studies

University of Idaho

by

Steven M. Kreyche

Major Professor
Jason W. Barnes, Ph.D.

Committee
Matthew M. Hedman, Ph.D.
Brian K. Jackson, Ph.D.
Marty F. Ytreberg, Ph.D.

Department Administrator
John R. Hiller, Ph.D.

December 2022

Abstract

The search for extraterrestrial life along with our desire to understand the necessary conditions for the development of life are large motivators in the field of astronomy. Although the Earth remains as our sole data point, it seems overwhelmingly likely that either other Solar System bodies or distant exoplanets had, have, or will have the capacity to host life of their own. Nonetheless, the assessment of a world's potential for habitability is a complex problem that requires thorough study of many contributing aspects. One key aspect is the value and evolution of a planet's obliquity, or axial tilt, which sets the nature of its seasons and long-term climate by governing the distribution of solar flux across its surface. Although we enjoy a pleasant climate thanks to the Earth's stable moderate obliquity, other planetary bodies may be either even better off or severely challenged in comparison. In dissertation, I help build toward a more complete picture of habitability by studying planetary obliquity evolution with the use of numerical simulations of planetary systems. Beginning with Chapter 1, I provide a brief background of the dynamics that drive obliquity evolution and describe previous work that establishes our current understanding moving forward. In Chapter 2, I discuss a threatening secular spin-orbit resonance that can destabilize the obliquities of retrograde rotators (planets with obliquities greater than 90 degrees). Next, in Chapter 3 I introduce SMERCURY-T, a tool that allows for the study of planetary obliquity evolution under the influence of tidal forces. Finally, in Chapter 4 I apply SMERCURY-T to study the tidal obliquity evolution of a moonless Earth and a potentially habitable early Venus. Each of these chapters provides wider contributions past their individual results by urging direction to future studies, releasing publicly available software, or identifying trends and process that may be important to the obliquity evolution of extrasolar planets. These findings can ideally be applied to such exoplanet systems in the future once further our capability to detect and characterize their spin states.

Acknowledgements

My completion of this thesis required the support and encouragement of many people including my graduate committee members, coauthors, and fellow graduate students. I thank my graduate committee for the invaluable part that they played in teaching and guiding me as I developed the necessary critical thinking and research skills to grow as a scientist. First and foremost, I thank my major professor, Dr. Jason W. Barnes, who taught me useful and practical knowledge both in and outside of the classroom as a close mentor and friend. I appreciate his selective hands-off mentoring approach which fostered my development and built my confidence as an independent researcher, while he knew to step in and help at the right times when I needed it. Dr. Matthew M. Hedman was often like a secondary research advisor to me whom I thank for the many engaging science conversations that we had in addition to his frequent willingness to provide advice or help. I thank Dr. Brian K. Jackson, my committee member and former undergraduate research advisor, whose helpfulness and encouragement laid the foundation for my research career. I thank Dr. Marty F. Ytreberg for his memorable instruction in the classroom and added depth of expertise and experience to this committee.

I would also like to thank the various coauthors involved with my published work including Dr. Billy L. Quarles, Dr. Jack J. Lissauer, and Dr. John E. Chambers, who provided codes and useful feedback that helped shape the direction of this dissertation. Finally, I extend a huge thanks to my close friends and graduate student peers including Jonathan Barnes, Marshal Boyland, Ross Miller, and Sanjoy Saha, who I bonded with through mutual suffering from homework and studying while finding plenty of time for some good fun and laughs. Joseph A'hearn, Michael Heslar, William Miller, and Himanshi Sharma helped further by providing codes or helpful feedback for early versions of my work.

Dedication

I dedicate this work to my wife, family, and friends. My wife, Danielle, continuously provided a tremendous amount of support and sacrifice over the years while proofreading my rough drafts, hearing my ideas, and sharing my stress about deadlines. I am truly appreciative of both of my parents, Debra and Paul, and sister, Caitlin, for fostering a home as I grew up that enabled me to pursue my interests and grow into the person that I wanted to be. I am also thankful for the support and encouragement that I received from the new additions to my family including my parents-in-law, Lisa and Nick, and brothers-in-law, Mike and Nicholas, as well from my lifelong friends and brothers to the end, Daniel and Garret.

TABLE OF CONTENTS

List of Tables

LIST OF FIGURES

CHAPTER 1

General Introduction

1.1 PLANETARY OBLIQUITY AND CLIMATE

The possibility of discovering extraterrestrial life largely motivates the study of extrasolar planets. Judging the habitability of these worlds requires the consideration of a multitude of factors. Aside from the basic requirement that a planet's orbit must reside within the habitable zone (HZ), the region around a star at which liquid water can exist on the planet's surface, the nature of the planet's obliquity, or axial tilt, is fundamental to habitability. Planetary obliquity affects the climate of the planet by governing the distribution and seasonal variation of its incoming solar flux. Therefore it is important to know both the value of the planet's obliquity and how it evolves over time. Additionally, we can use this knowledge to gain insights or make predictions for the spin dynamics of planetary bodies in the Solar System and beyond.

Formally, planetary obliquity, ϵ, is the angle between a planet's orbital and rotational angular momentum vectors. Therefore, with respect to the planet's direction of orbital motion, obliquity values $< 90°$ correspond to prograde rotation while obliquity values $> 90°$ correspond to retrograde (backwards) rotation. The Solar System is host to planets possessing a variety of obliquity values spanning nearly the entire $180°$ space. Terrestrial planet obliquities are likely initially isotropic in distribution, randomly decided from collisions in the protoplanetary disk after formation (Dones and Tremaine, 1993; Lissauer *et al.*, 1997; Miguel and Brunini, 2010), see however Lissauer and Kary (1991). However, recent findings suggest that processes such as planet-disk interactions could influence planetary obliquity early on (Millholland and Batygin, 2019; Su and Lai, 2020).

There are unique consequences for each value of obliquity. The Earth's relatively low obliquity of $\sim 23.5°$ means that its equator receives the most annually-averaged illumination while its poles receive very little. Low-obliquity worlds have the poten-

tial to enter snowball states, in which ice envelops the entire planet similar to the historic snowball Earth episode (Hoffman *et al.*, 1998). On the other hand, planets with obliquities near 90° have poles that experience extreme contrasts in solar flux over the course of an orbit, while their equators actually receive the least amount of illumination as seen in Figure 1 of Lissauer *et al.* (2012). High obliquity worlds have a severe seasonality that can generally lead to warmer climates (Kang, 2019), however see He *et al.* (2022). This seasonality could act to stave off snowball states (Spiegl *et al.*, 2015; Colose *et al.*, 2019) or produce equatorial ice belts (Kilic *et al.*, 2018). Olson *et al.* (2020) and Barnett and Olson (2022) found that oceans of high obliquity worlds may have more efficient nutrient recycling processes that would benefit potential biological activity near the surface. Ultimately the fate of a planet's climate depends on the configuration and properties of the planetary system, where studies that incorporate energy balance models show that any value of obliquity has the potential to provide habitable conditions (Williams and Kasting, 1997; Williams and Pollard, 2003; Kilic *et al.*, 2017; Kane and Torres, 2017; Guendelman and Kaspi, 2019; Dong *et al.*, 2019; Colose *et al.*, 2019).

1.2 OBLIQUITY VARIATIONS AND SPIN-ORBIT RESONANCE

Since the value of obliquity affects planetary climate, changes in the obliquity drive changes in the climate over time. In most cases, the expectation is that rapid large swings in obliquity would likely be harmful to a planet's habitability, acting as jolts to its climate. For instance, the large obliquity variations of Mars contributed to its atmospheric collapse (Head *et al.*, 2004; Head *et al.*, 2005; Forget *et al.*, 2013). Although muted compared to Mars, the periodic $\sim 2.4°$ shift of the Earth's spin axis drives its glacial cycles and Ice Ages (Milanković, 1998). Nonetheless, Armstrong *et al.* (2014) found that in special circumstances extreme obliquity variations can be helpful, in that they can push the outer limit of the HZ outwards by staving off snowball states. Later, Deitrick *et al.* (2018b) applied a more robust model and argued that fast and large variations in a planet's rotational and orbital properties can actually do the opposite, and sometimes lead to global glaciation.

Many processes contribute to alter a planet's obliquity over time. Constant torques exerted on a planet's equatorial bulge by its planetary neighbors in addition to the regular precessional motion of the planet's orbit plane set a range of small regular obliquity variations. On the other hand, a planet can experience large obliquity variations of many tens of degrees if it enters into a secular spin-orbit resonance. Such a resonance occurs when a planet's spin-axis precession becomes commensurate with a driving eigenfrequency of its orbital precession (Colombo, 1966; Peale, 1969; Henrard and Murigande, 1987). Considering the working parts that contribute to this resonance, rhythmic gravitational tugs from neighboring planets drive orbital precession while torques from the planet's star and moons fuel its spin precession. The rate of a planet's spin precession obeys

$$\dot{\psi} = \frac{\alpha \cos \epsilon}{\left(1 - e^2\right)^{\frac{3}{2}}} \tag{1.1}$$

where *epsilon* is the obliquity and e is its orbital eccentricity. This relationship implies that the spin-precession rate is larger for smaller values of obliquity and bigger values of eccentricity. In the case of a moonless planet, the precession constant, α, goes as

$$\alpha \approx \frac{3n^2}{2\omega_p} \frac{J_2}{\overline{C}} \tag{1.2}$$

Here n is the planet's mean motion, ω_p its spin rate, J_2 its oblateness coefficient, and $\overline{C}$ is its normalized polar moment of inertia (this expression is approximate, based on the assumption that the planet's dynamical ellipticity is roughly proportional to $\omega_p{}^2$) (Laskar and Robutel, 1993b; Li and Batygin, 2014; Quarles et al., 2020).

The resultant obliquity variations of this spin-orbit resonance depend on the amplitude of the participating orbital frequency in addition to the planet's proximity to the resonance center. Provided that a planet resides within a spin-orbit resonance, its resonant angle, $\sigma = \psi + \phi$, will typically librate about 0 (the stable Cassini States 1 and 2 or the unstable Cassini State 4) or 180 degrees (Cassini State 2, stable), where ψ is the planet's spin precession angle that defines the azimuthal orientation of the planet's spin vector and ϕ is the phase angle of the orbital precession mode (Deitrick et al., 2018a; Saillenfest et al., 2019; Su and Lai, 2020). Furthermore, in the case that the

widths of multiple spin-orbit resonances overlap, a planet's spin axis can be subject to chaotic evolution in which its obliquity swings across a wide range of values. Mars is the poster child for this chaotic behavior, as its obliquity swings from $\sim 0 - 60°$ (Laskar and Robutel, 1993b; Touma and Wisdom, 1993; Laskar *et al.*, 2004b; Li and Batygin, 2014). The Earth would suffer a similar fate if not for the Moon's help in speeding up the Earth's spin-axis precession enough so that the Earth peacefully resides outside of the chaotic region (Laskar *et al.*, 1993a, 2004a; Brasser and Walsh, 2011).

1.3 DYNAMIC RESONANT ENCOUNTERS AND THE SOLAR TIDAL TORQUE

The status of a planet's presence within a spin-orbit resonance can change with time. For instance, although the Earth rests easy now, it may have crossed a high-order resonance just a few million years ago (Laskar *et al.*, 1993a, 2004a). Change can be brought on by a variety of processes, such as those that shift the location and amplitudes of potentially resonant orbital frequencies. Planetary orbital migration mechanisms are one such way to achieve these shifts (Brasser and Lee, 2015; Vokrouhlický and Nesvorný, 2015; Millholland and Laughlin, 2019). In a similar vein, the works of Saillenfest *et al.* (2020), Saillenfest *et al.* (2021a), and Saillenfest, Melaine *et al.* (2021) studied the past and future influence that satellite migration may have had on the obliquity evolution of Jupiter and Saturn. Millholland and Batygin (2019) and Su and Lai (2020) studied another mechanism in which a shrinking protoplanetary disk could cause sweeping spin-orbit resonances to influence the obliquity distribution of newly formed protoplanets. Another study applied this concept to Uranus's circumplanetary disk to attempt to infer its dynamical history (Rogoszinski and Hamilton, 2020).

Alternatively, a planet can be driven into or out of a spin-orbit resonance by processes that alter its spin precession rate (Equation 1.1). Tidal spin torques are one mechanism that can dynamically shape the fate of a planet's spin state over time by modifying the planet's precession constant, obliquity, or orbital eccentricity. The tidal

friction generated from a system's star pulling on the equatorial bulges of a planet will slowly drive it toward tidal equilibrium, in which its obliquity will typically increase followed by a gradual decline to a small values (the solar tidal torque is initially more efficient at reducing the planet's spin component perpendicular to its orbit plane (Barnes and Fortney, 2003)), while its spin rate undergoes rotation braking until its spin period becomes synchronous with its orbital period (or pseudo-synchronous for eccentric orbits). This journey amounts to a constant decline in a planet's precession constant and consequently its spin-precession rate over time, allowing for opportunities to encounter spin-orbit resonances as time goes on. Tidal spin torques can drive a planet's spin axis to traverse parameter space and undergo scenarios such as spin-orbit resonance crossings, captures, or even traverses of chaotic resonance regions. Since the magnitude of the tidal force decays roughly as r^{-6} with distance, this process is likely especially important for planets in close proximity to their star. The Earth will likely undergo chaotic obliquity variations itself in a few billion years after entering the chaotic zone thanks to its decaying rotation rate (Neron de Surgy and Laskar, 1997a).

1.4 OUTLINE

In this thesis, I organize the following work into subsequent chapters that describe the work of three individual studies. In Chapter 2, I consider a fictitious simple planetary system to demonstrate a special case of a spin-orbit resonance that can excite large obliquity variations for retrograde-rotating planets on eccentric orbits. Then in Chapter 3 I introduce SMERCURY-T, a numerical integrator that I developed to study tidal obliquity evolution and perform several test experiments. Finally, in Chapter 4 I apply SMERCURY-T to study the accelerated tidal obliquity evolution of a moonless Earth and an early Venus in a complex spin-orbit resonance frequency environment. I conclude in Chapter 5.

CHAPTER 2

RETROGRADE-ROTATING EXOPLANETS EXPERIENCE OBLIQUITY EXCITATIONS IN AN ECCENTRICITY-ENABLED RESONANCE [1]

2.1 SUMMARY

Previous studies have shown that planets that rotate retrograde (backwards with respect to their orbital motion) generally experience less severe obliquity variations than those that rotate prograde (the same direction as their orbital motion). Here I examine retrograde-rotating planets on eccentric orbits and find a previously unknown secular spin-orbit resonance that can drive significant obliquity variations. This resonance occurs when the frequency of the planet's rotation axis precession becomes commensurate with an orbital eigenfrequency of the planetary system. The planet's eccentricity enables a participating orbital frequency through an interaction in which the apsidal precession of the planet's orbit causes a cyclic nutation of the planet's orbital angular momentum vector. The resulting orbital frequency follows the relationship $\nu = 2\dot{\omega} - \dot{\Omega}$, where $\dot{\omega}$ and $\dot{\Omega}$ are the rates of the planet's changing longitude of periapsis and ascending node, respectively. I test this mechanism by simulating cases of a simple Earth-Jupiter system, and confirm the predicted resonance. Over the course of 100 Myr, the test Earths with rotation axis precession rates near the predicted resonant frequency experienced pronounced obliquity variations of order $10°$-$30°$. These variations can be significant, and suggest that while retrograde rotation is a stabilizing influence most of the time, retrograde rotators can experience large obliquity variations if they are on eccentric orbits and enter this spin-orbit resonance.

2.2 CONTRIBUTION STATEMENT

For this chapter, I led the investigation by carrying out the numerical experiments, performing the analysis, and writing the report. Jason W. Barnes advised me throughout by providing feedback and guidance on the approach and solution to various components of the study. I shared several useful conversations with Matthew M. Hedman, where he provided useful ideas, feedback, and guidance in analyzing the specific resonance under study. Billy L. Quarles provided useful feedback and contributed code to perform the supplementary semi-analytical obliquity simulations. Coauthors Jack J. Lissauer and John E. Chambers provided useful feedback for revision of the report.

2.3 INTRODUCTION

A planet is a retrograde rotator when it has an obliquity greater than $90°$ and rotates backwards with respect to its orbital motion. A handful of studies considered the obliquity evolution of retrograde rotators. Laskar and Robutel (1993b) studied the obliquity evolution of the Earth under the influence of the Moon, and reasoned that cases of Earths with retrograde obliquities would be expected to be more stable than prograde ones. Later, Lissauer *et al.* (2012) explored the obliquity variations of a moonless Earth and found in agreement, that the retrograde-rotating Earths were generally more obliquity stable. Barnes *et al.* (2016) then explored the case of an early Venus and again reported similar results, with the exception of a long-term pronounced variability for some retrograde rotators. Quarles *et al.* (2019) found that depending on the mutual inclination and orbital precession of the bodies, retrograde rotators in the α Centauri AB binary-star system would likely be especially obliquity stable. Together, these studies have shown that retrograde rotation largely stabilizes obliquity under most circumstances.

In this chapter I explore an exceptional circumstance in which a spin-orbit resonance enabled by a retrograde-rotating planet's orbital eccentricity can drive it to experience significant obliquity variations. Specifically, the planet's eccentricity triggers a complex mechanism that enables a 1:1 secular spin-orbit resonance, in

which the frequency of the planet's rotation axis precession becomes commensurate with an orbital eigenfrequency of the system.

Since orbital eccentricity enables this specific spin-orbit resonance, it is important to discuss the influence that eccentricity has on planetary climate. Conservation of angular momentum requires an eccentric planet to spend more time near its apoapsis (the orbit's furthest point from the primary body) than its periapsis (the closest point to the primary body). At first glance, this relationship seems to imply that significantly eccentric planets should be inhospitable, where a greater amount of time spent further away from their energy source would trigger global glaciation. However, the time averaged solar flux over the course of an orbit actually works out to

$$\langle F \rangle \propto (1 - e^2)^{-\frac{1}{2}} \tag{2.1}$$

This relationship shows that a planet actually receives a larger orbitally-averaged global flux with increasing values of eccentricity (Laskar *et al.*, 1993a), albeit the planet's average equilibrium temperature decreases slightly (Méndez and Rivera-Valentín, 2017). Multiple studies applied energy balance and global circulation models to investigate the viability of eccentric planets as habitable worlds. Williams and Pollard (2002) found that planets up to ~ 0.7 eccentricity could remain habitable even with seasonal departures outside of the HZ. Later studies generally confirmed these findings with the exception of the occurrence of snowball states for the case of planets orbiting stars hotter than the Sun (Dressing *et al.*, 2010; Bolmont *et al.*, 2016). The climate of an Earth-like world could even remain temperate throughout significant eccentricity variations over short timescales, as demonstrated by Way and Georgakarakos (2017). Therefore, we should not necessarily discard eccentric worlds as potentially habitable candidates and instead should study the effects of a planet's orbital eccentricity in conjunction with its obliquity.

In this chapter, I explore the obliquity stability of retrograde rotators, finding that orbital eccentricity can generate large obliquity variations. I begin with Section 2.4, in which I describe the mechanism that affects the obliquity of retrograde rotators. Then

in Section 2.5 I explain my approach to test this mechanism. In Section 2.6, I reveal the results of my frequency analysis and simulations, and discuss their implications. I summarize my results and their implications for habitability in Section 2.7.

2.4 CONCEPTUAL MODEL

Planetary obliquity, ϵ, is the angle between a planet's orbital and rotational angular momentum vectors. Therefore, a change in the orientation of *either* of these vectors will alter a planet's obliquity. Torques exerted on a planet's rotational bulge from its star and neighboring planets can directly change the orientation of the planet's rotational angular momentum vector. On the other hand, changes in a planet's orbital inclination, I, or changes in the its longitude of ascending node, Ω, the position along an inclined orbit at which a planet ascends from below the reference plane to above (Murray and Dermott, 1999), alter the orientation of the planet's orbital angular momentum vector. Aside from the most basic case of a single-planet system, the properties and orientation of a planet's orbit in a multi-planet system evolve over time due to gravitational interactions with neighboring bodies.

Within this section, I first discuss how a planet's rotation axis evolves over time in Section 2.4.1. Then I review the different ways that a planet's orbit can evolve in Section 2.4.2. Finally, Section 2.4.3 describes how these processes can act in conjunction to lead to excitations of the obliquities of retrograde rotators.

2.4.1 *Rotation Axis Evolution*

Two angles fully describe the orientation of a planet's rotational angular momentum vector: the obliquity and the precession angle, ψ. While the obliquity specifies the polar angle between the orbital and rotational angular momentum vectors, the precession angle specifies the azimuthal angle at which the rotational angular momentum lies about the orbital angular momentum vector. Torques exerted on the planet's equatorial bulge by the primary body and/or by potential satellites cause this angle to precess over time. This phenomenon is rotation axis precession, or axial precession. Axial precession acts in the opposing direction to the orbital motion for planets with

prograde obliquities. For planets with retrograde obliquities however, the direction of precession flips, as shown in Figure 2.1, and instead moves in the direction of orbital motion. Following Neron de Surgy and Laskar (1997b), the planetary obliquity, precession constant (α from Equation 1.2), and orbital eccentricity define the rate of the axial precession according to Equation 1.1.

2.4.2 *Orbital Evolution*

Considering the case of a multi-planet system, one way that a planet's orbit evolves over time is by nodal precession. Depicted in panel (a) of Figure 2.1, nodal precession is the process in which the orbital ascending node precesses through space in the opposing direction to that of the planet's orbital motion. This corresponds to a cyclically changing direction at which the orbital angular momentum vector points in space with respect to the invariable plane (the plane that lies orthogonal to the net angular momentum vector of the planetary system) at the frequency $\dot{\Omega}$ (the rate of the changing longitude of ascending node). This process resembles a coin spinning on a table top, in which the top face of the coin reorients itself in space as it rotates. Physically, forces from neighboring planets that are normal to a planet's orbit plane as it traverses along its orbit drive nodal precession, with a complete cycling occurring on a timescale of $\sim 70,000$ years for the Earth (Muller and MacDonald, 1995). Therefore this process only occurs when either the orbital plane of the planet shares a mutual inclination with that of a neighboring planet, or their orbital ascending nodes share some angular separation.

Looking to panel (b) of Figure 2.1, for the case of an eccentric orbit, the orientation of a planet's orbit can also evolve through a process called apsidal precession. This process involves the precession of the line of apsides, the imaginary line connecting the orbit's periapsis and apoapsis. During apsidal precession the orbital argument of periapsis, ω, the angle from the orbital ascending node to the position of periapsis, as well as the orbital longitude of periapsis, ϖ, the angle from the origin of the reference frame to the position of periapsis, both precess in the same direction as that of the planet's orbital motion. The motion of apsidal precession "hula hoops" the planet's orbit around its star at the frequency $\dot{\omega}$ (the rate of the changing argument
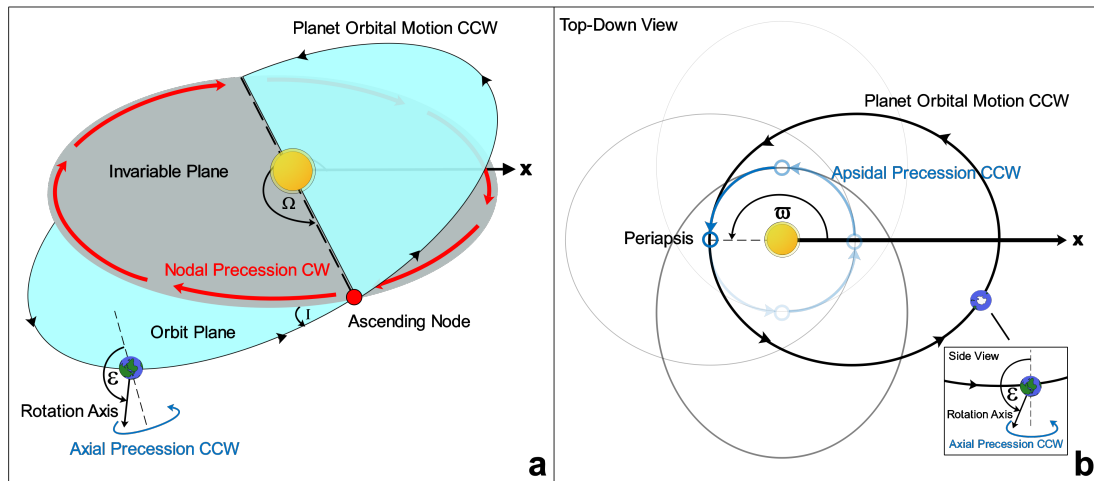
Figure 2.1 Panel (a) depicts the nodal precession of a retrograde-rotating planet's orbit that has some inclination, I, with respect to the invariable plane (the plane orthogonal to the net angular momentum vector of the planetary system). During this process, the longitude of the planet's ascending node, Ω, precesses in the clockwise direction while the planet's rotation axis precesses in the opposite (counter-clockwise) direction. Panel (b) depicts a visualization of the apsidal precession of the eccentric planet's orbit with a top-down view situated above the orbit plane. During this process the planet's longitude of periapsis, ϖ, precesses in the counter-clockwise (prograde) direction while the planet's rotation axis precesses in the same direction, as seen with the side view within the figure inset.

of periapsis). In contrast to nodal precession, forces from neighboring planets that are radial and tangential to the planet along its orbit drive apsidal precession. This precession cycle elapses over the course of $\sim 112,000$ years for the Earth (van den Heuvel, 1966). Unlike nodal precession, apsidal precession does not affect obliquity directly because the orientation of the orbital angular momentum vector does not change.

2.4.3 *A Spin-Orbit Resonance Enabled by Eccentricity*

Bearing in mind the processes in which the rotation axis and planetary orbit can evolve, special circumstances can induce large-amplitude obliquity variations. One such circumstance is the event of a 1:1 secular spin-orbit resonance between a planet's axial precession frequency, $\dot{\psi}$, and an orbital eigenfrequency of the planetary system

(usually a driver of nodal precession). While prograde rotators experience axial precession in the same direction as their nodal precession and can potentially achieve this spin-orbit resonance, retrograde rotators conventionally cannot. A positive orbital frequency that comes near a retrograde rotators axial precession frequency does not usually exist. Indeed, previous studies found retrograde rotators to be especially obliquity stable (Laskar and Robutel, 1993b; Lissauer *et al.*, 2012; Barnes *et al.*, 2016). I propose an exceptional circumstance. The orbital eccentricity of a retrograde-rotating planet can act to trigger a mechanism that enables a spin-orbit resonance which consequently drives obliquity variations.

For a planet with nonzero eccentricity, the process of apsidal precession indirectly affects that of nodal precession and introduces an additional orbital frequency. Figure 2.2 demonstrates this mechanism and shows four edge-on snapshots of a two-planet system, each with a different value of the inner planet's argument of periapsis. Here the inner planet has some mutual inclination with the outer body, and its orbit experiences apsidal precession as ω changes. Considering a more massive exterior planet which can be thought of as a uniform ring of mass in the long-timescale secular approximation, the orbit of the inner planet tips asymmetrically out of the ring mass plane twice over the duration of the precession cycle, that is, at a frequency of $2\dot{\omega}$. The inner planet therefore feels a difference in force pulling on it and its orbit experiences a precessional torque as it proceeds over the course of this cycle. This is important not only due to the contrast between the distance of the orbit's periapsis and apoapsis, but also because conservation of angular momentum requires that more time is spent at apoapsis compared to periapsis. This effect becomes more and more significant with larger values of eccentricity, and affects the process of nodal precession in the sense that the orbital angular momentum vector experiences an additional nutating motion.

Figure 2.3a visualizes this process, where an opposing nutating circular motion accompanies the traditional circular motion traced out by the orbital angular momentum vector during nodal precession. This motion can be thought of as two superimposed precessions, each with its own amplitude, frequency, and direction. Figure 2.3b summarizes this concept and shows that the primary nodal precession

frequency drives the orbital angular momentum vector at the frequency $\dot{\Omega}$ while the nutating motion operates at the frequency $2\dot{\omega}$. The resulting orbital frequency I expect to see for this nutation goes as

$$\nu = 2\dot{\omega} + \dot{\Omega} = 2\dot{\varpi} - \dot{\Omega} \tag{2.2}$$

where I used the relationship $\varpi = \Omega + \omega$ which translates to $\dot{\varpi} = \dot{\Omega} + \dot{\omega}$. Following this, the condition for the aforementioned spin-orbit resonance is when $\nu = \dot{\psi}$, or $2\dot{\varpi} - \dot{\Omega} - \dot{\psi} = 0$.
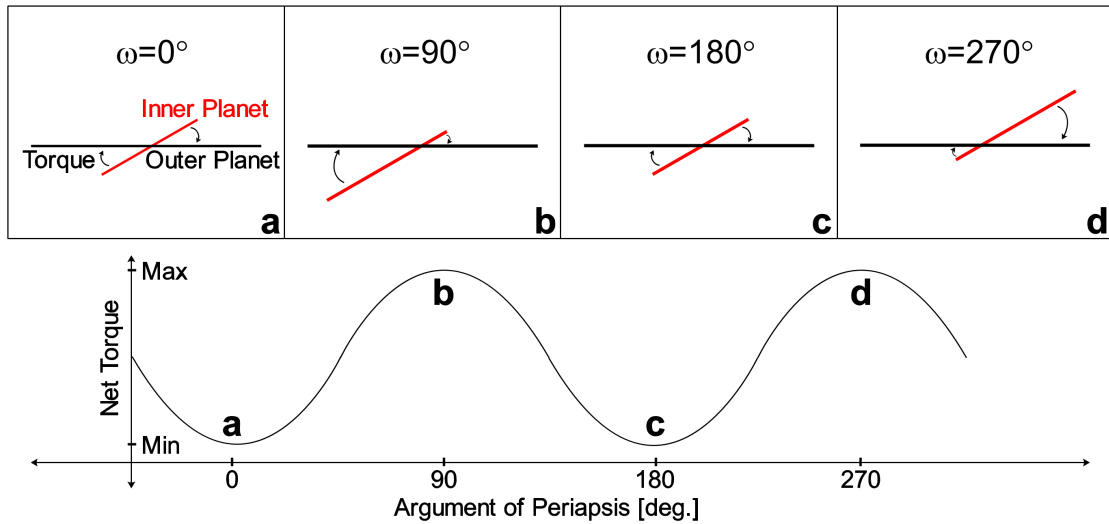
Figure 2.2 This edge-on perspective shows a massive outer planet's orbital plane (black) and an inclined, eccentric inner planet's orbital plane (red). The panels show four cases of the inner planet's argument of periapsis, ω, as it undergoes apsidal precession. Here I ignore the nodal precession of their orbits for simplicity and assume their longitudes of ascending node are equal (their orbital planes both remain edge on from my perspective). The cases for $\omega = 0°$ and $180°$ (when the line of apsides is co-planar with outer planet's orbital plane) occur twice, for which the normal force felt by the inner planet is zero at periapsis and apoapsis. The cases for $\omega = 90°$ and $270°$ show that the inner planet's orbital plane is tilted out of the outer planet's orbital plane, enabling a precessional torque due to the large difference in the normal force felt by the inner planet at the apsides. The letters on each of the panels map to the plot beneath, showing the net torque on the inner planet's orbit as a function of ω. The difference between the minimum and maximum net torque would grow for increasing eccentricity.
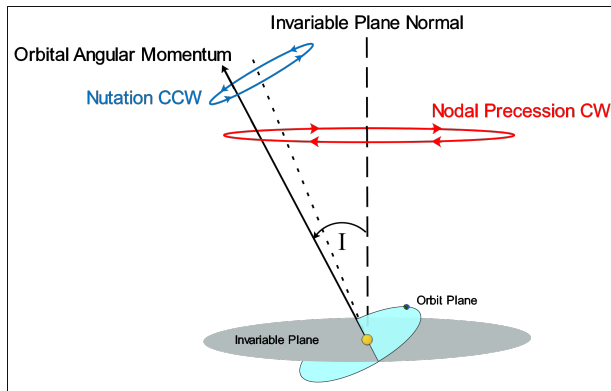
(A) The Physical Process
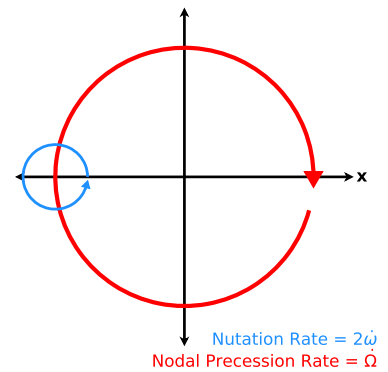
(B) Superimposed Precessions

Figure 2.3 Figure 2.3a shows a planet's orbital angular momentum vector as the straight black vector arrow. The planet's orbit has some inclination, I, with respect to the invariable plane (the plane that lies orthogonal to the net angular momentum of the planetary system). Due to the perturbations of a neighboring planet, its orbital angular momentum vector precesses around the invariable plane normal in the clockwise direction (viewed from above). In the case that the planet's orbit is eccentric, its orbital angular momentum vector nutates in the counter-clockwise direction. Figure 2.3b depicts the processes that I describe in Figure 2.3a acting as superimposed precessions with rates of $\dot{\Omega}$ and $2\dot{\omega}$, where $\dot{\Omega}$ and $\dot{\omega}$ are the rates at which the longitude of ascending node and argument or periapsis are changing, respectively.

2.5 NUMERICAL TREATMENT

2.5.1 *Approach*

I explore the validity of my analytical derivation by performing numerical simulations with the use of the mixed-variable symplectic N-body integrator, SMERCURY, which is a modified algorithm that adds spin-tracking capabilities to the original MERCURY package (Chambers, 1999). Similar to the works of Lissauer *et al*. (2012), Barnes *et al*. (2016), and Quarles *et al*. (2020), I use SMERCURY to track a planet's obliquity evolution while the planetary system dynamically evolves. I refer to Lissauer *et al*. (2012) for a thorough description of my technique, although I highlight some key details here.

SMERCURY computes the orbital evolution of the system's bodies based on orbital forcing interactions between one another, in which I base the calculations on a time step of at most 5% of the orbital period of the inner-most planet. In the meantime, the SMERCURY algorithm only tracks the obliquity evolution of one body in a specified system, although it features what I call "ghost planets". Ghost planets are essentially massless clones of the tracked body with their own assigned rotation states, in which their obliquities evolve independently. This scheme allows for a broad exploration of parameter space and saves computation time.

A SMERCURY simulation treats the tracked planet along with its ghost planets as axisymmetric rigid bodies, in which their rotation states evolve due to gravitational torques exerted on their rotational bulges. I assign a value for the planet's oblateness coefficient J_2 based on the their rotation periods, computed by following the Darwin-Radau relation (Hubbard, 1984; Murray and Dermott, 1999). This value remains fixed throughout the duration of the simulation, which implies that I do not account for tidal dissipation effects. I can neglect these effects so long as the timescale for tidal effects to become important for the planet greatly exceeds the chosen integration time. Considering a moonless Earth with a rotation period of 24 hours as an example, it would take of order 10^{10} years for the Earth to become tidally locked with the Sun. In this case, the amount of tidal deceleration over the course of a 100 Myr simulation would have little effect on its spin evolution.

I initialize each simulation by generating the rotation states of each planet based on their desired orientation and rotation period, taking into account the orientation of the orbit plane. Recalling from Section 2.4, together the obliquity and the precession angle specify the orientation of a planet's rotational angular momentum vector. I transform these angles by accounting for the orbital inclination and longitude of ascending node, following the explanation of Neron de Surgy and Laskar (1997b) and Barnes *et al.* (2016).

2.5.2 *Initial Conditions*

I design a simple numerical experiment to test the eccentricity mechanism that I predict destabilizes the obliquities of retrograde rotating planets. I consider a toy system consisting of the Sun as the primary body, a moonless Earth I call Earthmoo (the exclusion of the Moon simplifies my experiment), and Jupiter. Earthmoo is taken to have the same density as the real Earth yet has the mass of the combined Earth-Moon system, which is consistent with the approach of Lissauer *et al.* (2012) and Barnes *et al.* (2016). I arbitrarily initialize my simulations according to Table 2.1, for which the orbital elements are with respect to the J2000 epoch and ecliptic (Murray and Dermott, 1999). Earthmoo's orbital elements mostly mimic that of the real Earth-Moon barycenter at this epoch, although I assign values of 0, 0.1, 0.3, and 0.5 for its initial orbital eccentricity across separate simulations. I begin Jupiter on a circular orbit (its initial eccentricity is set to zero) at the start of all of my simulations in order to avoid unwanted excitation of Earthmoo's eccentricity. Importantly, I place a mutual inclination between Earthmoo and Jupiter in order to ensure that the orbit of Earthmoo will experience nodal precession as Jupiter exerts gravitational tugs normal to Earthmoo's motion. I set the initial orbital inclinations of Earthmoo and Jupiter to the arbitrary values of $2.30530°$ and $1.30530°$, respectively; note that their mutual inclination actually works out to be $3.04204°$ from the spherical law of cosines, due to the angular difference between their orbital ascending nodes. Deitrick *et al.* (2018a) similarly tested a mutually inclined Earth-Jovian system with large eccentricities, but did not test Earths with retrograde obliquities.

System Orbital Parameters

Planet	m [$M_\odot$]	a [AU]	e	I [deg]	ω [deg]	Ω [deg]	M [deg]
Earthmoo	3.04 x 10^{-6}	1.00000011	-	2.30530	114.20783	348.73936	357.51716
Jupiter	9.5450 x 10^{-4}	5.20336301	0	1.30530	274.19770	100.55615	19.65053

Table 2.1 Initial values for the planetary mass (m), semi-major axis (a), eccentricity (e), inclination (I), argument of periapsis (ω), longitude of ascending node (Ω), and mean anomaly (M) for the Earthmoo-Jupiter system taken from Murray and Dermott (1999). These values correspond to the J2000 ecliptic with respect to the Earth-Moon barycentre. The mass of Sun taken to be 1.98911×10^{30} kg, while I set Earthmoo's initial eccentricity to 0, 0.1, 0.3, and 0.5.

P_{rot} [hrs]	R_{eq} [km]	J_2	α ["/yr]
4	6721.04	0.0441685	118.86406
6	6520.71	0.0179269	72.36607
10	6438.62	0.0062130	41.80041
16	6412.76	0.0023978	25.81175
24	6403.80	0.0010612	17.13579
34	6400.24	0.0005279	12.07568
46	6398.64	0.0002882	8.91882

Table 2.2 Computed initial values for the rotation period (P_{rot}), equatorial radius (R_{eq}), oblateness coefficient value (J_2), and precession constant (α) for Earthmoo determined from Lissauer *et al.* (2012).

I explore a range of rotation states composed of varied rotation periods and initial obliquities that correspond to varied axial precession frequencies following Equation 1.1. This variation allows for a contrast of Earthmoos caught both in and out of my proposed spin-orbit resonance. Therefore, I test a range of Earthmoo rotation periods spanning 4 to 46 hours, where I select the 4 hour lower limit due to the physical limitation that Earthmoo would be near breakup and no longer axisymmetric, sticking to my Darwin-Radau assumptions discussed in the previous section. Taking Earthmoo to have a density of 5.5153 g/cm^3 and a constant moment of inertia coefficient of 0.3296108, I compute the J_2 values for each case. I show a summary of the rotational parameters I use in Table 2.2. Since this work investigates retrograde rotating planets, I test initial obliquities of Earthmoo ranging from 90° to 180°, in 5° increments. Each obliquity value that I test pairs with a precession angle (ψ) value; I arbitrarily set the initial ψ value of the Earthmoos to 348.74°.

2.6 RESULTS AND DISCUSSION

2.6.1 *Frequency Analysis*

The mechanism that I describe in Section 2.4 suggests that my Earthmoo-Jupiter system will involve a significant positive orbital frequency pertaining to the nodal precession of an eccentric Earthmoo's orbit. I predict that this frequency will take on a value according to Equation 2.2. In order to test this mechanism, I perform a set of simulations and conduct a Fourier analysis to obtain the secular eigenfrequencies of the system.

I ran 100 Myr simulations sampled at 100 year intervals of the Earthmoo-Jupiter system described by Table 2.1; here I set the integration time step to 2.5% of Earthmoo's orbital period. From this, I performed a Fourier analysis over the course of the simulation of the inclination vector ($[I \cos \Omega, I \sin \Omega]$) and the eccentricity vector ($[e \cos \varpi, e \sin \varpi]$). This is done using a Frequency-modified Fourier Transform (Šidlichovský and Nesvorný, 1996), yielding the amplitude, frequency, and phase for each mode. The two most prominent amplitude frequencies (the subsequent frequencies have orders of magnitude less power and are thus left out) are displayed for each in Table 2.3. I exclude a prominent peak of inclination vector found in each analysis at 0 $''$/yr, as it is an artifact due to a degeneracy in the inclination vector (Murray and Dermott, 1999).

Looking to Figure 2.4, for each case of eccentricity, I show the orbital frequencies of the inclination vector; I overlay Earthmoo's range of axial precession frequencies according to Equation 1.1 to allow for a visual comparison. I expect pronounced obliquity variation to occur near regions of parameter space in which these frequencies have values near one another. Inspecting the values within Table 2.3, a significant positive frequency peak appears for the eccentric cases, yet is absent for the zero eccentricity case. This peak grows in amplitude for increasing values of eccentricity. Also observe that both the dominant negative peak and the positive peak shift to higher frequencies with larger values of eccentricity due to Earthmoo's orbit becoming easier to torque, which causes its ascending node to precesses faster.

Secular Orbital Frequencies

e_0	j	Inclination Vector Series			Eccentricity Vector Series		
		ν_j [$''$/yr]	S_j	$\phi_j^{(0)}$ [deg]	μ_j [$''$/yr]	E_j	$\theta_j^{(0)}$ [deg]
0	1	-7.06	3.038000	325.28	7.03	0.000027	90.91
	2	-14.13	0.000610	100.43	0.01	0.000003	247.14
0.1	1	-7.22	3.036219	325.7	7.00	0.100044	103.08
	2	21.22	0.020543	240.49	-21.45	0.000188	8.25
0.3	1	-8.49	3.036676	328.68	6.75	0.300010	103.07
	2	21.98	0.180591	237.46	-23.72	0.000501	14.30
0.5	1	-10.95	3.110164	334.51	6.18	0.499828	103.05
	2	23.32	0.498464	231.59	-28.08	0.000698	25.97

Table 2.3 The results from my Frequency-modified Fourier Transform analysis of the inclination vector ([$I \cos \Omega$, $I \sin \Omega$]) and the eccentricity vector ([$e \cos \varpi$, $e \sin \varpi$]) of Earthmoo for different initial values of eccentricity (e_0), where I is the orbital inclination, Ω is the longitude of ascending node, e is the eccentricity, and ϖ is the longitude of periapsis. I show the top two values of the frequency (ν_j), amplitude (S_j), and phase (ϕ_j) of the inclination vector, as well as the top two values of the frequency (μ_j), amplitude (E_j), and phase (θ_j) of the eccentricity vector.

Frequency Comparison

e_0	$\nu_{predict}$ ["/yr]	ν_{actual} ["/yr]
0	-	-
0.1	21.22	21.22
0.3	21.99	21.98
0.5	23.32	23.32

Table 2.4 The predicted value of the eccentricity-enabled frequency ($\nu_{predict}$) for each case of initial eccentricity (e_0) according to Equation 2.2 using the frequency values from Table 2.3. For comparison, I list the actual frequency value (ν_{actual}) from the Fourier analysis, which is also listed as ν_2 in Table 2.3. This prediction does not apply to the 0 initial eccentricity case.
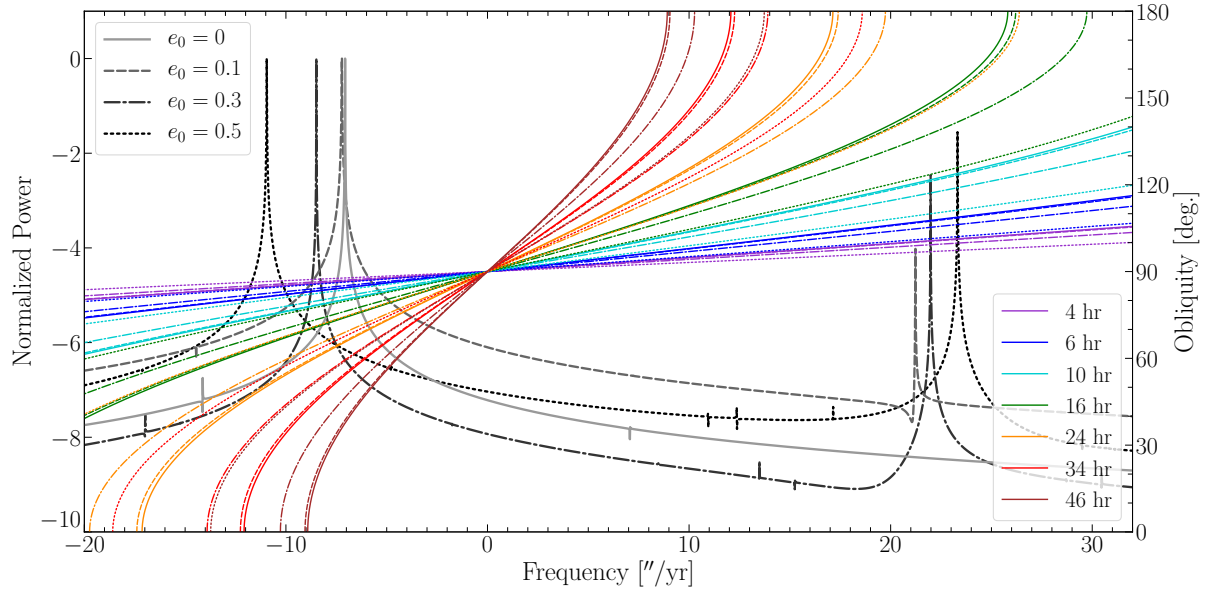
Figure 2.4 The power spectra of the orbital frequencies of Earthmoo's inclination vector for each case of initial eccentricity (e_0) obtained from my Frequency-modified Fourier Transform analysis. I show these spectra as the varied black lines paired with the left and bottom axes, which are normalized on a log scale. I overlay Earthmoo's range of axial precession frequencies for varied rotation periods and obliquities, computed according to Equation 1.1; I show these frequencies as colored lines that pair with the right and bottom axes, for each case of eccentricity (I vary the line styles the same way as the the orbital frequencies). The obliquity can be excited when Earthmoo's axial precession frequency becomes commensurate with an orbital frequency in a spin-orbit resonance. The positive orbital frequency peak present for the eccentric cases has the potential to enter a spin-orbit resonance with retrograde-rotating Earthmoos.

I describe in Section 2.4 that this positive frequency should follow a predictable relationship stated in Equation 2.2. Noting that the dominant frequency for the inclination vector for each of the eccentricity cases in Table 2.3, ν_1, corresponds to $\dot{\Omega}$, the driver of nodal precession. Similarly the dominant frequency found in the analysis of the eccentricity vector in Table 2.3, μ_1, corresponds to $\dot{\varpi}$, the driver of apsidal precession. Taking the 0.3 eccentricity Earthmoo case as an example, I find that $\dot{\Omega} = \nu_1 = -8.49$ ''/yr and $\dot{\varpi} = \mu_1 = 6.75$ ''/yr. According to Equation 2.2, this yields $\nu = 2\dot{\varpi} - \Omega = 21.99$ ''/yr, which nearly matches my reported value from the Fourier analysis for ν_2 of 21.98 ''/yr. I compare the frequency values for the other

eccentricity cases in Table 2.4. These cases provide good support for my proposed mechanism and show that the frequency relationship described in Equation 2.2 holds.

In addition, using the same results but only the first 500,000 years of my simulations, I generate plots of the inclination vector components as seen in Figure 2.5. In essence, these plots demonstrate the projection of a planet's orbital angular momentum vector as it reorients in space due to variations in the orbital inclination and the process of nodal precession. I examine these plots for each Earthmoo-Jupiter test case in order to gain additional understanding into the physical process that takes place. While the 0 and 0.1 eccentricity cases show the orbital angular momentum vector trace a neat, mostly circular path, the 0.3 and 0.5 eccentricity cases reveal more complex behavior. These higher eccentricity cases show that the position of the orbital angular momentum vector strays from circular, and swings outward periodically to produce the outer "petals" seen with the overlap of previous tracings. This observation exemplifies the physical process described in Figures 2.3a and 2.3b, in which the additional positive frequency introduced acts to nutate the orbital angular momentum vector in the opposing direction as it undergoes nodal precession.

2.6.2   *N-body Simulations*

The previous section showed and discussed the nature of the secular orbital eigenfrequencies in my toy Earthmoo-Jupiter system. The mechanism that I describe in Section 2.4 successfully predicts a significant positive secular frequency that could participate in a spin-orbit resonance for a retrograde-rotating Earth. However, I must also determine whether this resonance is significant enough to drive large-amplitude obliquity variations important for the consideration of life.

I demonstrate this phenomenon by simulating the aforementioned Earthmoo-Jupiter system over the course of 100 Myr, sampling at 10,000 year intervals with an integration time step of 5% of Earthmoo's orbital period. Note that orbital changes of Earthmoo's inclination and ascending node throughout the simulations result in changes in its obliquity, so I expect a baseline obliquity variation of up to $\Delta \epsilon = \epsilon_{max} - \epsilon_{min} \approx 2I_m \sim 6°$ (Quarles *et al.*, 2019), where I_m is the mutual inclination
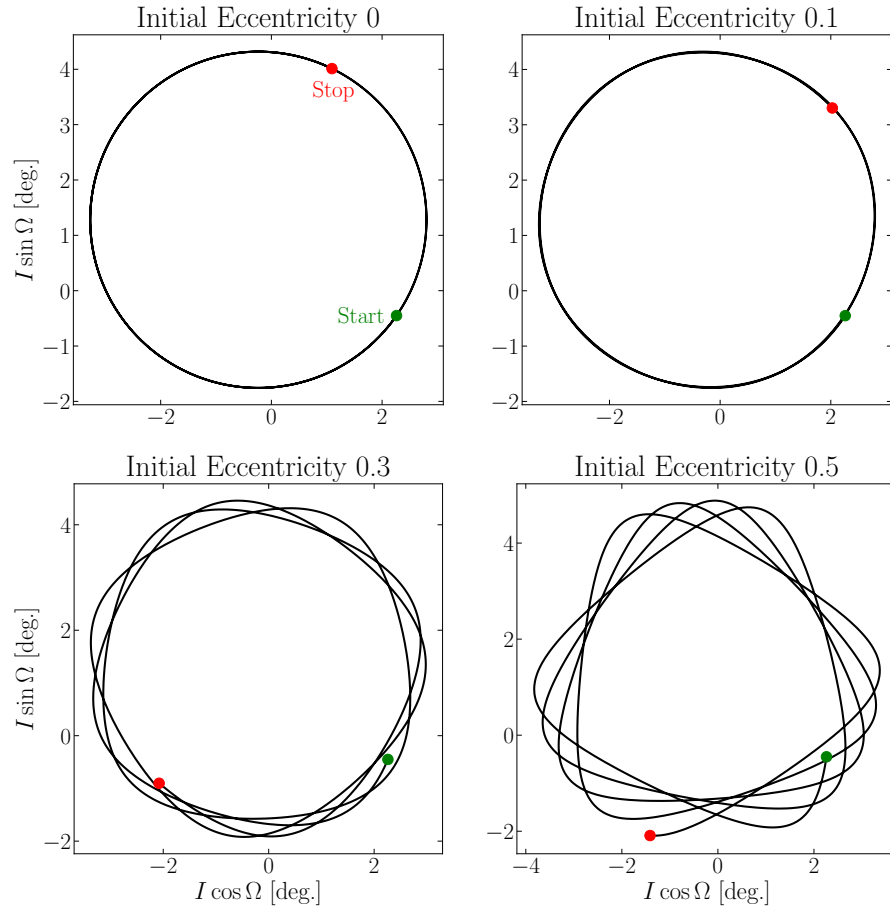
Figure 2.5 For each case of initial eccentricity I plot the inclination vector components as $[I \sin \Omega]$ versus $[I \cos \Omega]$ over the course of 500,000 years, sampled every 100 years. This depiction serves as a projection of the direction of Earthmoo's orbital angular momentum vector over time; the green and red dots mark the start and end of the simulation, respectively. The 0 and 0.1 eccentricity cases show Earthmoo's orbital angular momentum vector tracing out a nearly circular path as its inclination varies and its ascending node precesses. However, the 0.3 and 0.5 eccentricity cases show a path that deviates from circular, in which the orbital angular momentum vector swings outward periodically. This motion is due to the eccentricity mechanism described in Section 2.4, in which the orbital angular momentum vector undergoes a nutation in the opposing direction.

between the orbits of Earthmoo and Jupiter as stated in Section 2.5.2. I am interested in pronounced obliquity variations that arise from the proposed spin-orbit resonance, which I expect to be nestled among this baseline variation. I describe the results in the following section, with frequent reference to Table 2.3 and Figure 2.4 in order to discuss their relations.

Beginning with the zero initial eccentricity case, Figure 2.6 displays the range of obliquity variation explored by each Earthmoo for the tested parameter space over the course of the 100 Myr simulation. For the rotation periods and initial obliquities tested, the majority of Earthmoos experience little variation in their obliquity across the board, mostly varying $\sim 1°$-$3°$, similar to that of the present day Earth. Here I find that 100% of the Earthmoos vary less than the expected $2I_m$ baseline value. However, an exception here is a pronounced increase in obliquity variation for the Earthmoos with initial obliquities set near $90°$. These cases experience obliquity variations of $\sim 3°$-$6°$. Although these are still relatively small values, looking back to Figure 2.4, the proximity of the axial precession frequencies of these $90°$ obliquity Earthmoos to the dominant negative orbital frequency explains the pronounced variation. Looking to Table 2.3, the frequency ν_1 is the primary driver of nodal precession, clocking at -7.07 $''$/yr. Recall that for the zero eccentricity case, there is no significant positive orbital frequency present, hence the general lack of interesting variation across the parameter space.

Moving on to the 0.1 initial eccentricity case, as a similar plot, Figure 2.7 displays the range of obliquity variation for this set of Earthmoos. Again the majority of test cases exhibit obliquity variations $\sim 1°$-$3°$ (99.2% vary less than $2I_m$), with the Earthmoos having nearly $90°$ obliquities showing variations of $\sim 4°$-$6°$. Interestingly, there are a few additional test Earthmoos that stick out with pronounced obliquity variations. These include the $100°$ obliquity Earthmoo in the 4 hour case varying $\sim 3°$, the $120°$ obliquity Earthmoo in the 10 hour case varying $\sim 4°$, and the $145°$ obliquity Earthmoo in the 16 hour case varying $\sim 6°$. Figure 2.4 maps these regions of parameter space, where the Earthmoos of these combinations of rotation period and obliquity have frequencies near to the now excited positive orbital frequency peak which Table 2.3 marks as 21.23 $''$/yr.

The 0.3 initial eccentricity case follows this trend, looking to Figure 2.8. Most of these Earthmoo cases see obliquity variations of $\sim 1°$-$4°$ (94.7% vary less than the $2I_m$), while the $90°$ obliquity Earthmoos swing $\sim 5°$-$6°$ with rotation periods 6-46 hours. The 4 hour $90°$ obliquity Earthmoo in particular experienced a much larger $\sim 15°$ range of variation. The 4 hour case also has an additional "hot spot"
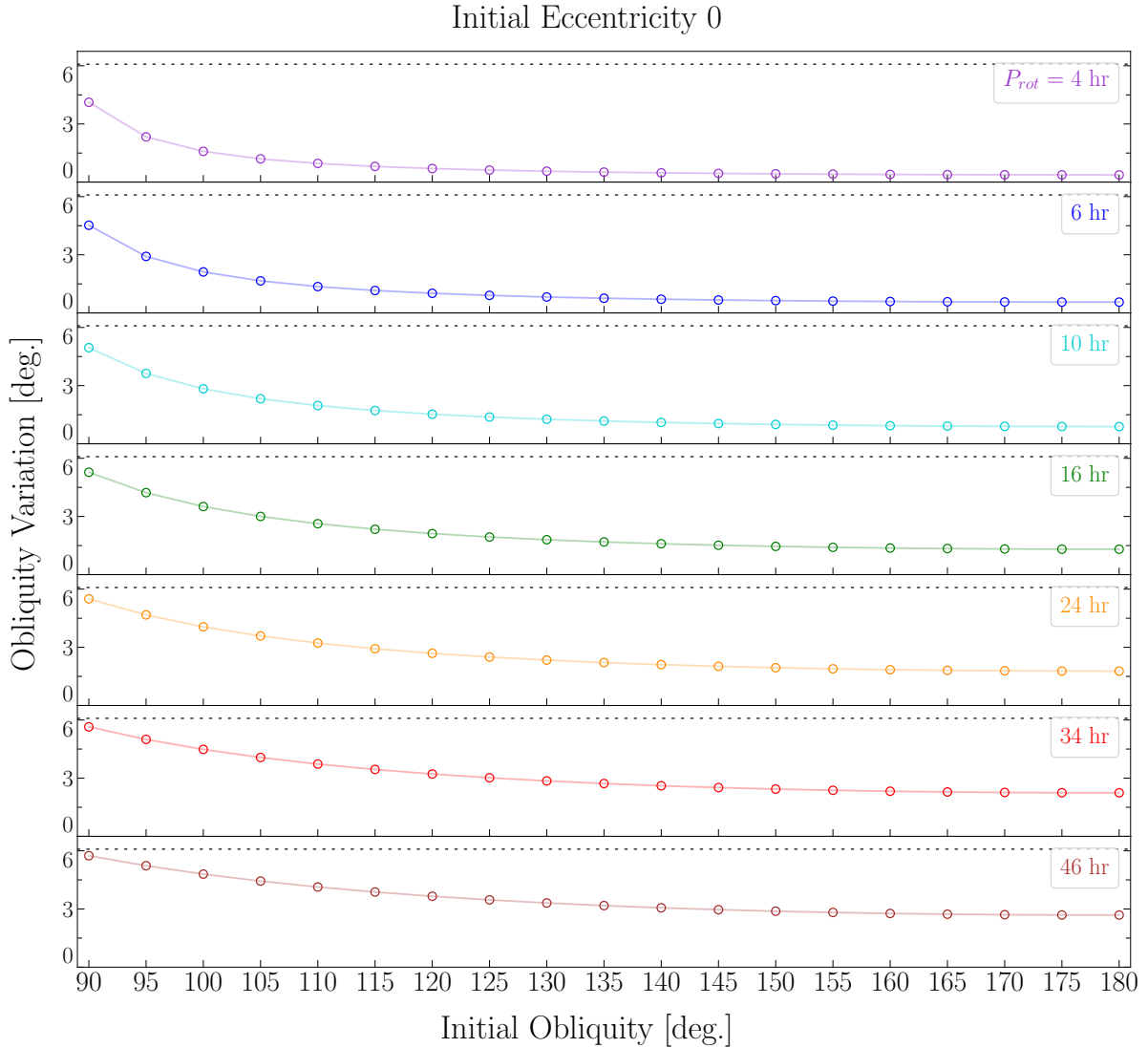
Figure 2.6 For the Earthmoo case with an initial eccentricity of zero, I show the range of obliquity variation ($\Delta\epsilon$) explored by each Earthmoo ghost planet over the course of the 100 Myr simulation as the colored markers with the vertical axis. The black dashed lines mark the threshold of the expected baseline obliquity variation due solely to orbital changes (twice the mutual inclination of Earthmoo and Jupiter). The horizontal axis corresponds to the initial obliquity at the start of the simulation, while each subplot groups corresponds to the different rotation periods (P_{rot}) of 4, 6, 10, 16, 24, 34, and 46 hours that I test. The color scheme is consistent with that of Figure 2.4.

for the Earthmoo with an initial set obliquity of 100°, varying by $\sim 6°$. The 6 hour case has an Earthmoo with a pronounced $\sim 7°$ variation with an initial 105° obliquity. Additionally, the 10 hour case has Earthmoos that experience $\sim 10°$ and 5° variations for the initial obliquities 115° and 120°, respectively. The 16 hour case sees
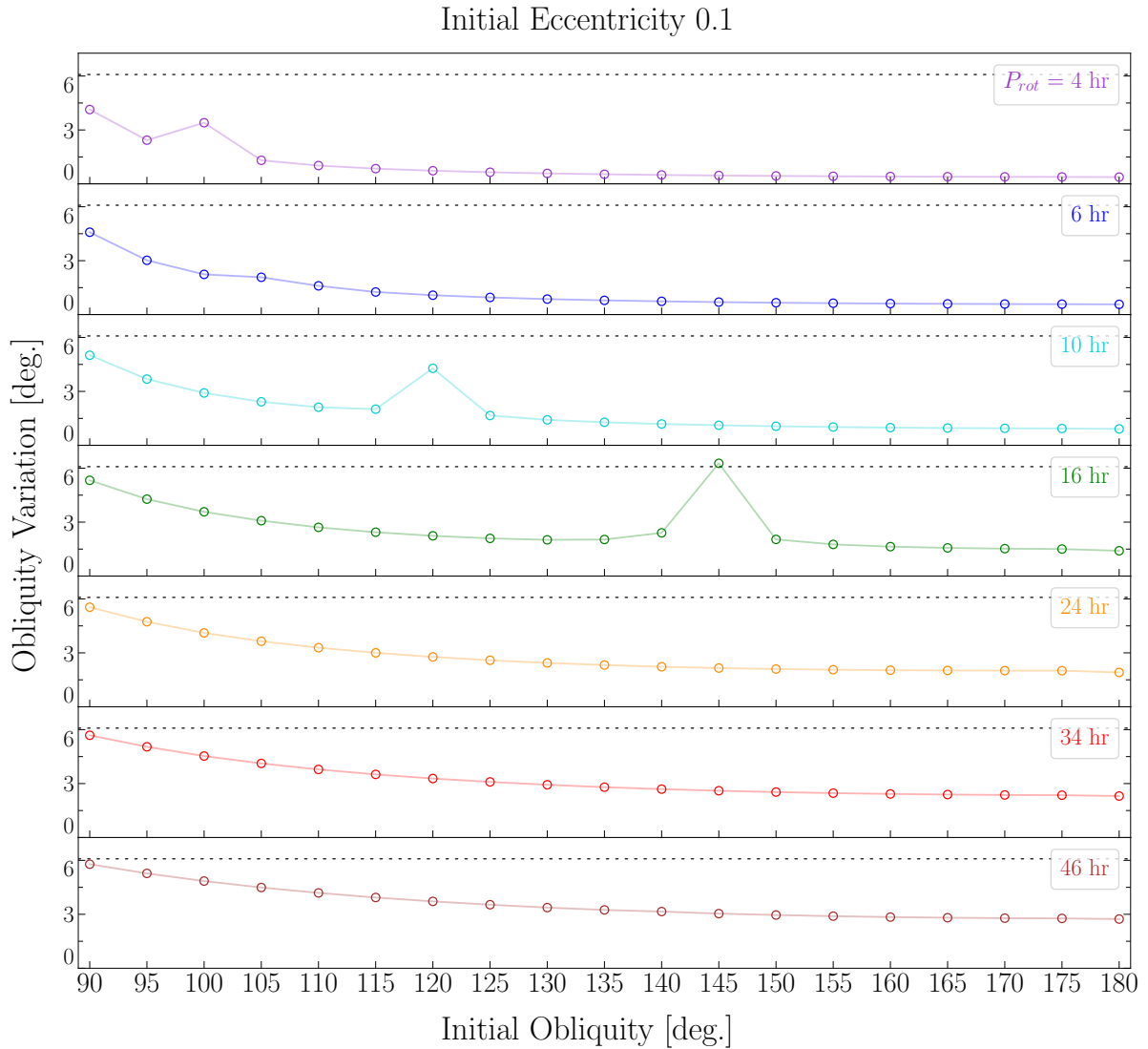
Figure 2.7 Similar to Figure 2.6, but for the Earthmoo case with an initial eccentricity of 0.1.

pronounced variation centered around the 135° and 140° obliquity cases each with $\sim 14°$ variation. The 24 hour case is not as dramatic, but sees slightly pronounced variation for its higher obliquity cases $> 155°$ by a few degrees. According to Table 2.3, the positive orbital frequency peak has increased in amplitude and has been shifted to a frequency of 21.98 ''/yr. The shift of the peak appears to correlate roughly with the regions of pronounced obliquity variation as mapped by Figure 2.4.

Finally, Figure 2.9 displays the results of the 0.5 initial eccentricity case. Most of test Earthmoo cases with rotation periods 4-16 hours only experience obliquity
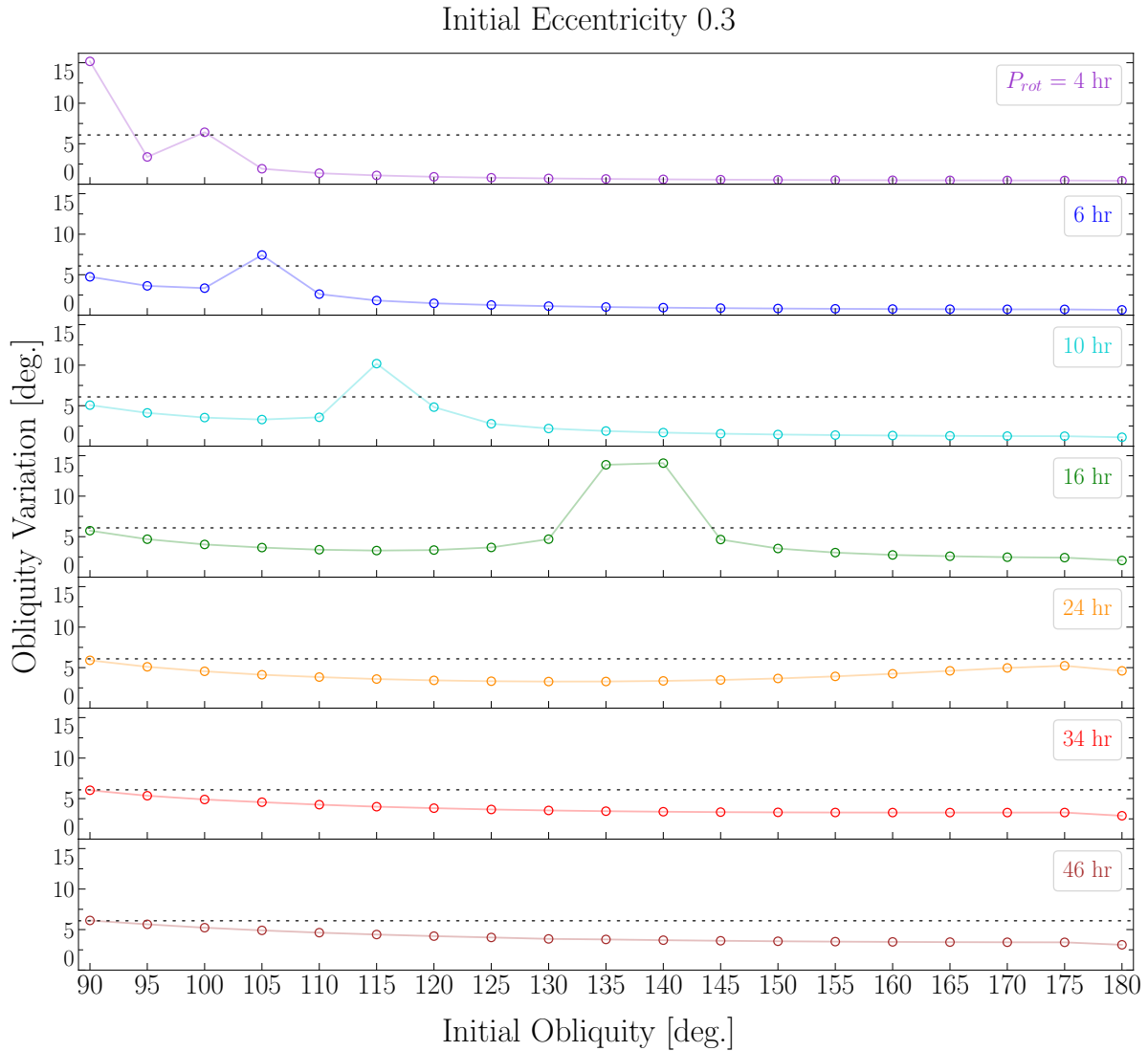
Figure 2.8 Similar to Figure 2.6, but for the Earthmoo case with an initial eccentricity of 0.3.

variations of $\sim 1°$-$4°$. The majority of Earthmoos with rotation periods 24-46 hours see consistent yet higher variations of $\sim 5°$-$6°$. Here I find that 75.9% of the Earthmoos experience obliquity variations less than the expected $2I_m$ baseline value. This time, the Earthmoos with initial obliquities of 90° don't stick out quite as much, although the 4 hour and 6 hour case Earthmoos do experience variations of $\sim 24°$ and $21°$, respectively. The driver of the large obliquity variation for the 90° obliquity Earthmoos has appeared to be the fault of the negative orbital frequency peak at -10.95 ″/yr according to Table 2.3. This peak appears to have now shifted enough

so that the Earthmoos with rotation periods > 6 hours evade a resonance with it. Notable test cases with pronounced variation include the four hour 95° obliquity Earthmoo that varies $\sim 19°$, the 6 hour 100° obliquity Earthmoo that varies $\sim 11°$, the 10 hour 110° obliquity Earthmoo that varies $\sim 14°$, the 16 hour 125° and 130° obliquity Earthmoos that vary about 18° and 20°, respectively, and the 24 hour batch of Earthmoos with initial obliquities ranging from 145° to 160° that vary from 16° to 31°. The positive frequency orbital peak has again increased in amplitude due to the greater value of eccentricity, and is roughly 23.32 ″/yr according to Table 2.3. Figure 2.4 once more largely maps out the pattern of variation.

2.6.3 *Semi-Analytical Secular Model*

Although I am confident in my methodology and the accuracy of my results, running simulations with SMERCURY is computationally expensive and limits the parameter space that I can explore. I choose to complement my results by examining a broader parameter space and employ the less robust but useful semi-analytical secular spin evolution approach as featured in Quarles *et al.* (2019). This approach applies a secular time-dependent Hamiltonian to the orbital integration results computed by SMERCURY in order to compute the spin evolution of a planet. I use the same initial conditions as my other simulations (according to Table 2.1), and apply this model to the 100 Myr, sampled every 100 years, orbital evolution results as featured in Figures 2.4 and 2.5. However, I now explore initial obliquities for Earthmoo from 90° to 180° in 1° increments while I sweep the values of the precession constant (relates to rotation period) from 0 ″/yr to 120 ″/yr in 1 ″/yr increments. Here the initial precession angle is 348°.

Looking to Figure 2.10, I display the range of obliquity variation ($\Delta\epsilon$) each Earthmoo experienced for each case of initial eccentricity. Since I was able to explore a much finer grid of parameter space using this approach, I present my results in different way that more easily highlights the trends. These results are in good agreement with those discussed in Section 2.6.2. The majority of Earthmoos are quite stable and only vary 1°-2°, while the cases in which Earthmoo had an initial obliquity near 90° similarly resulted in heightened obliquity variation. The test Earthmoos
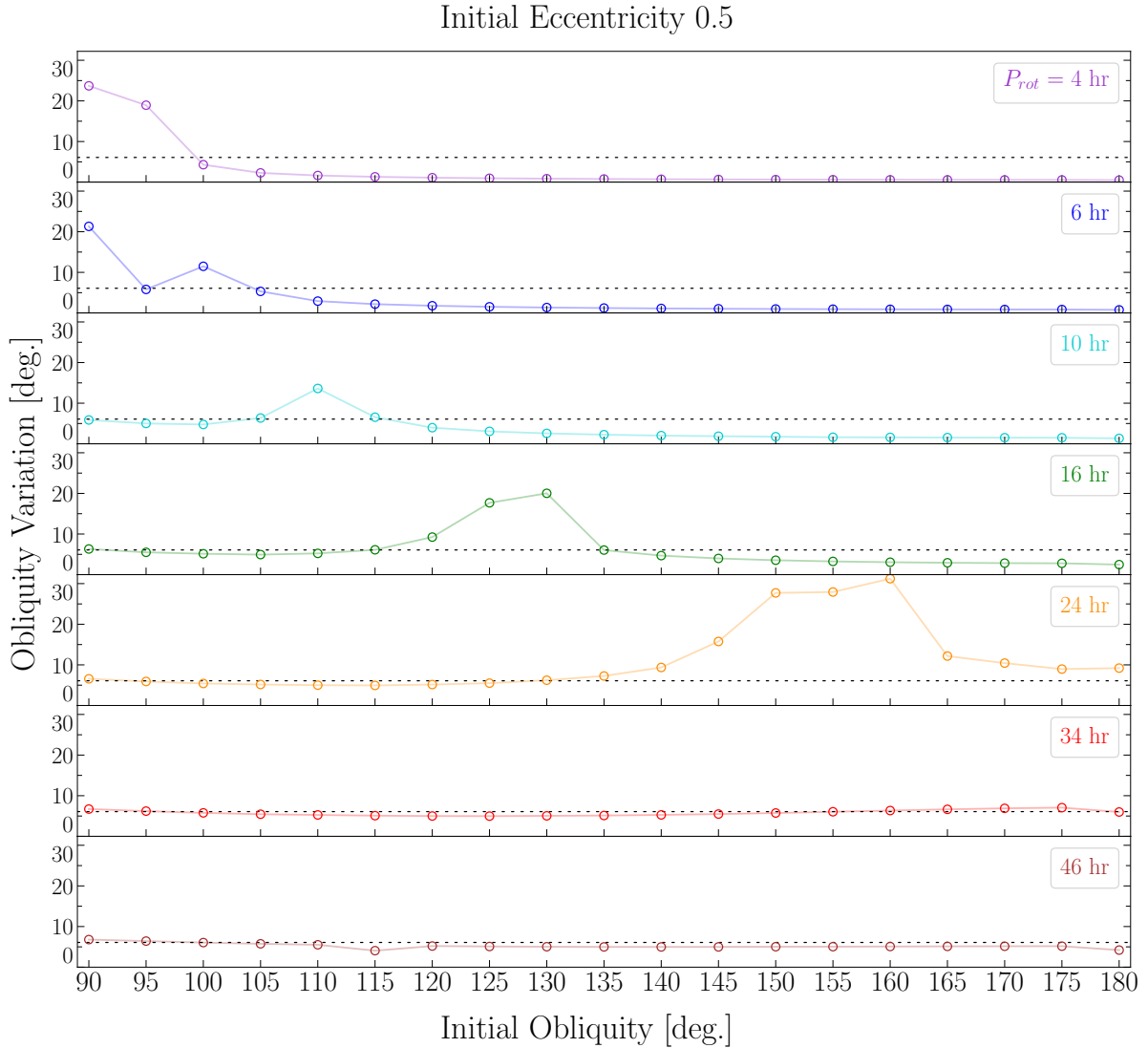
Figure 2.9 Similar to Figure 2.6, but for the Earthmoo case with an initial eccentricity of 0.5.

experienced pronounced obliquity variation near the predicted locations of the spin-orbit resonance. In addition, there is a splitting trend that distinguishes two regimes of variation that follow the predicted resonance location which become more evident for higher values of eccentricity. Figure 12 of Quarles *et al.* (2020) showcases a similar splitting trend, in which the authors explain that it is a consequence as a result of the difference between the initial precession angle and the initial longitude of ascending node ($\psi_0 - \Omega_0$) having a large angular separation from the phase of the resonant orbital frequency (shown as γ_i in Table 2.3). I again find that the magnitude of these

variations generally increase with eccentricity (due to increasing amplitudes of the orbital frequencies), where I report a maximum variation of 35.24° for the Earthmoo with an initial eccentricity of 0.5 with an initial obliquity of 174° and a precession constant of 16 ″/yr.

2.6.4 *A Closer Look at the Resonance*

Taking the results of my N-body simulations, I can gain additional insight into the nature of this eccentricity-enabled spin-orbit resonance through further analysis. In Section 2.4 I discussed that the condition for this resonance was that $2\dot{\varpi} - \dot{\Omega} - \dot{\psi} = 0$. The corresponding resonant angle, λ, is therefore

$$\lambda = 2\varpi - \Omega - \psi \tag{2.3}$$

Saillenfest *et al.* (2019) provides an analytical theory that identifies this angle as a first-order term that obeys the "Colombo's Top" Hamiltonian. Here, I use my numerical simulations to verify that λ is indeed a valid resonant angle, and that it is connected to the observed obliquity variations. I select the Earthmoo with a 16-hour rotation period and an initial obliquity of 140° from the 0.3 initial eccentricity case (featured in Figure 2.8) to serve as an example. I plot the Earthmoo's resonant angle and obliquity as functions of time for the first 5 Myr of the simulation in Figure 2.11. This plot is revealing, and shows that λ is indeed librating about zero, as one would expect for a valid resonant angle. Furthermore, the variations in λ lead the variations in obliquity by 90°, implying a direct dynamical connection between these two angles.

The behavior shown in Figure 2.11 also highlights the importance of initial conditions. Previous work found that the choice of the initial precession angle can influence the obliquity evolution in the sense that it affects the phasing of frequencies involved in the spin-orbit resonance, which in turn moderates the strength of the resonant interactions (Lissauer *et al.*, 2012; Barnes *et al.*, 2016; Quarles *et al.*, 2020). The example Earthmoo in Figure 2.11 had an initial precession angle of 348.74°, in which the wide libration of its resonant angle and subsequent large obliquity variations was likely determined by its initial combination of ϖ, Ω, and ψ. Therefore I conclude that
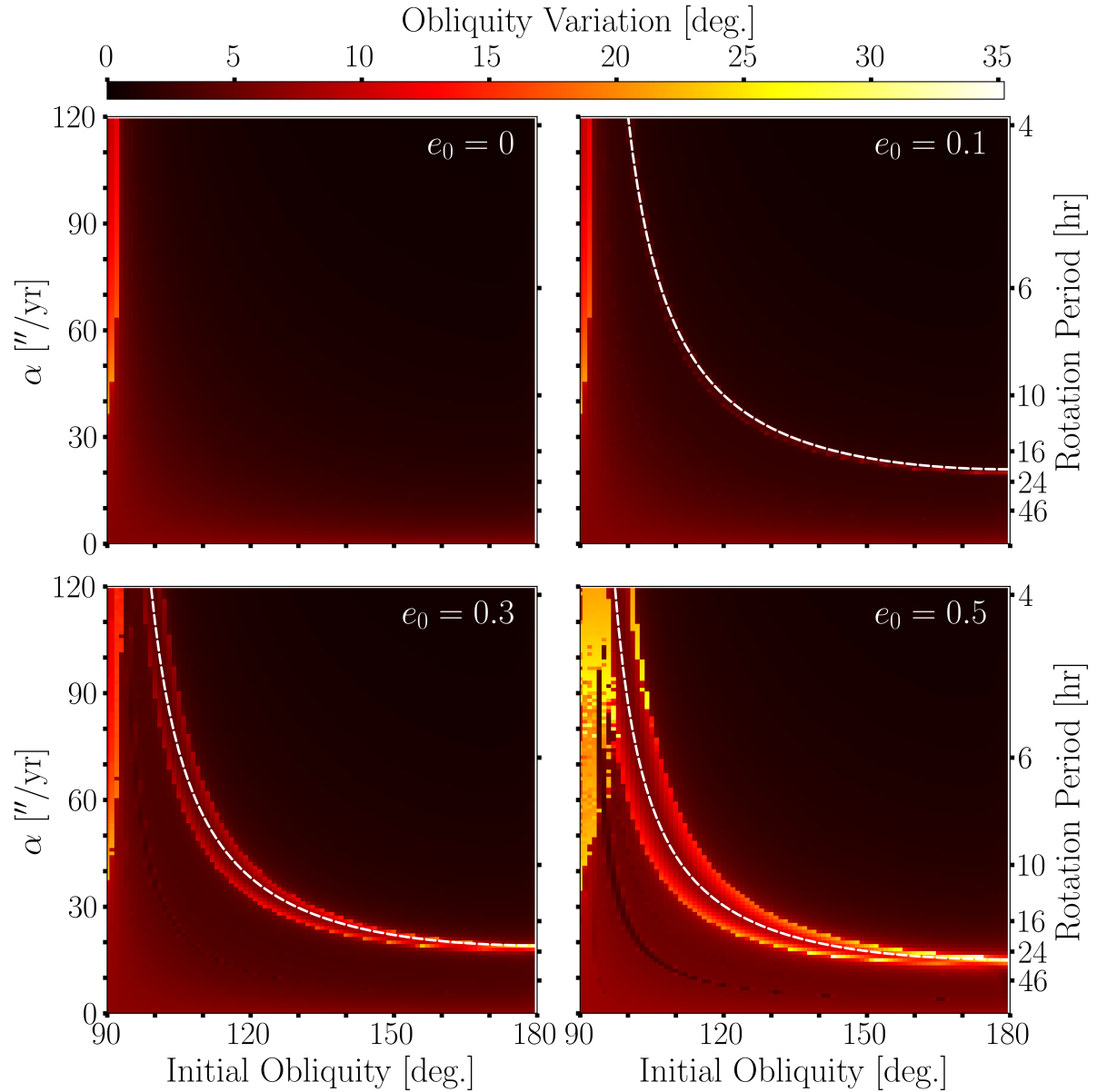
Figure 2.10 For each case of initial eccentricity (e_0), I show the obliquity variation ($\Delta\epsilon$) each Earthmoo experienced over the course of the 100 Myr simulation for a range of values of the initial obliquity and precession constant, α (related to the rotation period). The values of obliquity variation are mapped to the color bar shown at the top of the plot, ranging from zero to the maximum recorded value of 35.24° (from the $e_0 = 0.5$ case) according to the semi-analytical approach described in Section 2.6.3. The dashed white lines for the 0.1, 0.3, and 0.5 eccentricity cases mark the predicted locations of the spin-orbit resonance.

these angles play a role in controlling the range of affected obliquity configurations near the resonance. Future work could explore this phenomenon.
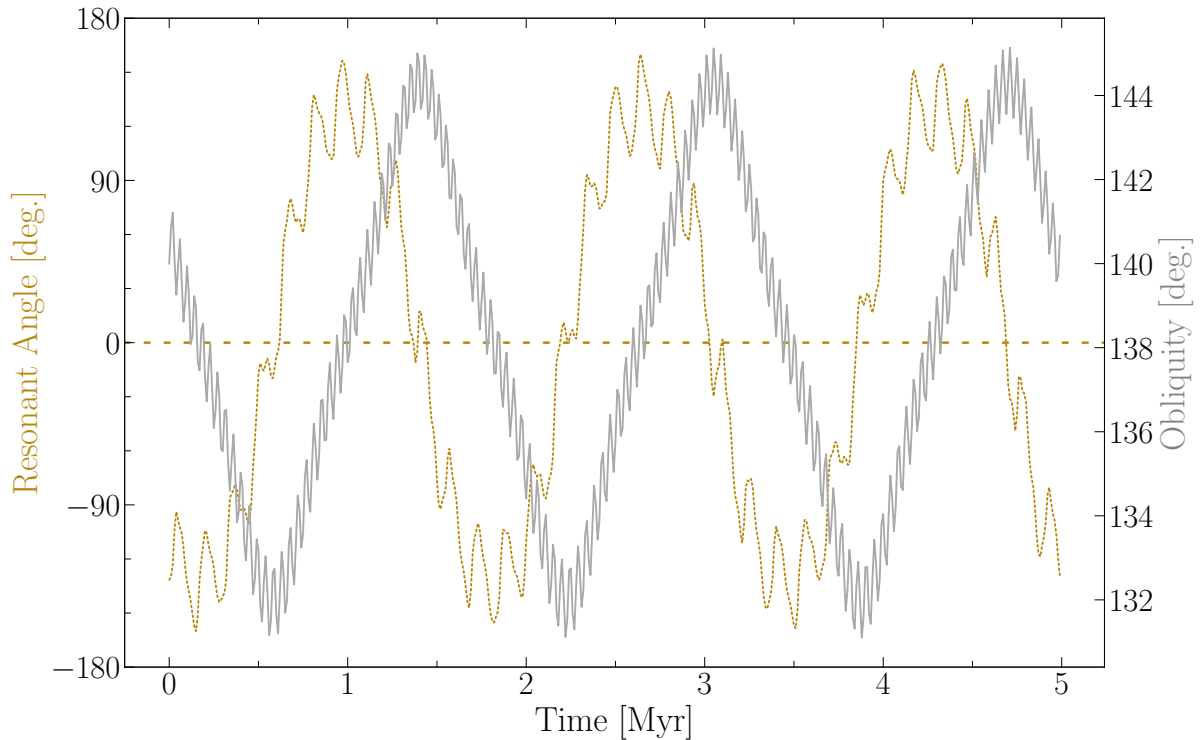
Figure 2.11 The first 5 Myr of the evolution of the resonant angle and obliquity of the Earthmoo on an orbit with an initial eccentricity of 0.3 with a 16-hour rotation period and an initial obliquity of 140°. I display the resonant angle from Equation 2.3 as the dotted gold line that pairs with the left vertical axis. The dashed horizontal gold line marks the 0° location for the resonant angle. I show the Earthmoo's obliquity as the solid silver line that pairs with the right vertical axis.

2.7 CONCLUSION

I investigate a mechanism in which orbital eccentricity acts to influence the obliquity evolution of retrograde-rotating planets. This mechanism can lead to pronounced obliquity variations in the event of a spin-orbit resonance, when a retrograde rotator's axial precession frequency becomes commensurate with an eccentricity-enabled orbital frequency. I demonstrate this phenomenon by performing numerical simulations of a toy system consisting of the Sun, a moonless Earth I call Earthmoo, and Jupiter.

I find that the predicted orbital frequency is indeed present for the cases in which Earthmoo is eccentric; this orbital frequency obeys the relationship I describe in Equation 2.2, while it shifts to higher values and grows in amplitude for greater

values of eccentricity. Over the course of the 100 Myr rigid body simulations I find that 92.5% of the Earthmoos that I test are relatively obliquity stable and experienced variations less than what I expect from orbital variations alone. However, for regions of parameter space near the predicted spin-orbit resonance locations, Earthmoo experienced pronounced obliquity variations of order 10°-30°. Generally, greater values of eccentricity led to an increase in the fraction of parameter space occupied by solutions with large obliquity variations, in which these variations also increased with increasing eccentricity.

The magnitude of these obliquity variations over this timescale is likely significant in the consideration of habitability. I do not employ a climate model in this work similar to Armstrong *et al.* (2014), Deitrick *et al.* (2018b), and others, but others have shown that large swings in a planet's obliquity could be the deciding factor between conditions that are detrimental to life, or foster it. Although the system that I consider here is purely fictional, I show the importance of the consideration of orbital eccentricity for retrograde-rotating planets and suggest that this effect may be important in future efforts to characterize planetary habitability. Retrograde rotation stabilizes obliquity under most circumstances, but the obliquity evolution of a planet is ultimately at the mercy of its system's orbital architecture. It's possible that exoplanets on significantly eccentric orbits with retrograde rotation can experience large obliquity variations.

CHAPTER 3

EXPLORING TIDAL OBLIQUITY VARIATIONS WITH SMERCURY-T [2]

3.1 SUMMARY

I introduce my new code, SMERCURY-T, which is based on existing codes SMERCURY (Lissauer *et al.*, 2012) and Mercury-T (Bolmont *et al.*, 2015). The result is a mixed-variable symplectic N-body integrator that can compute the orbital and spin evolution of a planet within a multi-planet system under the influence of tidal spin torques from its star. I validate my implementation by comparing my experimental results to that of a secular model. As I demonstrate in a series of experiments, SMERCURY-T allows for the study of secular spin-orbit resonance crossings and captures for planets within complex multi-planet systems. These processes can drive a planet's spin state to evolve along vastly different pathways on its road toward tidal equilibrium, as tidal spin torques dampen the planet's spin rate and evolve its obliquity. Additionally, I show the results of a scenario that exemplifies the crossing of a chaotic region that exists as the overlap of two spin-orbit resonances. The test planet experiences violent and chaotic swings in its obliquity until its eventual escape from resonance as it tidally evolves. All of these processes are and have been important over the obliquity evolution of many bodies within the Solar System and beyond, and have implications for planetary climate and habitability. SMERCURY-T is a powerful and versatile tool that allows for further study of these phenomena.

3.2 CONTRIBUTION STATEMENT

For this chapter, I led the investigation by carrying out the numerical experiments, performing the analysis, and writing the report. Jason W. Barnes advised me throughout by providing feedback and guidance on the approach and solution to various

---

[2]Kreyche, S. M., Barnes, J. W., Quarles, B. L., & Chambers, J. E. (2021). Exploring tidal obliquity variations with SMERCURY-T. The Planetary Science Journal, 2(5), 187.

components of the study. The coauthors Billy L. Quarles and John E. Chambers provided useful feedback to revise and improve the report.

3.3 INTRODUCTION

A planet's status within a spin-orbit resonance or chaotic region can change over time due to a variety of processes that either alter the planet's spin-precession rate or the position of the resonant orbital frequency. One process that continuously dampens the precession constants of planets is the solar tidal torque, which causes planets to undergo tidal braking in which their rotation rates slow while their obliquity evolve until eventual near zero values. Considering the impact that complex tidal obliquity evolution might have on planetary climate as they could potentially traverse many spin-orbit resonance encounters, this subject warrants further study.

I introduce SMERCURY-T (Kreyche *et al.*, 2021a), a joining of the existing code SMERCURY (Lissauer *et al.*, 2012) with elements from Mercury-T (Bolmont *et al.*, 2016) so that I can investigate these dynamic tidal spin phenomena and build a more complete picture of planetary spin dynamics. While SMERCURY utilizes its implementation of the spin Hamiltonian from Touma and Wisdom (1994) to accurately compute the orbital and rotational dynamics of a planetary system due to N-body interactions, it is not equipped to compute tidal evolution. On the other hand, Mercury-T is capable of computing the tidal evolution of a system but limits the study planetary spin evolution by neglecting planet-planet cross terms in its spin calculations. In addition, Mercury-T lacks a scheme to efficiently explore parameter space like the "ghost planet" scheme featured in the SMERCURY-T code (discussed in Section 3.4.1). Similar open-source codes such as Posidonius (Blanco-Cuaresma and Bolmont, 2017) and VPLanet (Barnes *et al.*, 2020) are also guilty of these charges. I bridge this gap by branching SMERCURY-T from SMERCURY to include modifications that allow for the complete simultaneous computation of the orbital and spin evolution of a planet while under the effects of stellar tidal spin torques.

In this chapter, I begin with Section 3.4 in which I describe the SMERCURY-T code and discuss my implementation of its new modules. Following that, in Section

3.5 I perform several experiments that demonstrate the phenomena of spin-orbit resonance crossings, captures, and chaotic crossings which express the versatility of SMERCURY-T as a tool. I conclude in Section 3.6.

3.4 METHODS

3.4.1 *The Base Code*

I present my new code, SMERCURY-T, as a modified version of its predecessor, SMERCURY (Lissauer *et al.*, 2012; Barnes *et al.*, 2016; Quarles *et al.*, 2020; Kreyche *et al.*, 2020). SMERCURY is a mixed-variable symplectic N-body integrator which is itself a modified spin-tracking version of the original MERCURY package (Chambers, 1999). Just like the code that SMERCURY-T derives from, it is capable of computing the orbital evolution of multiplanet systems while tracking the spin state of one planet and its "ghosts". The ghost planet scheme entails the simultaneous simulation of massless copies of the spin-tracked planet, in which the user assigns a unique initial spin state to each ghost planet which will evolve while its orbital evolution mimics that of the original planet. This scheme makes SMERCURY-T advantageous over similar codes by allowing for efficient exploration of parameter space, however its present implementation restricts the user to only being able to simulate the spin evolution of one system's planet at a time. SMERCURY-T is publicly available (Kreyche *et al.*, 2021a).

SMERCURY-T treats the spin computation by considering the spin-tracked planet to be an axisymmetric rigid body. Gravitational torques from the planet's star and neighboring planets exerted on the spin-tracked planet's equatorial bulge modify its obliquity. When preparing a simulation, I express the planet's spin rate by assigning it a value for its zonal gravity coefficient J_2 according to the Darwin-Radau relation (Hubbard, 1984; Murray and Dermott, 1999). This takes the form

$$J_2 = \frac{\omega_p^2 R^3}{3Gm_p}\left(\frac{5}{D} - 1\right) \tag{3.1}$$

with ω_p, R, and m_p as the planet's spin rate, mass, and equatorial radius, respectively. Here G is the universal gravitational constant and the placeholder D is short for

$$D = \frac{25}{4} \left(\frac{3}{2}\overline{C} - 1 \right)^2 + 1 \tag{3.2}$$

where $\overline{C}$ is the planet's normalized polar moment of inertia. I calculate R according to

$$R = \left[\frac{Gm_p D}{\omega_p{}^2} \left(\frac{2 - \sqrt{4 - \frac{30\omega_p{}^2}{GD\pi\rho}}}{10} \right) \right]^{\frac{1}{3}} \tag{3.3}$$

with ρ as the average density of the planet. I refer to Lissauer *et al.* (2012) for a more thorough description of this technique.

3.4.2 *Code Modifications*

In this section, I describe the modifications that I include within the SMERCURY-T package based on the alterations that I made to the base SMERCURY code. Here I include the details and implementation of the tidal spin torque module and then discuss the results of a test experiment to verify its accuracy. I also discuss my additional inclusion of a general relativity module.

TIDAL SPIN TORQUE MODULE — The most significant inclusion to the SMERCURY-T code is the tidal spin torque module. I follow the methods of Bolmont *et al.* (2015) and adopt the constant time lag tidal formulation expressed by Leconte *et al.* (2010) and others (Mignard, 1979; Hut, 1981; Eggleton *et al.*, 1998), which is valid for arbitrary values of obliquity, spin, and orbital eccentricity. Contrary to the rigid body considerations that I employ for the N-body torque computations, this model assumes that the body is made of a weakly viscous fluid (Alexander, 1973). In the future, SMERCURY-T's modular design makes it simple to implement and explore alternative tidal models. my approach differs from the aforementioned works in that I neglect orbital tides (when the tidal force works to circularize an orbit and reduce its

semi-major axis) and consider only the effects of tidal spin torque on the spin-tracked planet from its star. This choice saves valuable computation time, while still allowing for sufficient study of the behavior of planetary spin evolution in most planetary systems except the most compact ones. Readers can refer to Table 2 of Mardling and Lin (2004), or can perform quick calculations with handy equations such as those found in Rodríguez, A. and Ferraz-Mello, S. (2010) to estimate the importance of orbital tides in their desired system. I justify my study of the systems that I consider in Section 3.5 by estimating the semi-major axis damping timescale ($a/\dot{a}$) and eccentricity damping timescale ($e/\dot{e}$) to be practically infinite for the Earth-mass planet under study compared to my integration time of 4 Gyr. Another consequence of my methodology is that it is technically in violation with the law of conservation of angular momentum, since the spin-tracked planet's spin angular momentum decays while the system gets nothing back in return. The choice to neglect the effects of this feedback is acceptable for the study of planetary systems since the total angular momentum of the system will always vastly dwarf the the spin-tracked planet's spin angular momentum.

The task to modify the spin routine of SMERCURY-T to include tidal spin torques is a relatively straight-forward one. Since SMERCURY-T already integrates the summation of all of the torques felt by the spin-tracket planet's rotational bulge at each time step, all that remains is calculating the additional tidal torque within the routine. From Bolmont *et al.* (2015), the non-averaged tidal torque felt by a planet from its star goes as

$$\mathbf{N_T} = 3G\frac{m_s{}^2R^5}{r^7}k_2\tau(r\boldsymbol{\omega}_p - (\mathbf{r} \cdot \boldsymbol{\omega}_p)\mathbf{e}_r - \mathbf{e}_r \times \mathbf{v}) \tag{3.4}$$

where $\mathbf{r}$ is the radial vector between the planet at its star, $\boldsymbol{\omega}_p$ is the planet's spin vector, $\mathbf{e_r}$ is the radial unit vector, $\mathbf{v}$ is the planet's velocity vector, k_2 is its potential Love number of degree 2, τ is the constant time lag, m_s is the mass of the star, and G is the universal gravitational constant. This calculation treats the star as a point mass while the planet is made up of a reduced central point mass with two point mass bulges. Figure 1 from Bolmont *et al.* (2015) is a useful diagram that demonstrates

some of these elements. Converting this result to heliocentric coordinates allows for a final expression that conforms with the requirements of SMERCURY-T's spin algorithm. Taking the planet's spin angular momentum as **S**, the adjusted tidal torque is

$$\frac{d}{dt}\mathbf{S} = -\frac{m_s}{m_s + m_p}\mathbf{N_T} \tag{3.5}$$

As the spin-tracked planet's spin rate damps over time due to the inclusion of the tidal torque, it is necessary to update the planet's J_2 and equatorial radius at each time step to represent the reduction of its equatorial bulge. This is important not only due to the dependence of the strength of the tidal torque on R, but even more so due to the sensitive nature of the N-body spin dynamics computations to the value of J_2 as the planet's spin state evolves. I develop a scheme to update these parameters and provide the details in Appendix A. This scheme involves instructing SMERCURY-T to use the value of the planet's spin angular momentum to solve a cubic equation to ultimately determine new values for R and J_2 using Equations A.6 and 3.1.

One possible concern with the inclusion of the tidal spin torque module is that there may be scenarios in which the magnitude of the computed tidal torque is so small that it under flows machine precision, causing the planet's tidal evolution to cease entirely. I solve this issue by implementing a "tidal tolerance" input parameter that the user can specify prior to running a simulation. This parameter is a fractional value that determines a certain threshold after being multiplied by the total spin angular momentum at the current time step. If the tidal torque components exceed this threshold, then they are integrated and added to the spin vector. However, if they fall below the threshold then SMERCURY-T saves their values and adds them to a running total to be checked the next time around. A typical value for the tidal tolerance parameter that I use in this chapter is 10^{-12}.

3.4.3 *Tidal Spin Torque Module Verification*

I verify the implementation of the SMERCURY-T tidal spin torque module by simulating and comparing the results of a test system's tidal evolution to that of an alternative secular code based on the framework of Leconte *et al.* (2010). The secular code is

Planet Physical Parameters

$\overline{C}$	ρ [g/cm^3]	P_0 [hrs]	R_0 [km]	k_2	τ [sec]	ϵ_0 [deg]
0.3296108	5.5136	24	6378	0.305	698	45

Table 3.1 Physical values for the test planet that I describe in Section 3.4.3. Here I list the planet's moment of inertia ($\overline{C}$), average density (ρ), initial spin period (P_0), initial equatorial radius (R_0), potential Love number of degree 2 (k_2), constant time lag (τ), and initial obliquity (ϵ_0).

capable of solving the averaged equations of one planet's orbital and rotational tidal evolution. However, since SMERCURY-T only accounts for the effects of tidal spin torques, for a fair comparison I hold the orbital elements constant and evolve the secular code solely with the spin equations. I implement the same scheme from Section 3.4.2, detailed in Appendix A, into the secular code to similarly update the planet's equatorial radius at each time step.

The test system that I use here is a one-planet system that consists of the Sun and an Earth-mass planet with an semi-major axis of 0.2 AU and an orbital eccentricity of 0.3. This choice ensures a short integration time and demonstrates the capability of SMERCURY-T to handle large eccentricities. For both simulations, I assign this planet with a polar moment of inertia, average density, initial spin period, initial equatorial radius, potential Love number of degree 2, constant time lag, and initial obliquity according to Table 3.1. I integrate the SMERCURY-T simulation with a time step of 1.6 days ($\sim$ 5% of the inner-most planet's orbital period, my usual rule of thumb) and sample at an interval of 1000 years. The time step for the averaged equations of the secular code does not need to be as small, so I proceed with 1000 year increments. I run both simulations for 10 Myr which is more than enough time for the planet to reach tidal equilibrium.

Looking to Figure 3.1, I show a comparison between the results of the two codes for the spin evolution of the Earth-mass planet due to the effects of tidal spin torques. Examining the evolution of the planet's obliquity, spin period, equatorial radius, J_2 (initially calculated with Equation 3.1), and spin angular momentum, I show that SMERCURY-T is in good agreement with the secular code. Although there is a slight discrepancy between the extent of the planet's obliquity values near the peaks of the

plot in Figure 3.1's upper left panel, each parameter ultimately tracks and converges to the same end value with little difference between the two codes. In summary, We see that tidal spin torques cause the planet to initially experience an increase in its obliquity until its spin rate decays such that the altitudinal component of its spin angular momentum overtakes the azimuthal component, as shown in the upper and lower right panels of Figure 3.1. From there, its spin period continues to increase while its obliquity declines until it reaches tidal equilibrium when its obliquity is near zero and its spin period is that of its pseudo-synchronous period ($\sim$ 21 days here). The planet's equatorial radius shrinks by about 7 km while its J_2 reduces considerably.

General Relativity Module — I also incorporate the general relativistic (GR) force due to the post-Newtonian potential into SMERCURY-T as an optional module following section 2.2 of Bolmont *et al.* (2016). The GR force not only plays an important role with regard to the stability of a planetary system, but I reason that it can also have an indirect influence on planetary obliquity evolution. This influence stems from the GR effect that causes the precession of periapsis of planetary orbits to speed up. Bearing this in mind, GR can indirectly influence planetary obliquity by shifting the potentially resonant orbital eigenfrequencies. While these effects are important to a degree in our own Solar System, they are likely especially important for compact exoplanet systems whose planets reside deep within their star's gravitational well.

In the spirit of one famous confirmation of Einstein's general theory of relativity (Einstein, 1916), I verify the implementation of my GR module by checking the contribution of GR to the precession of periapsis of our planetary neighbor, Mercury. I compare the results of my SMERCURY-T simulation to that of the measured rate from the *MESSENGER* spacecraft reported by Park *et al.* (2017). I obtain an average value of 42.9790 ″/Julian century over the course of my 1 Myr simulation in which I used a system consisting only of the Sun and Mercury to isolate the effect of GR. Specifically, this value is the difference between Mercury's precession rate when the GR module was enabled versus another simulation when it was not. Here I set the integration
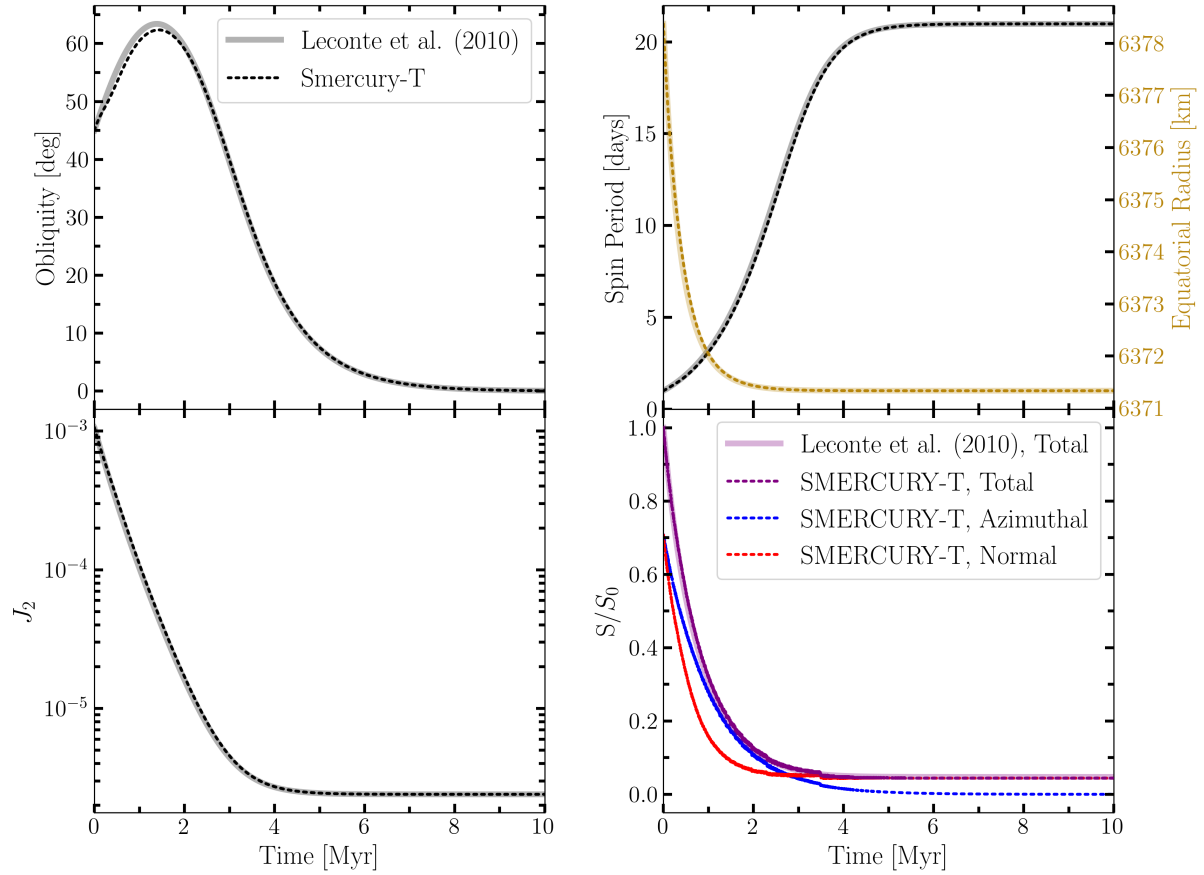
Figure 3.1 A comparison between `SMERCURY-T` (dashed lines) and the secular tidal model from Leconte *et al.* (2010) (solid lines) for the spin evolution of an Earth-mass planet orbiting at 0.2 AU with an eccentricity of 0.3. Tidal spin torques cause the planet's obliquity (top left), spin period and equatorial radius (top right), zonal gravity coefficient, J_2 (bottom left), and spin angular momentum, S/S_0 (expressed as a fraction of the total initial spin angular momentum, bottom right), to evolve over the course of each 10 Myr simulation. For the `SMERCURY-T` result, I also show the breakdown of the planet's total spin angular momentum into its azimuthal (dashed blue line) and normal components (dashed red line) with respect to the invariable plane.

time step to be 5% of Mercury's orbital period and sampled at 100 year intervals. This value is in good agreement and lies within the error bars of the Park *et al.* (2017) result.

System Orbital Parameters

System	Planet	m_p [$M_\odot$]	a [AU]	e	I [deg]	ω [deg]	Ω [deg]	M [deg]
E-J	Earth	3.003×10^{-6}	0.5	0	1	0	0	0
	Jupiter	9.54244×10^{-4}	2.5	0	0	0	0	0
E-E-J	Inner Earth	3.003×10^{-6}	0.5	0	5	0	0	0
	Outer Earth	3.003×10^{-6}	0.7	0	2.5	0	0	0
	Jupiter	9.54244×10^{-4}	3.5	0	0	0	0	0

Table 3.2 Initial values for the plantary mass (m_p), semimajor axis (a), eccentricity (e), inclination (I), argument of periapsis (ω), longitude of ascending node (Ω), and mean anomomly (M) for the Earthmoo-Jupiter (E-J) and Earth-Earth-Jupiter (E-E-J) systems that I test in this chapter. I set the mass of Sun to 1.98911×10^{30} kg.

3.5 EXPERIMENTS

In this section, I apply the code modifications discussed in Section 3.4.2 to demonstrate the usefulness and versatility of SMERCURY-T as a tool to study planetary spin dynamics. Here I showcase examples of three different scenarios driven by the effects of tidal spin torques: a spin-orbit resonance crossing, a spin-orbit resonance capture, and a chaotic resonance crossing. I enable the general relativity and tidal spin torque modules ("tidal tolerance" set to 10^{-12}) for these experiments with the exception of the initial frequency analysis runs detailed in Sections 3.5.1 and 3.5.3.

3.5.1 *Spin-orbit Resonance Crossing*

INITIAL CONDITIONS AND PRE-ANALYSIS — I design an experiment to exemplify the scenario in which tidal spin torques drive a planet to undergo a spin-orbit resonance crossing as its increasing obliquity and spin period cause its precession constant to decline over time. I choose to use a simple toy system consisting of the Sun, an Earth-mass planet initially placed at 0.5 AU, and a Jupiter-mass planet initially placed at 2.5 AU. This choice allows us to study this process appropriately while minimizing the necessary integration time thanks to the stronger presence of tides closer to the Sun. I display the masses and orbital elements of these bodies in Table 3.2 listed under system E-J, which shows that the Earth-mass planet and Jupiter-mass planet share an initial mutual inclination of $1°$.

I perform an initial simulation of the E-J system over the course of 10 Myr, sampling on an interval of 1000 years with a numerical time step of 6.46 days ($\sim$

5% of the Earth-mass planet's orbital period). For this part I am only interested in the system's orbital evolution, so I leave the GR module enabled but disable the tidal spin torque module in the interest of shaving off some computation time. Taking these results, I perform a frequency analysis routine by applying a Frequency-modified Fourier Transform (Šidlichovský and Nesvorný, 1996) to the Earth-mass planet's inclination and eccentricity vectors ($[\sin\frac{I}{2}\cos\Omega, \sin\frac{I}{2}\sin\Omega]$ and $[e\cos\varpi, e\sin\varpi]$ respectively). This process extracts the frequencies, amplitudes, and initial phases of the precessional modes that could enter resonance with the Earth-mass planet. First order resonances appear directly in the inclination series. I display these values in Table 3.3 listed under system E-J. This information allows us to compute both the location of a resonance center and its width enclosed by the separatrix as a function of a planet's precession constant and obliquity, following the procedure of Saillenfest *et al.* (2019). The simplicity of the E-J system results in the single dominant ν_1 mode in the inclination series at ≈ -22.69 ″/yr. This frequency sets the target resonance for the Earth-mass planet in the experiments I describe in Section 3.5.1 and 3.5.2.

Targeting the ν_1 mode, I initialize the Earth-mass planet so that it will begin its tidal evolution just outside of the resonance and cross paths with the resonance center some time later. Therefore I assign it with an initial obliquity of $50°$ and a precession constant of 60 ″/yr (using Equation 1.2 with a spin period of ≈ 54.7 hours and $J_2 = 2.03779 \times 10^{-4}$). These planetary characteristics are not unrealistic, and could be the aftermath of various primordial scenarios such as giant impacts. I set its initial precession angle to be $0°$, while I use the same values for its average density, normalized polar moment of inertia, potential Love number of degree 2, and constant time lag as found in Table 3.1. I run this simulation for 4 Gyr and sample every 10,000 years with the same 6.46 day time step.

Results and Discussion — I explore the results of the spin-orbit resonance crossing experiment by looking to Figure 3.2. We see that the Earth-mass planet begins with an obliquity of $50°$ and experiences benign obliquity variations of a few degrees that are primarily due to the precessional motion of its orbit. The planet's

Secular Orbital Frequencies

System	j	ν_j [″/yr]	$S_j \times 10^8$	$\phi_j^{(0)}$ [deg]	μ_j [″/yr]	$E_j \times 10^8$	$\theta_j^{(0)}$ [deg]
		Inclination Vector Series			Eccentricity Vector Series		
E-J	1	-22.69	871406	359.94	22.89	804.86	179.80
	2	0.00	1221	0.00	0.03	431	183.31
	3	-22.47	183	15.31	-9.11	15	41.66
	4	-22.90	170	149.56	-6.23	14	346.47
	5	-22.30	102	6.21	-7.45	13	235.11
E-E-J	1	-10.67	3736801	359.99	30.74	704	180.09
	2	-32.25	617977	359.84	0.03	617	180.22
	3	-3.97	8169	0.09	12.59	53	2.33
	4	-53.83	2096	179.43	9.15	14	191.46
	5	10.91	786	358.52	-98.64	8	77.37

Table 3.3 The results from my Frequency-modified Fourier Transform analysis of the inclination vector ($[\sin \frac{I}{2} \cos \Omega, \sin \frac{I}{2} \sin \Omega]$) and the eccentricity vector ($[e \cos \varpi, e \sin \varpi]$) of the Earth-mass planet in the Earth-Jupiter (E-J) system and the inner Earth-mass planet in the Earth-Earth-Jupiter (E-E-J) system, where I is the orbital inclination, Ω is the longitude of ascending node, e is the eccentricity, and ϖ is the longitude of periapsis. I show the top five values of the frequencies (ν_j), amplitudes (S_j), and phases ($\phi_j^{(0)}$) of the inclination vector, as well as the top five values of the frequencies (μ_j), amplitudes (E_j), and phases ($\theta_j^{(0)}$) of the eccentricity vector.

precession constant declines while tidal spin torques cause its obliquity to gradually increase as it approaches the resonance. Upon entering the resonance region, the planet's obliquity swings wildly in the range of $\sim 50 - 60°$. Then, at about 98 Myr into the simulation, the planet's obliquity suddenly shifts ten degrees as it crosses the resonance center and swings in a new range of $\sim 60 - 70°$. The planet then proceeds to exit the resonance and eventually converges towards tidal equilibrium with the behavior of Cassini State 1, as its obliquity draws near zero and its spin period approaches the synchronous period of ~ 129 days. The nature of these short term obliquity variations as the planet crossed through this resonance during its tidal evolution would likely be harmful toward its prospects for climatic stability and habitability. However, a true assessment of these prospects would require a more complete study that that would explore the application of a climate model.

Further examination of the resonance crossing event leads us to reason that my choice of the planet's initial precession angle ensured that it crossed through the resonance's hyperbolic point (Saillenfest *et al.*, 2021a). In other words, this behavior resulted due to the chance timing and positioning of the planet's spin axis as its spin precession wound down while the planet crossed the resonance center. Looking to Figure 3.3, I examine the evolution of the angle $\sigma = \psi - \Omega$ centered around the time of the resonance center crossing event at ~ 98 Myr, where ψ is its spin precession angle and Ω is the planet's longitude of ascending node. I treat this angle as a close approximation of the resonant angle, in which it is diagnostic of the nature of a resonance event. This angle tends to librate about $180°$ when a planet is captured in resonance in the vicinity of Cassini State 2, otherwise it usually circulates (Deitrick *et al.*, 2018a; Quarles *et al.*, 2020). Here I show that the resonant angle circulates while the planet approaches and moves away from the resonance center while an inflection point appears at the time of the crossing. This behavior reinforces that the planet was never captured into the resonance at any point in time and indeed crossed through its hyperbolic point.

Figure 3.2 I show the evolution of the Earth-mass planet's precession constant, obliquity, and rotation period over the course of 4 Gyr for the Earth-Jupiter system described in Table 3.2. Here the planet's initial precession angle was 0°. In the upper panel the green and red dots indicate the start and stop points of the simulation, while the black line traces out the spin evolution of the Earth-mass planet as tidal spin torques cause it to traverse through the pink-filled spin-orbit resonance region and across the ν_1 resonance center (Cassini state 2, solid red line). The middle panel isolates the obliquity evolution and includes an inset that showcases the dramatic shift in obliquity around the time of the resonance crossing event (highlighted in gold). The lower panel shows the evolution of the spin period over time and marks the location of the planet's synchronous period (dashed black line).

3.5.2 *Spin-orbit Resonance Capture*

INITIAL CONDITIONS AND PRE-ANALYSIS — Following the spin-orbit resonance crossing experiment described in Section 3.5.1, I now consider an alternative fate for the Earth-mass planet in which it could instead become captured into the spin-orbit resonance. Here I use the exact same initial conditions as the former experiment

Figure 3.3 I show the evolution of the Earth-mass planet's (from the Earth-Jupiter system described in Table 3.2) resonant angle over time centered about the time that the planet crossed the ν_1 resonance center. In this case, the planet's initial precession angle, ψ, was $0°$. For the resonant angle I use $\sigma = \psi - \Omega$, with Ω as the planet's longitude of ascending node.

This angle is diagnostic of the presence of a planet in a spin-orbit resonance. Here the angle circulates with a brief inflection point at the time of the crossing event (~ 98 Myr), which indicates that the planet was not captured into the resonance and instead crossed through its hyperbolic point (Saillenfest *et al.*, 2021a).

save one: the initial precession angle. Since the outcome is probabilistic based on the value of the precession angle upon its arrival at the resonance (Henrard, 1982; Saillenfest *et al.*, 2021a), I consider a slew of initial precession angles but handpick the case of the Earth-mass planet with an initial precession angle of $180°$. I stress here that although this serves my example, this is an atypical pathway toward resonance capture since the planet crosses the resonance "from above" (α/ν_1 proceeds toward unity from greater to smaller values) (Ward and Hamilton, 2004; Hamilton and Ward, 2004). I simulate this system for 4 Gyr with the same sample rate and time step as the experiment described in Section 3.5.1.

RESULTS AND DISCUSSION — I show the results of the spin-orbit resonance capture experiment by looking to Figure 3.4. While the Earth-mass planet begins on a track very similar to the crossing experiment described in Section 3.5.1, its spin

evolution takes a very different path once it enters the resonance. After about 75 Myr into the simulation, the planet crosses the resonance center and is subsequently captured into the ν_1 resonance. From here, its obliquity experiences large variations of order $\sim 20°$ as it is bound to the follow the track of the resonance's center as its precession constant declines. Eventually, at around the 350 Myr mark the separatrix of the resonance disappears and the planet exits the resonance. Since the planet's ride within the resonance led to an inefficient decay of its spin rate, the planet's obliquity then trends to greater values until peaks at about 50° and then reverses while the planet heads towards tidal equilibrium. The path that the planet's obliquity ultimately took from start to finish spanned a wide range of values with frequently large obliquity variations over short timescales. Similar to the resonance crossing experiment from Section 3.5.1, this behavior would likely be detrimental toward the planet's prospects for habitability.

Why did this experiment lead to the Earth-mass planet getting captured into the resonance while the other did not? Recalling that I set this planet to have an initial precession angle of 180° rather than the former experiment's 0°, I show the temporal evolution of its resonant angle centered around the event in Figure 3.5. Here I show that prior to the planet's encounter with the resonance center its resonant angle circulates. However, following the event the resonant angle then librates about 180°, albeit very widely, which is confirmation of the planet's capture into the resonance. This time, my choice of initial precession angle ensured that the conditions were ripe for capture into the resonance at the time of crossing.

3.5.3 *Chaotic Crossing*

Initial Conditions and Pre-analysis — For my final experiment, I design a scenario that exemplifies a chaotic spin-orbit resonance crossing. The resonance overlap criterion specifies that chaotic regions of parameter space exist in the case that two first-order resonances overlap. Therefore I now consider a system with an additional planet to introduce an additional forced inclination frequency (Saillenfest *et al.*, 2019). I present this system in Table 3.2 listed under system E-E-J, which shows my new system to consist of the Sun, an Earth-mass planet at 0.5 AU with

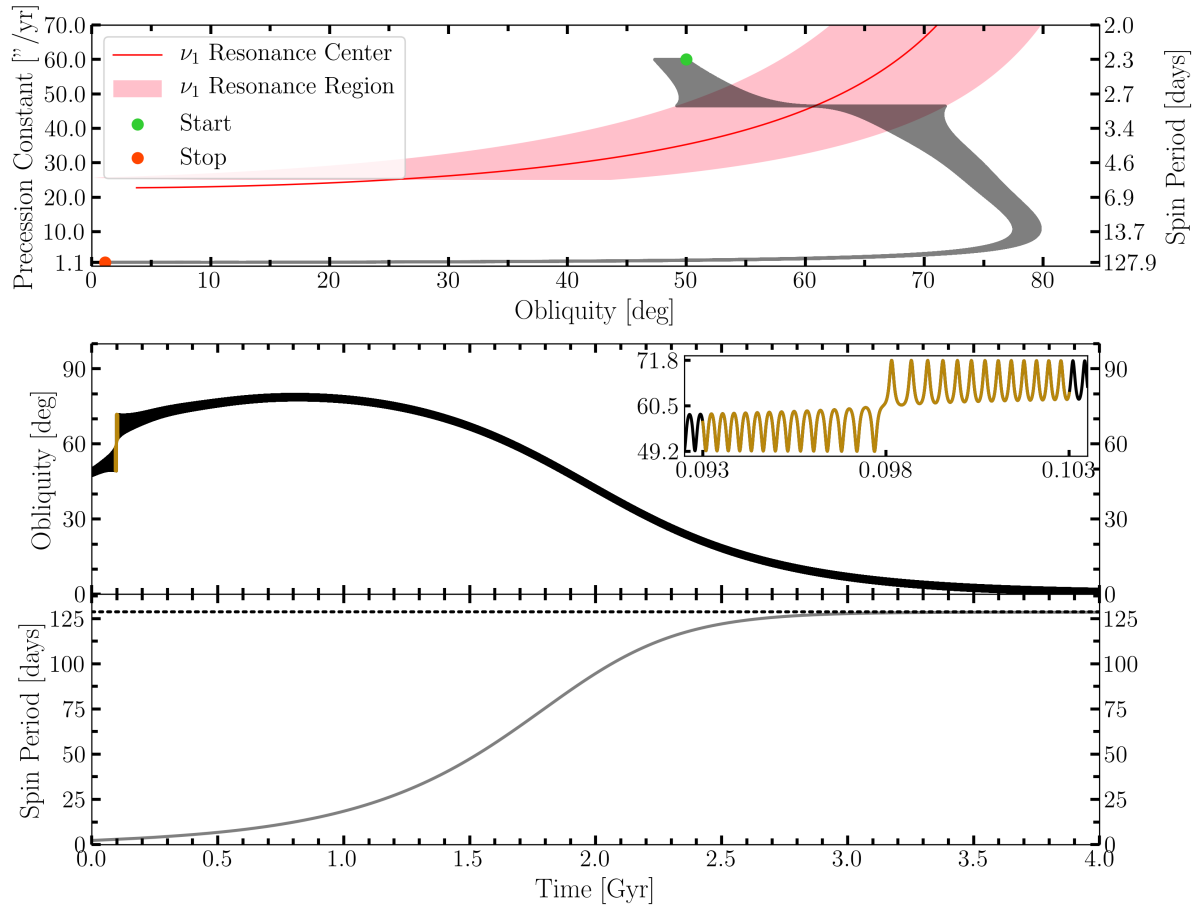Figure 3.4 Similar to Figure 3.2, here I show an alternative pathway for the evolution of the inner Earth-mass planet's precession constant, obliquity, and rotation period over the course of 4 Gyr for the Earth-Earth-Jupiter system described in Table 3.2. Here the planet's initial precession angle was $180°$. The middle panel includes an inset that showcases the shift in obliquity after the planet is captured into the ν_1 resonance (highlighted in gold).

an inclination of $5°$, an Earth-mass planet at 0.7 AU with an inclination of $2.5°$, and a Jupiter-mass planet at 3.5 AU whose orbit sits flat with an inclination of $0°$.

I conduct the same frequency analysis as described in Section 3.5.1 to extract the information on the relevant modes of this system. I display this information in Table 3.3 listed under system E-E-J. This time, my inclusion of the additional Earth-mass planet raised the "temperature" of the system, where the inner Earth shows two prominent driving frequencies in its inclination series. The first mode, ν_1, has a frequency of $\approx -10.67 \; ''/\mathrm{yr}$ and is the primary driver of the inner Earth-mass planet's orbital precession. The second mode, ν_2, has a frequency of $\approx -32.25 \; ''/\mathrm{yr}$
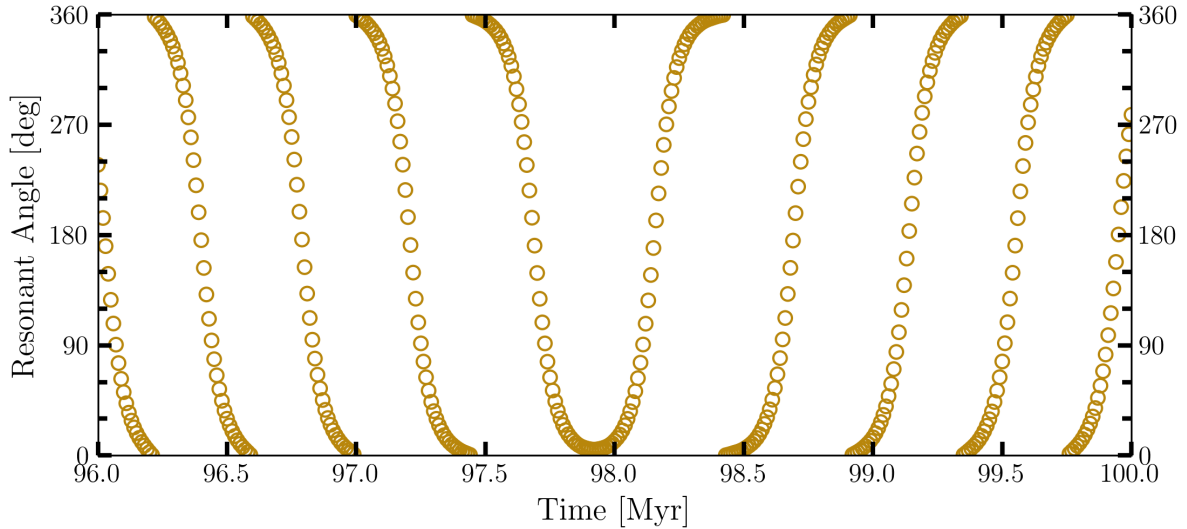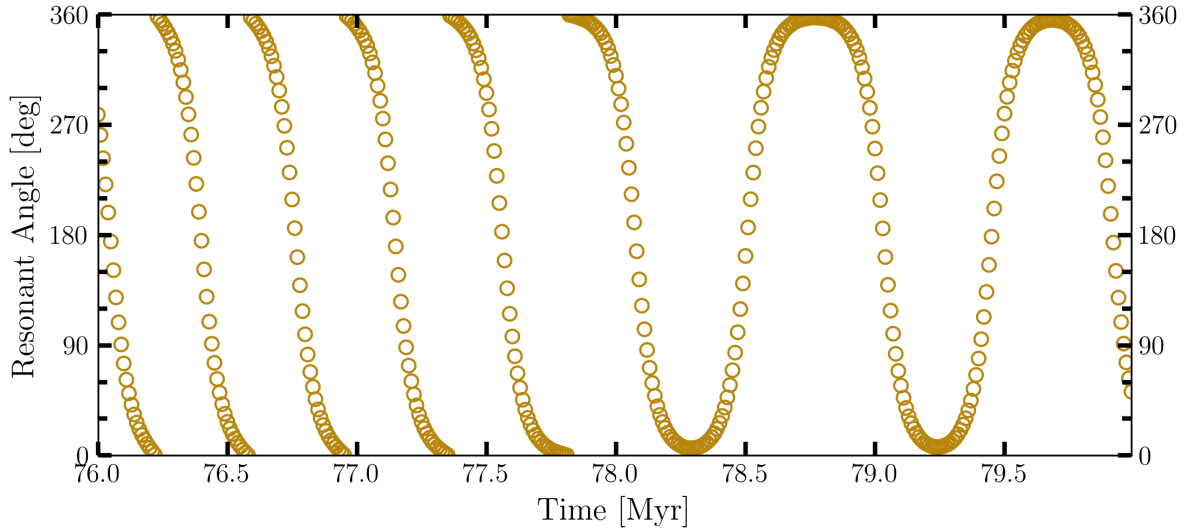
Figure 3.5 Similar to Figure 3.3, here I show an alternative evolution of the Earth-mass planet's (from the Earth-Jupiter system described in Table 3.2) resonant angle over time centered about the time that the planet crossed the ν_1 resonance center. In this case, the planet's initial precession angle was 180°. We see that this time the resonant angle transitions from circulating to librating about 180° upon the encounter, which is a strong indicator that it was captured into the resonance.

with a considerably smaller amplitude. These two frequencies have resonant widths that overlap to form a chaotic region.

I set the inner Earth's obliquity to 60° and its precession constant to 110 $''$/yr (using Equation 1.2 with a spin period of $\approx$ 29.88 hours and $J_2 = 6.83897 \times 10^{-4}$) so that it will begin its tidal evolution just outside of the ν_2 resonance region and will tidally evolve to cross into the chaotic region. The inner Earth has the same average density, normalized polar moment of inertia, potential Love number of degree 2, and constant time lag found in Table 3.1. I simulate this system over the course of 4 Gyr by sampling on 10,000 year intervals with a 6.46 day time step.

RESULTS AND DISCUSSION — I show the results of the chaotic spin-orbit resonance crossing experiment in Figure 3.6. These results share similarities with Figures 4a and 4b of Neron de Surgy and Laskar (1997a) that studied possible chaotic futures for the real Earth. Here the inner Earth begins with an obliquity of 60° and experiences variations of order $5 - 10°$ which are on par with benign variations resulting

primarily from the precessional motion of its orbit. As tidal spin torques dampen the planet's precession constant and push its obliquity towards higher values, the planet crosses into the ν_2 resonance after about 150 Myr. The resonance excites larger obliquity variations as the planet first crosses the center of the ν_2 resonance and then into the chaotic overlap region of the ν_2 and ν_1 resonance. Chaos ensues, in which the planet's obliquity violently swings as much as $\sim 60°$ in an unpredictable fashion within the range $30-90°$. This behavior spans from 200-600 Myr into the simulation until the planet finally transitions to crossing through just the ν_1 resonance and eventually exits to proceed towards tidal equilibrium where its obliquity trends towards zero and its spin period approaches the synchronous period ~ 129 days. Although this planetary system is fictional, its example of chaotic spin evolution implicates the probable catastrophic effects that this behavior could have on the planet's well-being.

3.6 CONCLUSION

In this chapter I presented my new code, SMERCURY-T, a numerical N-body integrator that is capable of computing the orbital and rotational evolution of a planet under the influence of tidal spin torques. Additionally, I included a module that adds the effects of the general relativistic force to planetary orbital evolution. I verified the proper implementation of these inclusions and showed the potential of SMERCURY-T as a powerful and versatile tool that is capable of tackling a variety of problems.

I used SMERCURY-T to perform a series of experiments to investigate different phenomena that a planet could experience due to the effects of tidal spin torques. These processes are likely important to the long-term dynamics of many planets. The spin-orbit resonance crossing and capture experiments demonstrated the possibility that a planet can take vastly different pathways which are determined purely by its initial conditions. While the resonance crossing experiment showed an example in which tidal spin torques drew a planet to encounter a spin-orbit resonance followed by an abrupt kick to its obliquity, the resonance capture experiment instead resulted in the planet engaging in a stable libration within the resonance while it was transported
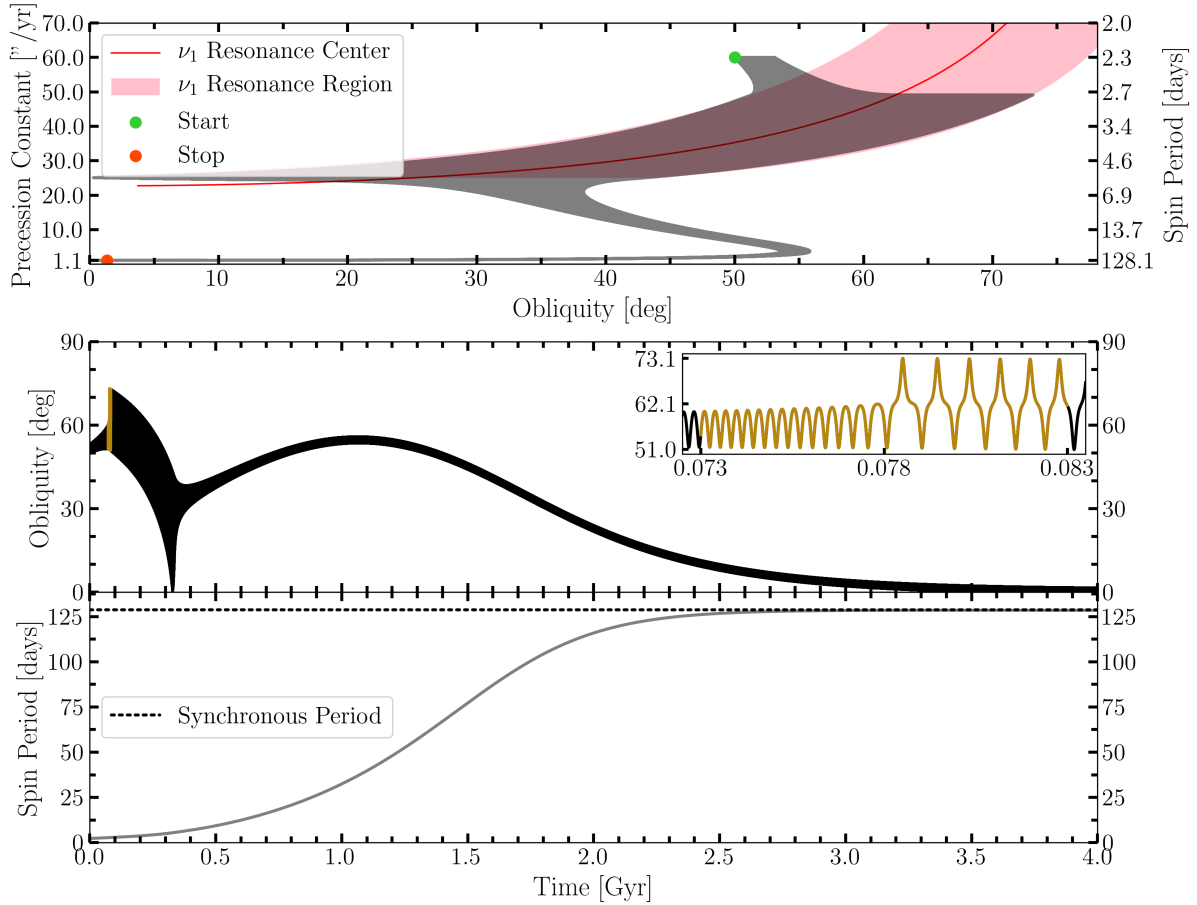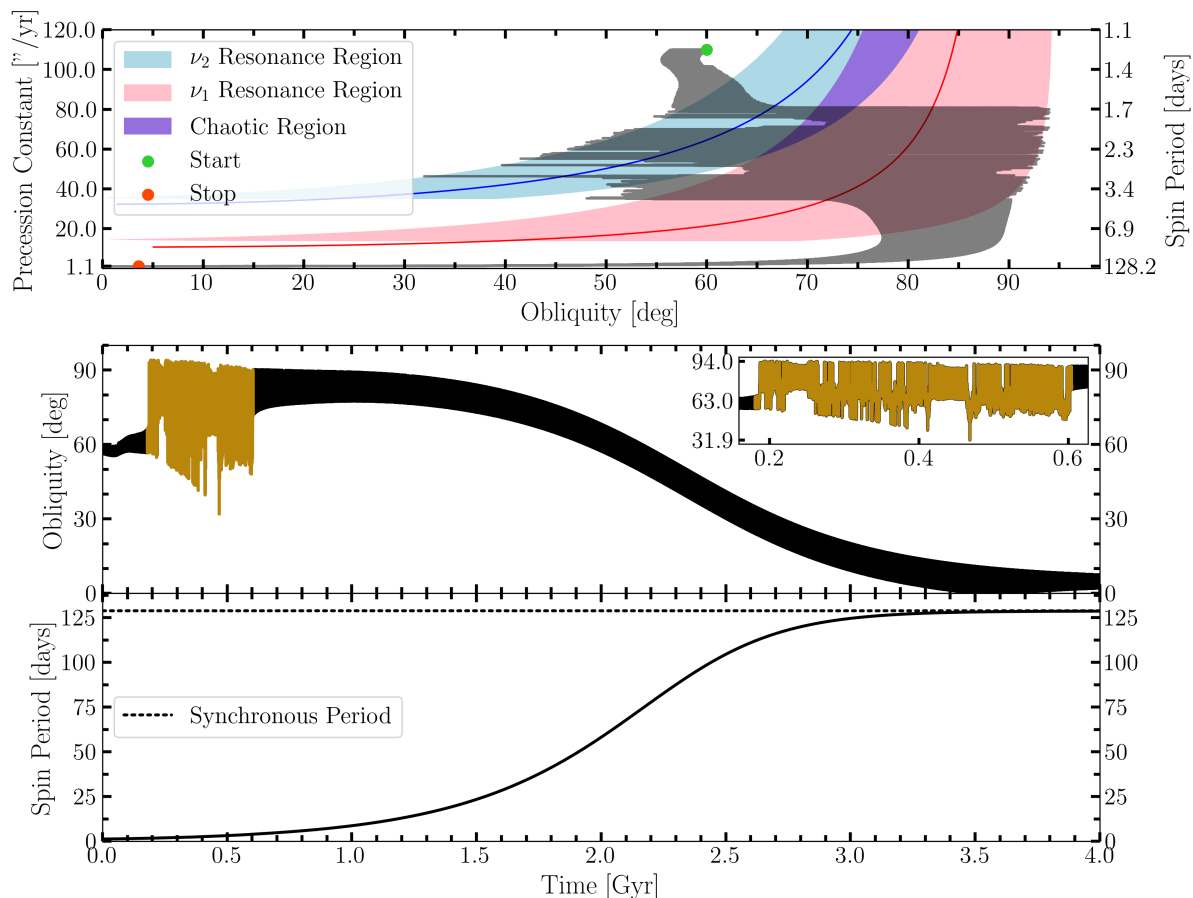
Figure 3.6 Similar to Figure 3.2, here I show the evolution of the inner Earth-mass planet's precession constant, obliquity, and rotation period over the course of 4 Gyr for the Earth-Earth-Jupiter system described in Table 3.2. The upper panel shows the region and center of the ν_2 resonance (light blue fill and solid blue line) and the region and center of the ν_1 resonance (pink fil and solid red line). The extent of their overlap exists as a chaotic region (purple fill). The middle panel includes an inset that showcases the chaotic obliquity regime from $\sim 200 - 600$ Myr (highlighted in gold).

toward lower obliquity for a period of time. I also showed the results of the crossing of a chaotic region formed by the overlap of two spin-orbit resonances. The large chaotic swings of the planet's obliquity are familiar and consistent with the dynamics of some of the bodies in my own Solar System.

Although the planetary systems that I considered in this chapter were fictional, my general study of the nature of tidal obliquity evolution demonstrates possible scenarios that may have implications for the past, present, and future dynamics of

planetary obliquity evolution. Knowing that the climatic stability and consequently, the habitability of planet, is strongly related to the nature of its obliquity evolution, understanding the dynamic role that tidal spin torques can play is critical knowledge. Large and rapid obliquity variations like those that I observed in my experiments would likely be detrimental toward a planet's climatic stability, and therefore its prospects for habitability. Although I did not investigate this claim in this chapter, an interesting avenue for future work could involve the application of a climate model to explore the potentially destructive consequences of these evolutionary pathways.

For future work, SMERCURY-T can serve as a tool to further explore tidal obliquity evolution and seek answers to questions about the planets in our Solar System and beyond. The effects of tidal spin torques are especially relevant to planets that are in close proximity to their star, such our own system's inner terrestrial planets or those in compact exoplanet systems such as TRAPPIST-1. Future characterization of exoplanet obiquities will allow for the opportunity to perform more complete assessments of their dynamical nature.

CHAPTER 4

Tidal obliquity evolution of a moonless Earth and early Venus

---

4.1 SUMMARY

A more complete understanding of how planetary obliquity (axial tilt) can evolve over time is necessary to assess the potential for habitability in planetary systems. I consider a moonless Earth and an early Venus in our own well-characterized 8-planet Solar System and perform numerical experiments using SMERCURY-T (Kreyche *et al.*, 2021b) to study the role that the solar tidal torque plays during the obliquity evolution of planets residing in a complex planetary system. The result is a variety of evolutionary pathways where the severity and timescale of the planets' obliquity variations sensitively depends on the planet's initial conditions as tidal braking causes the planets to traverse chaotic frequency space that exists as the overlap of spin-orbit resonances. Although large shifts in the obliquity are often an eventuality on the journey toward tidal equilibrium (usually Cassini State 1 with low obliquity $\sim 0°$ and synchronous rotation), both the moonless Earth and Venus generally experienced their most gradual obliquity shifts when they had retrograde rotation (having an obliquity greater than 90°), in addition to when they had long initial spin periods or initial obliquities near 90°. These results can inform how tidal obliquity variations may have or will influence both the short and long-term habitability of bodies in the Solar System as well as for exoplanets.

4.2 CONTRIBUTION STATEMENT

For this chapter, I led the investigation by carrying out the numerical experiments, performing the analysis, and writing the report. Jason W. Barnes advised me throughout by providing feedback and guidance on the approach and solution to various

components of the study. William J. Miller contributed code and effort to help generate the frequency map in the included figures, and also helped to improve the algorithm within the *SMERCURY-T* code.

4.3 INTRODUCTION

The work in Chapter 3 presented SMERCURY-T as a useful tool that enables the exploration of planetary obliquity evolution under the influence of the solar tidal torque. Although the included SMERCURY-T demonstration experiments were instructive, they involved simple planetary systems whose spin-orbit resonance frequency environment was clear cut and therefore unrealistic for real planetary systems. The intended purpose of SMERCURY-T is to consider realistic multi-planet systems with complex resonance frequency environments that may influence planetary obliquity evolution in interesting ways along their path toward tidal equilibrium. Alternative analytical or semi-analytical methods cannot study these phenomena effectively.

Since the Solar System is the only planetary system for which I can be confident that I have complete dynamical knowledge, I choose to revisit the case of a moonless Earth and early Venus as considered in previous works (Lissauer *et al.*, 2012; Li and Batygin, 2014; Barnes *et al.*, 2016). A moonless Earth (I use the nickname "Earthmoo" following Lissauer *et al.* (2012)) is an interesting problem motivated by the question of whether the Moon is necessary for the habitable conditions I enjoy on Earth thanks to its stabilizing influence in speeding its spin precession to place it comfortably distant from resonances. Although present-day Venus is a tough sell as a habitable planet, it is an interesting exercise to consider the possible evolution of its spin state in the first few Gyr after its formation when it could have been habitable under the faint young Sun. Looking to the top row of Figure 4.1, I show the orbital spectra of Earthmoo and Venus after applying a Frequency-modified Fourier Transform (Šidlichovský and Nesvorný, 1996) to their inclination vectors ([$\sin \frac{I}{2} \cos \Omega$, $\sin \frac{I}{2} \sin \Omega$] over a 100 kyr simulation of the full 8-planet Solar System. Taking these orbital frequencies as input, I show the spin-orbit resonance frequency environment in the bottom row of Figure 4.1 as a function of the planet's precession constant and obliquity. I generated

these maps following the methodology within the work of Saillenfest *et al.* (2019), and similarly display second and third-order resonances that have a weaker but potentially still important influence on planetary spin dynamics over secular time scales. Note that Earthmoo and Venus both have very similar resonance frequency maps as a result being subject to similar dynamical interactions. As pointed out and tested in previous work, retrograde rotation (having an obliquity greater that 90°) seems to be an obliquity-stabilizing characteristic due to the lack of resonances in that region (Laskar *et al.*, 1993a; Lissauer *et al.*, 2012; Barnes *et al.*, 2016). The study of the obliquity dynamics of both planets can inform our expectations for how tidal obliquity variations might influence the obliquity of other planets in extrasolar systems, especially those in closer proximity to their stars where tides would be a greater influence.

In this chapter, I perform numerical experiments to investigate tidal obliquity evolution of a moonless Earth and an early Venus. I begin with Section 4.4 in which I describe the methods that I use to approach this problem and provide the initial conditions that I use for my simulations. Then in Section 4.5 I present the results of my experiments and discuss their implications in a more general context. Finally I conclude in Section 4.6.

4.4 METHODS

4.4.1 *Approach*

I explore the nature of tidal obliquity variations for Earthmoo and early Venus by performing numerical simulations using the mixed-variable symplectic N-body integrator, SMERCURY-T (Kreyche *et al.*, 2021a,b). SMERCURY-T is a modified version of SMERCURY, (Lissauer *et al.*, 2012; Barnes *et al.*, 2016; Kreyche *et al.*, 2020; Quarles *et al.*, 2020) which itself was an upgrade to the original MERCURY code (Chambers, 1999). My code is capable of computing the orbital evolution of a multi-planet system while tracking the spin of one planet and its massless "ghosts" that are subject to both N-body gravitational torques from their planetary neighbors and the dampening tidal torque from the central body. The tidal spin torque module within SMERCURY-T
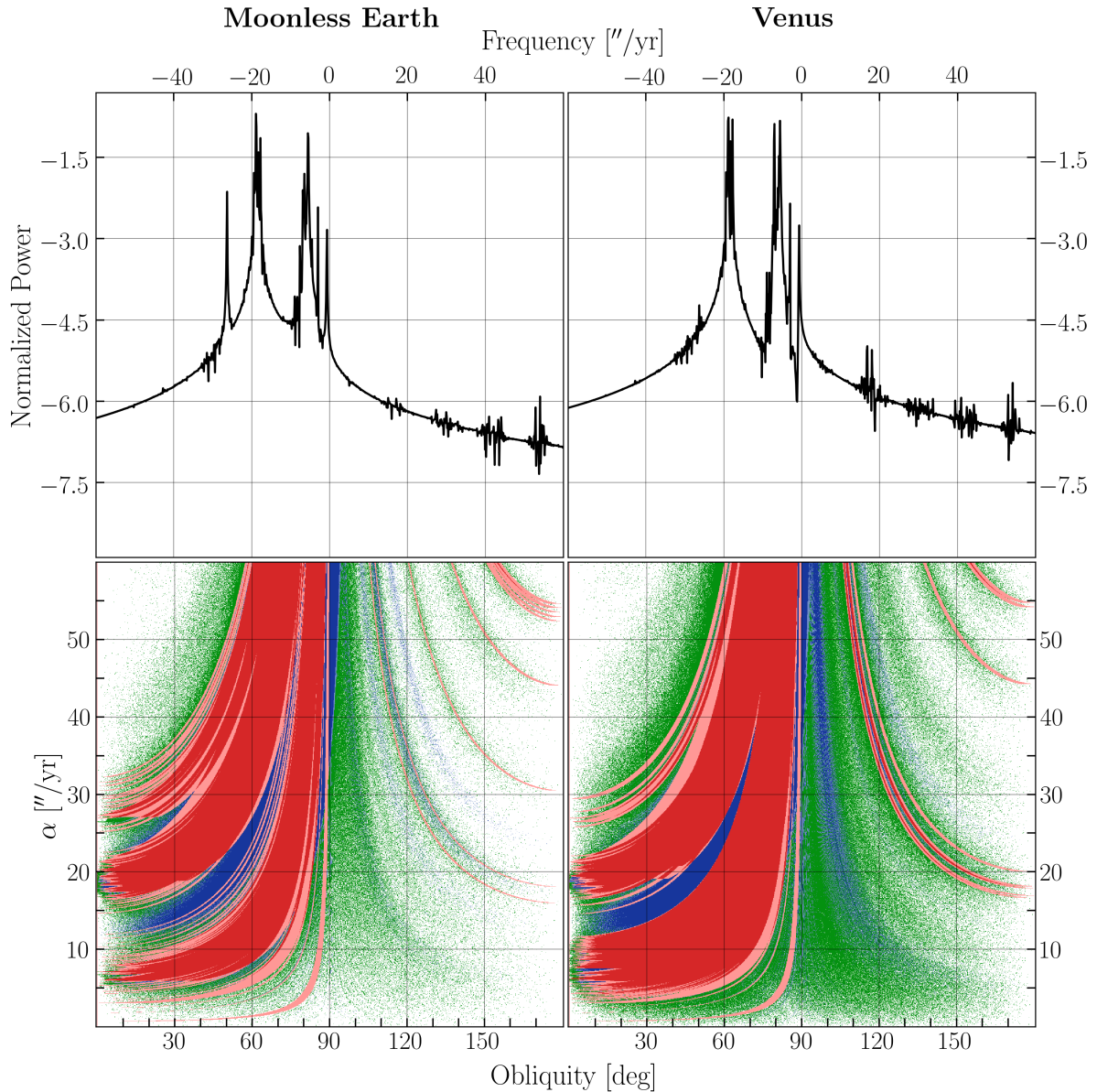
Figure 4.1 I show the normalized power spectrum of the inclination vector (top) and the corresponding spin-orbit resonance frequency map (bottom) for the moonless Earth (left) and Venus (right). The frequency maps use the 100 highest amplitude frequencies from my Frequency-modified Fourier Transform (FMFT) analysis and follow Saillenfest *et al.* (2019) to chart the locations and widths of the first (red), second (blue), and third order (green) resonances in terms of the precession constant, α, and the planet's obliquity. The darker shades of each color indicate regions of overlap between resonances of the same order.

follows the methodology of Bolmont *et al.* (2015) to incorporate the constant time lag tidal formulation from Mignard (1979); Hut (1981); Eggleton *et al.* (1998); Leconte *et al.*

(2010), however `SMERCURY-T` only computes the effect of the tidal spin torque on the spin-tracked planet since it saves valuable computation time while studying systems for which the effects of orbital tides are negligible (Kreyche *et al.*, 2021b).

I verify that my implementation of the tidal torque correctly dissipates a planet's rotational energy by performing a few quick calculations for a select Earthmoo simulation from Section 4.4.2. Here the very much Earth-like Earthmoo began with the physical properties according to Section 4.4.2, a rotation period of 24 hours, and an initial obliquity of 23.44°. Taking the difference of this Earthmoo's initial and final rotational kinetic energy at the beginning and end of the 1 Gyr simulation amounts to a $2.18 \times 10^{29} J$ loss. This is in good agreement with my analytical calculation of $2.16 \times 10^{29} J$ for the tidal energy loss over this time span using Equations 22 and 31 within Hut (1981); Bolmont *et al.* (2015), respectively.

Within a `SMERCURY-T` simulation, I treat the spin-tracked planet and its ghosts as axisymmetric rigid bodies in which gravitational N-body torques act on their rotational bulges. `SMERCURY-T` dynamically computes and updates the values for the planets' spin rates, radii, and oblateness coefficients (J_2) based on the Darwin-Radau relation (Hubbard, 1984; Murray and Dermott, 1999) in order to ensure accuracy while the tidal spin torque module modifies the spin angular momenta. I refer to Kreyche *et al.* (2021b) for a more thorough description of my methodology.

4.4.2 *Initial Conditions*

Preparing the suites of simulations for Earthmoo and Venus requires the input of the initial conditions that completely describe the orbital and spin characteristics of the planetary system. Here I simulate the full 8-planet Solar System with orbital ephemerides with respect to the J2000 epoch and ecliptic. Earthmoo is positioned at the location of the Earth-Moon barycenter. I set the simulation time step to be 5% of the shortest orbital period in the system (Mercury) which amounts to 4.4 days, while I output data at the interval of 10 kyr. Across all of my simulations I set the tidal tolerance parameter (Kreyche *et al.*, 2021b) to 10^{-14}. I detail the physical parameters that I set to characterize the spin states of Earthmoo and Venus separately in Sections 4.4.2 and 4.4.2.

MOONLESS EARTH — I initialize Earthmoo in my simulations by assigning it with the necessary physical parameters to treat it as the combined object of the Earth and the Moon with a total mass of $3.04032185 \times 10^{-6} M_\odot$, upholding the tradition as in Lissauer *et al.* (2012); Kreyche *et al.* (2020). This choice ensures that Earthmoo experiences practically the same secular interactions with its planetary neighbors as the real Earth would. Accordingly, I give Earthmoo a normalized polar moment of inertia coefficient of 0.3308, an average density of 5.51 g/cm^3, a potential Love number of degree 2 of 0.305, and a constant time lag of 698 seconds. Importantly, although the latter two values are typical tidal inputs for an Earth-like planet (Bolmont *et al.*, 2015), I greatly accelerate Earthmoo's tidal evolution by multiplying its tidal spin torque magnitude by a factor of 100 within SMERCURY-T. This operation is equivalent to reducing Earthmoo's tidal quality factor, Q, by 100, which I do in order to focus on the study of Earthmoo's long-term qualitative tidal obliquity behavior while saving valuable computation time. Looking to Table 4.1, I outline the parameter space that I explore in this study which includes a range of values for Earthmoo's initial precession constant and the corresponding initial spin period, radius, and J_2 that SMERCURY-T computes at the beginning of each simulation. Each value of precession constant is paired with several values of obliquity with the values $5°$, $25°$, $45°$, $65°$, and $85°$. Additionally, for Earthmoo I also perform simulations for the retrograde obliquity values of $95°$, $115°$, $135°$, $155°$, and $175°$. Considering the spin-orbit resonance frequency space for Earthmoo in Figure 4.1, these parameter space choices allow us to explore a variety of different outcomes.

VENUS — I largely explore the same parameter space for the Venus simulations as I do for Earthmoo in Section 4.4.2, noting their similar resonance frequency space in Figure 4.1. One key distinction is that of course the mass and average density of Venus differ, and are instead $2.448327885 \times 10^{-6} M_\odot$ and 5.204 g/cm^3, respectively. Similar to Barnes *et al.* (2016), I actually use the same normalized polar moment of inertia as Earthmoo, since a potentially habitable early Venus would have likely had a different internal structure than present day. For the same reason, I also use the Earthmoo value for Venus's k_2 while assigning the same amplified constant time

Planet Initial Spin Parameters

Planet	$\alpha\ ['' /yr]$	P [hr]	R [km]	J_2
Earthmoo	10	41.29	6400.75	3.61×10^{-4}
	20	20.71	6407.92	1.44×10^{-3}
	30	13.89	6419.86	3.22×10^{-3}
	40	10.50	6436.48	5.69×10^{-3}
	50	8.48	6457.73	8.48×10^{-3}
Venus	10	115.40	6067.53	4.89×10^{-5}
	20	57.72	6068.45	1.96×10^{-4}
	30	38.51	6069.99	4.40×10^{-4}
	40	28.91	6072.14	7.81×10^{-4}
	50	23.16	6074.90	1.22×10^{-3}

Table 4.1 Initial values for the spin period (P), equatorial radius (R), and oblateness coefficient (J_2) computed according to the Darwin-Radau relation (Kreyche *et al.*, 2021b) which correspond to the assigned value of precession constant (α) for both Earthmoo and Venus.

lag value to accelerate its tidal evolution. Since my goal is to explore the spin-orbit resonance frequency environment of Venus as evenly as possible, I test the same five initial precession constant as I do for Earthmoo, although the corresponding initial spin periods, radii, and J_2 differ due to the different physical properties of Venus (see the lower half of Table 4.1). I pair the same initial obliquity values from Section 4.4.2 to each precession constant which allows for a thorough exploration of the spin-orbit resonance frequency environment.

SETTING THE INITIAL SPIN-PRECESSION ANGLE — The spin-precession angle ψ, the angle that defines the azimuthal orientation of a planet's spin axis, plays an influential role in determining the outcome of a planet's dynamic interaction with a spin-orbit resonance. Although the conditions for a planet to enter resonance strictly requires the spin precession frequency and orbital frequency to be commensurate, the angle that ψ makes with the orbital frequency's phase angle can determine the outcome of the resonance response for the planet to either cross the resonance or potentially become captured about it (Deitrick *et al.*, 2018a; Saillenfest *et al.*, 2019; Su and Lai, 2020; Kreyche *et al.*, 2021b). Therefore while the spin-precession angle constantly circulates at a rate determined by Equation 1.1, the initial ψ value set at the beginning of a simulation is especially important. The works of Lissauer *et al.* (2012) and Barnes *et al.* (2016) conducted various experiments that examined the effects of spin chaos as they varied ψ at several increments. In this study, looking to Figure 4.2 I conduct a similar experiment to better understand the effect of varying ψ with the added effect of the solar tidal torque that was not included in the aforementioned works.

For this experiment, I consider an Earthmoo that has similar characteristics to that of the present-day Earth by setting an initial 24 hour spin period and obliquity of 23.44°. Looking to Figure 4.2, I run 1 Gyr simulations of twelve copies of Earthmoo with varied initial spin-precession angles ranging from 0 to 330 degrees in 30 degree increments. Thinking big picture, the spin period and obliquity of each Earthmoo ultimately evolves along a similar arc in which the obliquity undergoes frequent shifts while traversing the resonant frequency space and gradually increases toward high

values around 70°. This behavior occurs while the ever-present solar tidal torque dampens each Earthmoo's spin period, and consequently its precession constant. However, each Earthmoo in this experiment does experience a unique evolution where some suffered more rapid and severe obliquity variations than others due to their differing initial spin-precession angles. Contrasting the $\psi = 90°$ and the $\psi = 330°$ for instance demonstrates what would likely be a stark difference on impact toward climatic stability and potential for habitability, where Earthmoo's obliquity in the former case experiences a massive shift from about 20 to 60 degrees near the $\alpha = 8 \, ''/yr$ mark while Earthmoo's obliquity in the latter case evolved more gradually within the 30 to 60 degree range.

From this experiment I conclude that it would not be feasible to systematically set the initial spin-precession angle of the spin-tracked planets in consideration of the complex chaotic resonant frequency space in addition to the need to reduce parameter space and computation time. Therefore for the remainder of experiments in this study I assign randomized values for the initial spin-precession angles according to a uniform distribution which would realistically be random anyways for real planetary systems.

4.5 RESULTS AND DISCUSSION

4.5.1 *Moonless Earth*

In this section, I perform numerical experiments to study the tidal obliquity evolution of a moonless Earth in order to gain a qualitative sense for the impact of its initial conditions on its outlook for climatic stability and habitable conditions.

INITIAL PROGRADE OBLIQUITY — Based on my discussion in Section 4.3 of Earthmoo's spin-orbit resonance frequency environment, it is evident that there are many perilous regions of parameter space for prograde obliquities which include the chaotic overlap of strong obliquity-exciting resonances. Looking to Figure 4.3, I show the results of a set of SMERCURY-T simulations which sweep a variety of initial spin states that each include differing values for Earthmoo's initial precession
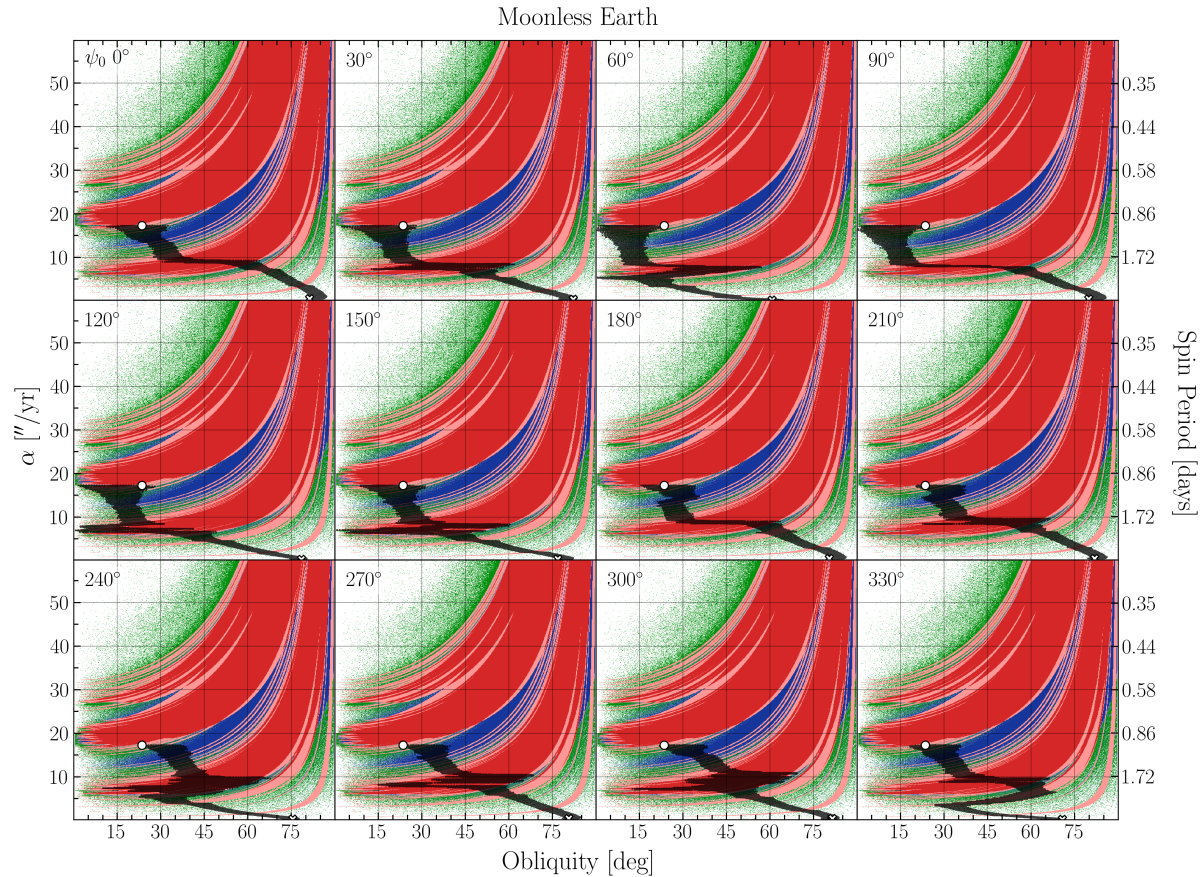
Figure 4.2 I show a grid of results for the tidal obliquity evolution over the course of 1 Gyr of an Earthmoo with the same initial spin period and obliquity as the present-day Earth. However, I vary the value of Earthmoo's initial spin-precession angle, ψ_0, in 30 degree increments from 0 to 330 degrees (I display ψ_0 in the upper left corner of each panel). The black lines chart the spin evolution of each Earthmoo in terms of the precession constant, α, the corresponding spin period (mapped to the right-hand axis), and its obliquity with the spin-orbit resonance frequency map from Figure 4.1 as a backdrop for context. The white circle and cross mark the beginning and end of each simulation, respectively.

constant, obliquity, and (randomized) spin-precession angle. Figure 4.4 serves to complement Figure 4.3 by showing the time evolution the same batch of simulations in order to provide important the context needed to properly judge the impact that the subsequent obliquity variations may have on habitability. Although my simulations investigate accelerated tidal evolution would likely differ in detail compared to true timescale simulations (due to the timing of probabilistic resonance encounters

(Henrard, 1982; Saillenfest *et al.*, 2021a)), it remains instructive to study the big picture trends.

We see a rich variety of pathways along which Earthmoo's spin state evolves as it proceeds towards its eventual tidal equilibrium end state (Cassini State 1). This end state entails near zero obliquity and a dampened spin rate with a synchronous or pseudo-synchronous period, however Earthmoo does not yet meet this end even after 1 Gyr of accelerated tidal evolution. First looking to the slowest rotators with initial precession constants of 10 $''/yr$ found in the bottom row of Figure 4.3, these Earthmoos begin as the closest to tidal equilibrium due to their reduced spin angular momentum. Nonetheless, these Earthmoos with initial obliquities of 5, 25, and 45 degrees initially reside within one of the large chaotic regions of spin-orbit resonance and subsequently experience shifting envelopes of obliquity variations of order 10-50 degrees within the first 100 Myr as their spin-precession rates decline. Looking to the larger initial precession constant cases, Earthmoos with low to moderate obliquity were placed in various regions of frequency space and usually experienced similar chaotic obliquity variations, but for longer periods of time up to the first $\sim$ 500 Myr of their simulations since the tidal torque must act on the longer before their chaotic zone exit. One particularly striking case is that of the Earthmoo with an initial obliquity of 5° and an initial precession constant of 40 $''/yr$, which experienced a rapid $\sim$ 20 million year 60° kick in obliquity at about the 100 Myr mark. Another notable example is the 30 $''/yr$ initial precession constant, 65° initial obliquity Earthmoo that showcased an example of resonance capture as its obliquity and precession rate decayed along the track of a low-frequency first-order resonance for the first $\sim$ 400 Myr. Most of these cases had Earthmoos that eventual resigned to more gradual and steady increases in obliquity during the second half of their simulation once their spin-precession rates distanced the planets away from the proximity of strong resonances. However, the aforementioned rapid and chaotic obliquity variations of these Earthmoos would likely be destabilizing to their climate and prospects for habitability.

Thinking further about habitably favorable conditions that might mean stable periods of obliquity, I can look to some of the Earthmoos that began with more

extreme initial conditions. For instance, the upper left of Figures 4.3 and 4.4 shows Earthmoos that began with large spin-precession rates that enable a brief ~ 100 Myr period of constrained $5°$ obliquity variations before declining into chaotic frequency space. On the other hand, the Earthmoos with initial obliquities of $85°$ show a mix of both resonance capture encounters and steady obliquity evolution (seen clearly as relatively flat lines in Figure 4.4) while their precession rates decline in straight-forward manner away from strong resonance.

Initial Retrograde Obliquity — I will now explore the results of the numerical simulations of the Earthmoos with initial obliquities that were retrograde. Previous studies suggest that retrograde rotation (having an obliquity greater than $90°$) is a largely obliquity-stabilizing influence (Laskar and Robutel, 1993b; Lissauer *et al.*, 2012; Barnes *et al.*, 2016) with the exception of resonant interactions in high eccentricity systems (Kreyche *et al.*, 2020). A look to the power spectra and resonance frequency maps in Figure 4.1 show that retrograde rotators only have a few weak clusters of positive frequencies to interact with, which should translate to similar findings. This study will check if the trend of stabilizing retrograde rotation holds for planets undergoing tidal obliquity evolution.

Looking to Figure 4.5, I show the results of a batch of simulations in which I assigned Earthmoo with the same precession constants as in Section 4.5.1 but pair them with an initial retrograde obliquity instead. Additionally, Figure 4.6 shows the time evolution of this batch of simulations for temporal context. Here we see a stark contrast across the board for the retrograde obliquity evolutionary tracks in comparison to the prograde obliquity runs. The initial retrograde Earthmoos do indeed generally experience constrained obliquity variations of just a few degrees over short million year timescales, noting the weak slopes in Figure 4.6 that progress to stronger slopes with increasing initial obliquity. Due to their retrograde rotation, the solar tidal torque works to reduce Earthmoo's obliquity and spin period in unison in which the planet evolves toward an eventual tidal equilibrium state with low obliquity and synchronous or pseudo-synchronous rotation that requires their spin pole to flip in orientation from beneath its orbital plane to above. We see the

Figure 4.3 Similar to Figure 4.2, but here I show a grid of results for the tidal obliquity evolution of a variety of Earthmoos over the course of 1 Gyr by varying the initial values of the precession constant and obliquity. Each row and column share the same initial value for the initial precession constant and obliquity, respectively. I indicate each Earthmoo's initial spin-precession angle, ψ_0 in the upper left corner of each panel, which were uniformly randomized to take values between 0 and 360 degrees.

beginnings of this orientation flip for the bottom row Earthmoos of Figure 4.5 which became prograde in the last $\sim$ 200 Myr of their simulations. I note that for all of the retrograde obliquity cases, the scattered weak first-order resonances and second and third-order resonance regions do not appear to have any meaningful influence on their spin state evolution.
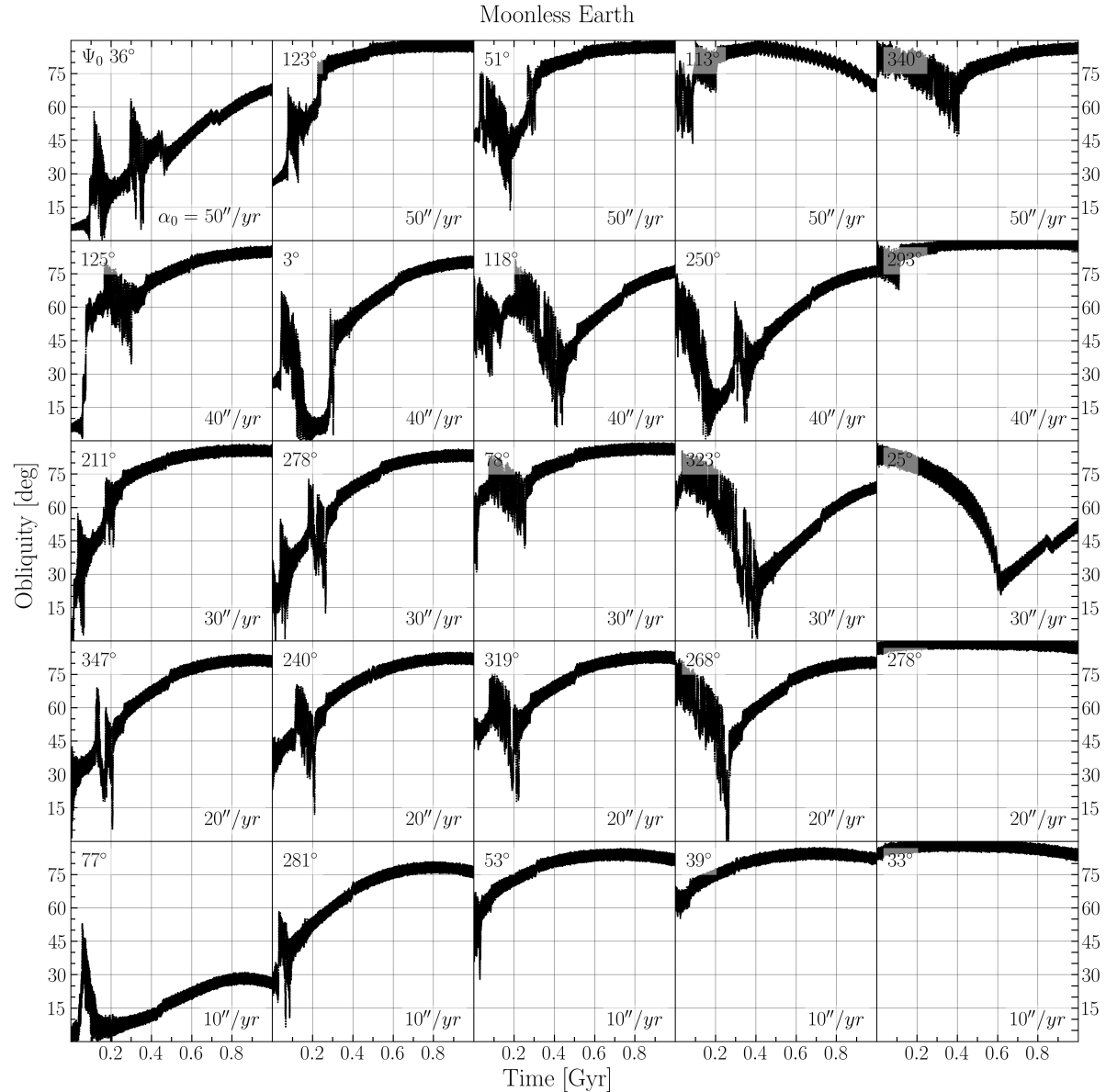
Figure 4.4 I show the tidal obliquity evolution as a function of time for each Earthmoo within the same grid of simulations as Figure 4.3. I again display the value of Earthmoo's initial spin precession angle, ψ_0 in the upper left corner of each panel.

Considering implications for habitability, here the Earthmoos with initial obliquities of $95°$ stand out as the most advantageous due to their minimal variation both on short timescales as well varying a total of 5-10 degrees over the entire 1 Gyr simulation. The initial $180°$ Earthmoos also enjoy a prolonged period of minimal shift of just 10-15 degrees for the first 400 Myr of their simulations prior to the onset of a quickening pace. The retrograde Earthmoos found in the middle panels of Figure 4.5

with intermediary obliquities shift through a much larger range of obliquities during the initial spin period damping phase, albiet still perhaps preferred to the chaotic behavior of various prograde Earthmoos in Section 4.5.1.

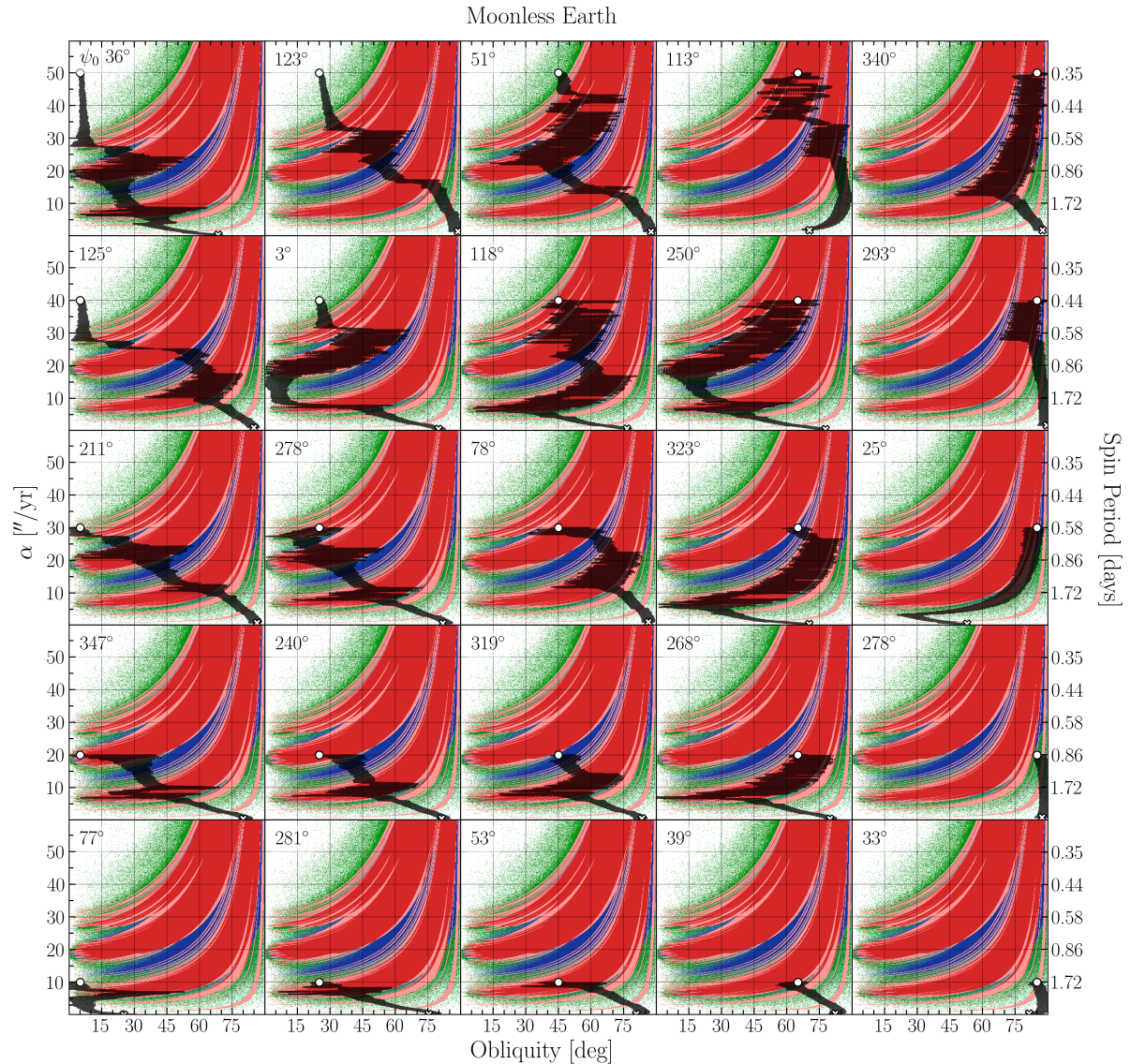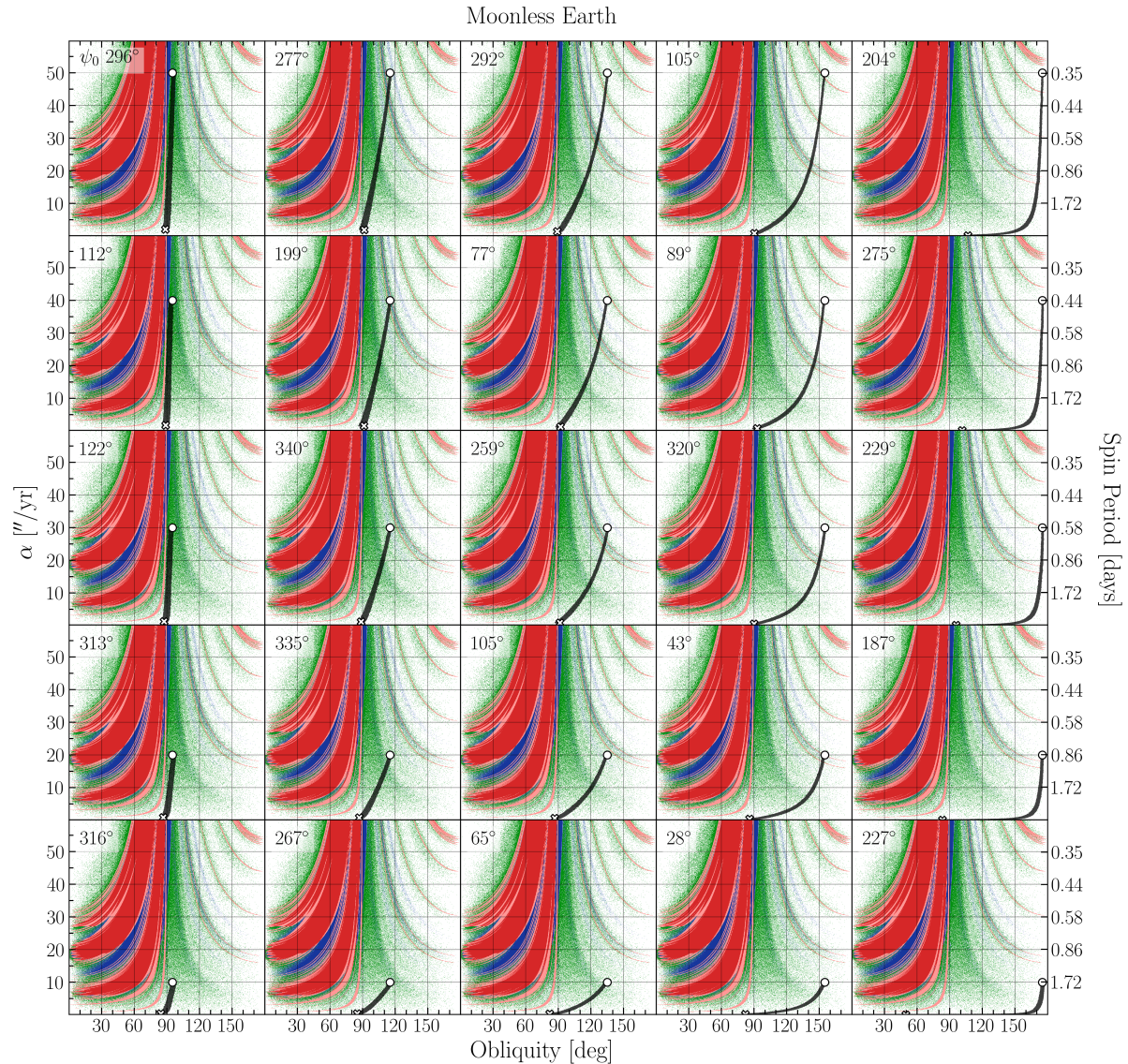

Figure 4.5 Similar to Figure 4.3, but here I show a grid of results for the tidal obliquity evolution of retrograde Earthmoos with initial obliquities greater than 90° over the course of 1 Gyr. The rows of panels explore the same variety of initial precession constants, while Earthmoo's initial spin-precession angle was again randomized on a uniform distribution.
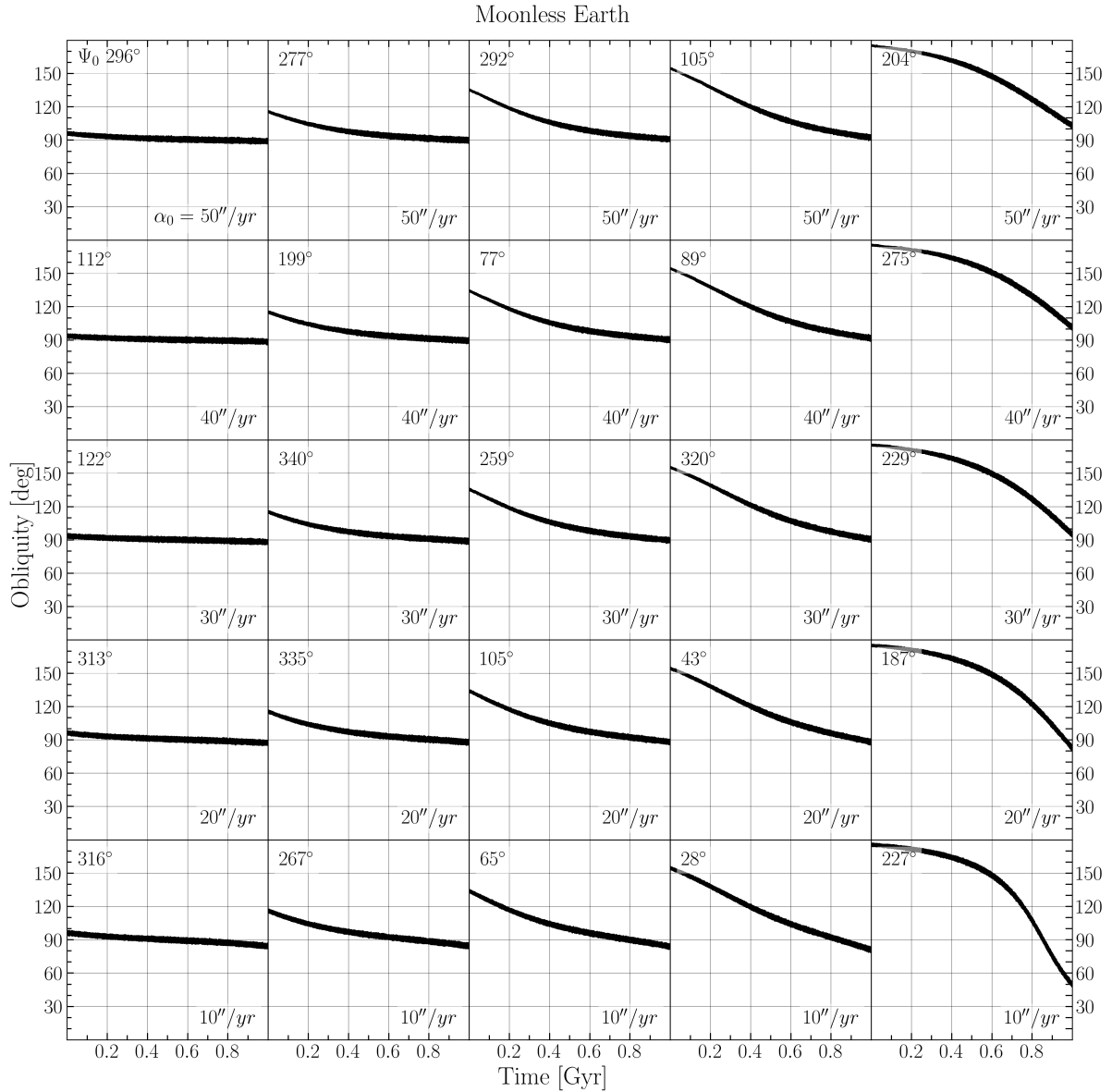
Figure 4.6 I show the tidal obliquity evolution as a function of time similar to Figure 4.4, but for the retrograde Earthmoo simulation batch featured in Figure 4.5.

4.5.2 *Early Venus*

In this section, I perform numerical experiments for a potentially habitable early Venus in order study its tidal obliquity evolution as I did for Earthmoo in Section 4.5.1.

Initial Prograde Obliquity — Considering the resonance frequency space of Venus in Figure 4.1, I note that it is qualitatively similar to that of Earthmoo's and encompasses many similar areas of linked chaotic resonance regions. Therefore we should expect that Venus should experience many of the same trends and tidal obliquity behavior as we studied for Earthmoo in Section 4.5.1. One notable difference is that while I sweep the same parameter space for Venus as I did for Earthmoo, due to its closer position to the Sun the Solar tidal torque is stronger and will cause Venus to tidally evolve much quicker even over the shortened 500 Myr time span. Looking to Figure 4.7, I show the results of the tidal obliquity evolution of Venus for a variety of initial precession constants and obliquities. Figure 4.8 complements this results by showing the time evolution of Venus's obliquity for the same batch of simulations.

The obliquity evolution of Venus indeed follows many of the same trends in behavior as noted for Earthmoo in Section 4.5.1. In a much denser timeline due to the stronger tidal torque, the Venus cases for low to moderate obliquity of all initial precession constants experience various forms of chaotic obliquity evolution encounters. Figure 4.8 shows that most of this chaotic behavior regime occurs within the first ~ 100 Myr of the simulation before each Venus exits the chaotic resonance zone and proceeds along a familiar track of increasing obliquity followed by a unified decline with its spin-precession rate. These results include features of loose resonance capture such as the $85°$ initial obliquity, $30 \, ''/yr$ initial precession constant Venus, in which capture here could possibly be fortunate in confining its obliquity variations and transporting it toward lower obliquity for about 750 Myr before its exit. One standout example of rapid large obliquity variations includes a $\sim 40°$ swing over just ~ 5 Myr for the $25°$ initial obliquity, $50 \, ''/yr$ initial precession constant Venus. The decline from the peak of a Venus tidal obliquity track to its near zero value near the end of its tidal evolution happens over just a few Myr so that we see their end state by the time the simulation completes.

While the tidal obliquity evolution of low to moderate obliquity Venus involves large and often rapid obliquity variations, the high obliquity cases of Venus at $85°$ are comparatively much obliquity stable for the first 200 Myr. Specifically, there are periods of time when their obliquity varies only 5-$10°$ which stands out in a similar

way as the Earthmoo results. Looking to Figure 4.8 however, the Venus case with an initial precession constant of 40 $''/yr$ and initial obliquity of 85° is a notable exception in which its evolution included a rapid swing from about 50° to 5° over about 10 Myr before returning to a high-obliquity state following its exit of the chaotic resonant region. Similar to Earthmoo, Venus also has a similar safe harbor region shown in the upper-left of Figure 4.7 where there is an absence of resonant regions and only small obliquity variations of order 5° occur before entering the chaotic zone in a few tens of millions of years.

INITIAL RETROGRADE OBLIQUITY — I expect that the initial retrograde obliquity cases of Venus should qualitatively be very similar to the Earthmoo results in Section 4.5.1 due to the similar lack of resonance features we observe in Figure 4.1. For the sake of brevity, I refer to my discussion of retrograde Earthmoo cases for the same general behavior, the quicker tidal evolution of Venus due to its closer positioning to the Sun again allows us to see the complete journey to tidal equilibrium. Look to Figure 4.9 for the tidal spin evolution results of Venus as the tidal torque drives them from high initial obliquities to eventual low obliquities that decline with their spin-precession rates. This amounts to an extreme difference in obliquity over the course of each 500 Myr simulation, although I note that on short timescales the obliquity variations are constrained to small fluctuations of order 5°. Figure 4.10 complements these results by providing important context on the time evolution of the tidal evolution. The general trends suggest that in terms of prolonged periods of obliquity stability, the Venus cases with initial obliquities of 95° maintained a steady slope for about 150 Myr until their rotation rates declined to the point of a unified rapid decline.

4.6 CONCLUSION

I investigated the tidal obliquity evolution of a moonless Earth and a potentially habitable early Venus with the use of the N-body numerical integrator SMERCURY-T. In my experiments I performed numerical simulations of these planets' accelerated
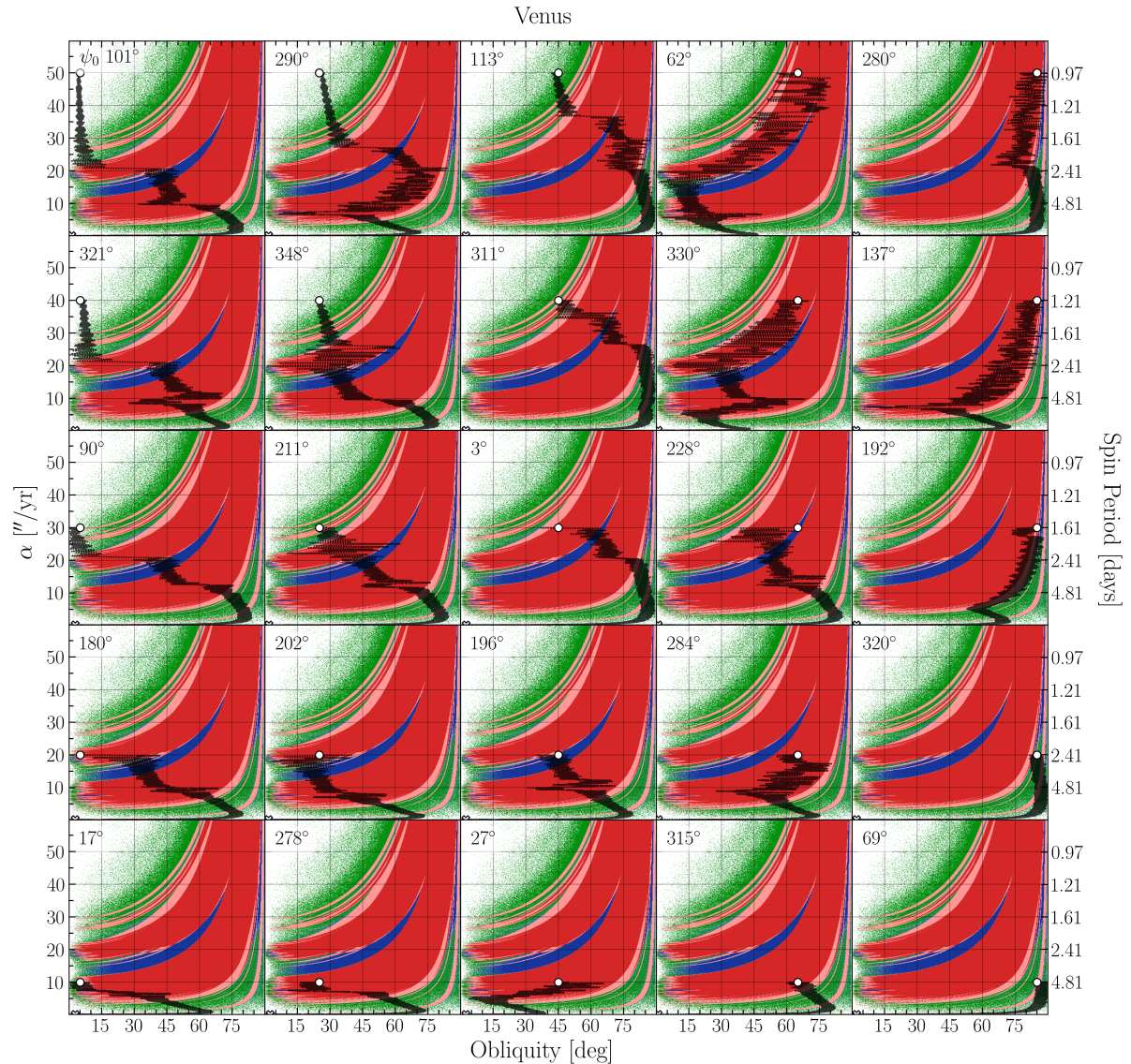
Figure 4.7 I show a grid of results for a variety of tidal obliquity simulations for Venus over the course of 500 Myr, similar to my presentation of the Earthmoo results in Figure 4.3. Here the spin-orbit resonance frequency map for Venus from Figure 4.1 is a backdrop in each panel to serve as spatial context, while the mapped spin period values appropriately map according to Venus's physical parameters.

tidal spin evolution which allowed for a thorough exploration of their complex spin-orbit resonance frequency space while vastly reducing the computation time required for them to reach tidal equilibrium or well on the way to it. Although this approach forfeits my ability to reasonably forecast the true evolution of these bodies due to obliquity chaos (Lissauer *et al.*, 2012), these cases serve as useful examples to better
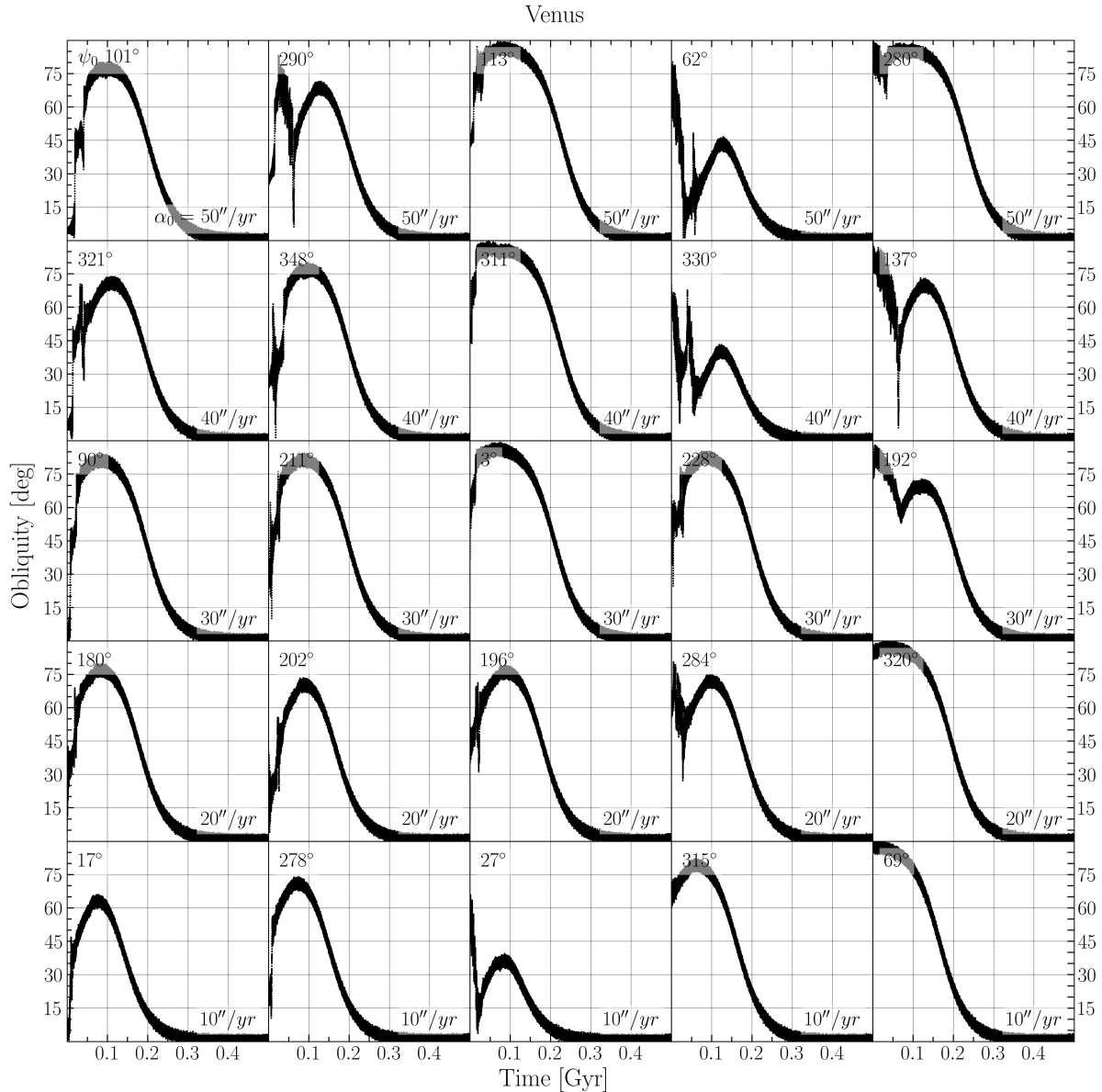
Venus

Figure 4.8 I show the tidal obliquity evolution of Venus over a time for the same grid of simulations as Figure 4.7, similar to the use of Figure 4.4's display of the Earthmoo results.

understand the qualitative pathways and behaviors that possible exoplanets could take in real complex planetary system similar to the Solar System.

With regard to the findings from my experiments, the inclusion of the solar tidal torque in conjunction with the orbital and N-body spin interactions proves to have great influence on the evolution of a planet's spin state. Although no two spin-state tracks were the same, due to their similar spin-orbit resonance frequency
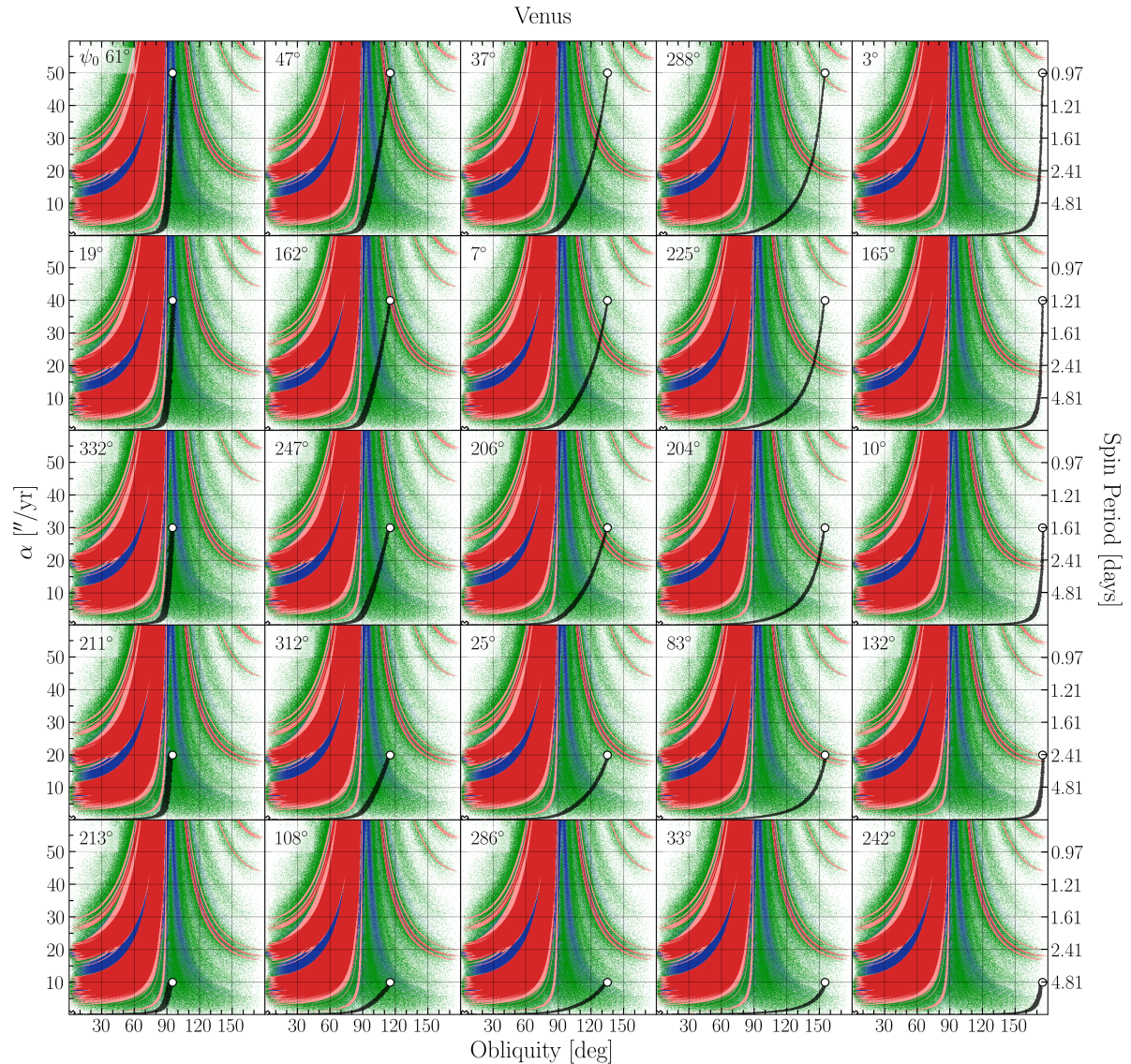
Figure 4.9 Similar to Figure 4.7, but here I show a grid of results for the tidal obliquity evolution of retrograde Venus with initial obliquities greater than 90° over the course of 500 Myr.

space, Earthmoo and Venus both experienced similar tidal obliquity evolutionary trends dependent on the initial conditions that define their spin states. Here the tidal spin torque acted as a constant drain that continuously saps their angular momentum while often causing an initial period of increasing obliquity (Barnes and Fortney, 2003), causing them to traverse their spin-orbit resonance frequency environments. This phenomenon is less explored due to the often considered "static" rotation periods in many obliquity studies. Along the way, frequent large and rapid
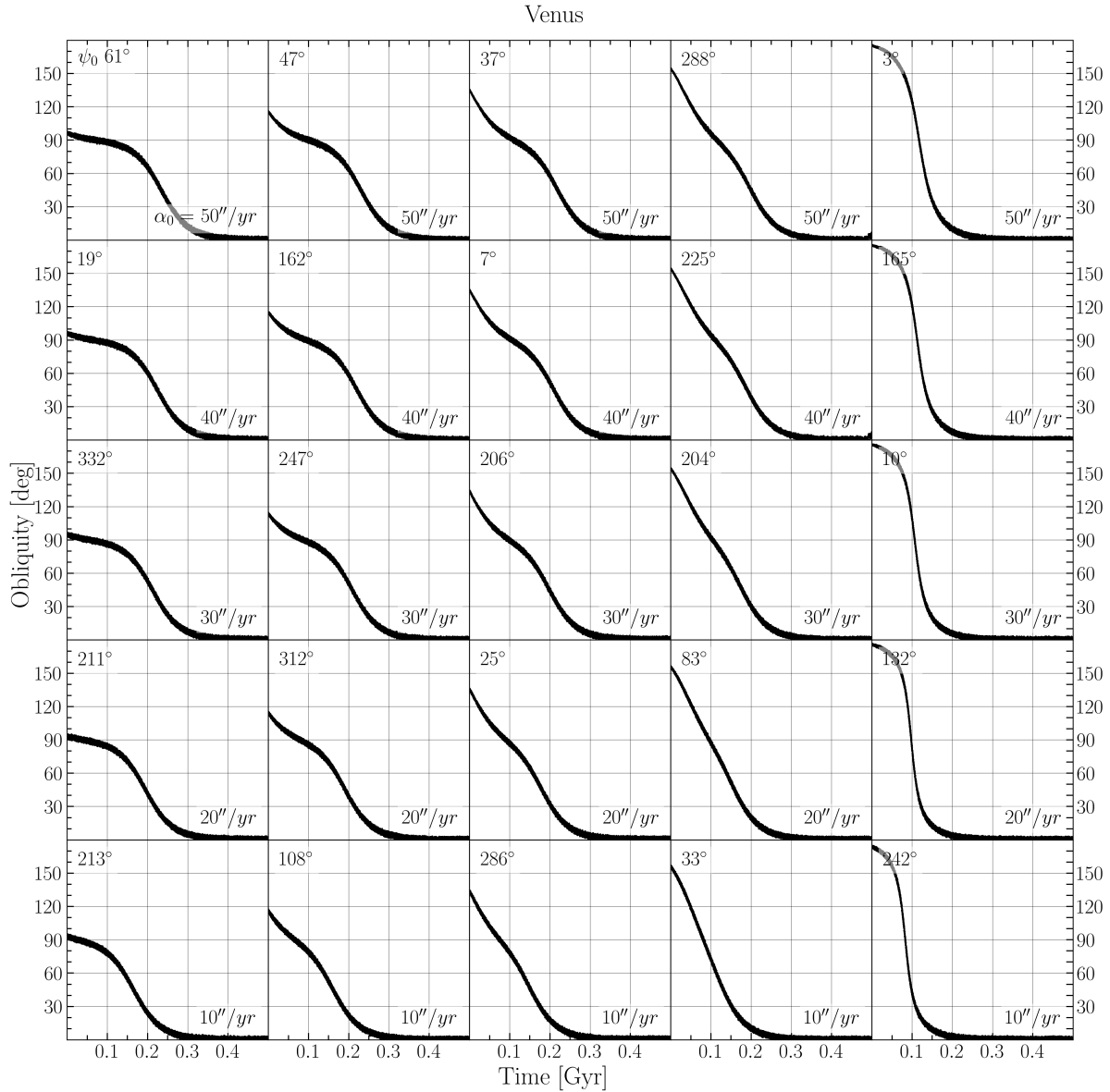
Figure 4.10 I show the tidal obliquity evolution as a function of time similar to Figure 4.4, but for the retrograde Venus simulation batch featured in Figure 4.9.

shifts in obliquity occur on the scale of millions to tens of millions of years were often an eventuality due to the extent of the Solar System's chaotic resonance zones. Earthmoo and Venus especially suffered significant obliquity variations for cases of low to moderate initial obliquities and for faster initial spin-precession rates. Fully considering the prospects of habitability of such states is outside of the scope of this study, but I speculate that such severe obliquity variations would likely be detrimental to the stability of their climate and development of life.

A subset of my simulations suggest that there are some initial conditions that result in mild obliquity variations which reinforces the idea that the Earth can be obliquity stable without the Moon and that an early Venus could have had desirable prospects for habitability. For instance, both Earthmoo and Venus enjoyed a brief initial respite when starting with a combination of low initial obliquity and high initial precession constant before tidal braking ultimately dragged them through chaotic frequency space. Additionally, I saw several instances of resonance capture in which a planet was transported in libration about a strong resonance appeared to offer a form of stability while its rotation slowed. Importantly, cases in which both Earthmoo and Venus had initial obliquities near $90°$ were especially obliquity stable during the initial spin dampening phase, while retrograde rotation generally meant constrained short-term obliquity variations due to the sparse presence of retrograde resonances to interact with. Although high obliquity could potentially be harmful toward planetary habitability due to the stark contrast in seasons as each pole alternates between extremes of incident solar flux, previous work suggests that high obliquity generally produces warmer climates (Kang, 2019) and can help to stave off snowball states (Spiegl *et al.*, 2015; Colose *et al.*, 2019), however see He *et al.* (2022).

For future work, it would be interesting to revisit the case of a moonless Earth and early Venus by considering the true, slower rate of tidal braking, in order to more realistically study those scenarios and gain a statistical sense for habitably favorable scenarios. However, the trends in obliquity evolution that I note in this study are still realistic for these two bodies. Performing simulations of this nature with SMERCURY-T would require a substantially longer amount of computation time, but would only need to provide have a long enough look on the billion year time scale to study the consequences for habitability. In the consideration of exoplanets we can apply the lessons that we have learned here toward judgement of their habitability once we gain the capability to characterize their spin states and frequency environment. We can expect that each planetary system's unique orbital architecture would produce vastly different spin-orbit resonance frequency environments than for the planets in the Solar System, where more "dynamically hot" systems could spell trouble for retrograde rotators. Ultimately, tidal obliquity evolution is an important process to

factor into the assessment of habitability but its importance is likely dependent on a case by case basis that requires the consideration of planetary and system properties.

CHAPTER 5

GENERAL CONCLUSION

This dissertation is comprised of three individual studies that together serve to help build a more complete understanding of planetary obliquity evolution in the context of habitability. Within Chapter 2, I employ numerical experiments to study a secular spin-orbit resonance enabled by planetary eccentricity that can excite significant obliquity variations for retrograde-rotating planets. In Chapter 3, I introduce SMERCURY-T, an N-body integrator capable of simulating tidal obliquity evolution for planets in complex systems and demonstrate spin-orbit resonance encounter scenarios as a result of tidal braking. Finally, in Chapter 4 I apply SMERCURY-T to the useful cases of a moonless Earth and early Venus in order to study how tidal obliquity evolution plays out in multi-planet systems with complex frequency environments.

Each of the studies within this dissertation provided additional value and made wider contributions to the field past their individual results and findings. The work within Chapter 2 importantly raised awareness and stressed the need to consider retrograde obliquities within the considered parameter space of obliquity studies, as often only prograde obliquities are. While I identified and explored one particular retrograde spin-orbit resonance, future studies could explore the mechanisms driving additional retrograde spin-orbit resonances enabled by orbital eccentricity that may potentially be important for the spin dynamics of eccentric exoplanets. The development of SMERCURY-T in Chapter 3 was not only useful for my subsequent exploration in Chapter 4, but was also made publicly available so that other studies may apply it to new investigations. This chapter also procedurally presented simple secular spin-orbit resonance encounters triggered by the tidal spin torque in order to better educate the community on what are likely common processes in more compact exoplanetary systems where tides are especially important. Although the work in Chapter 4 explored specific cases of tidal obliquity evolution in the Solar System, the findings of the experiments within identified general trends and behaviors on what we could expect for potentially habitable exoplanets in complex multi-planet

systems. For this study in addition to those within the previous two chapters, the lessons learned for what conditions or processes lead to stable or unstable obliquity variations may one day be useful references for the judgement of exoplanet habitability once their obliquities might be measured and characterized.

Ideally, the knowledge gained in this dissertation as well as from numerous other obliquity studies could be applied to real exoplanetary systems in the future. Knowledge of system and planetary properties could quickly be referenced and compared to analytical and numerical findings like this work which reveal specific processes and trends that may be relevant to that particular system. However, to date, we have not yet been able to directly measure the obliquity of an exoplanet. There are several methodologies that have been proposed to do so, including: constraining obliquity by measuring planetary oblateness and rotation period from transit photometry (Barnes and Fortney, 2003), inferring obliquity from seasonal differences in infrared light curves (Gaidos and Williams, 2004), obtaining obliquity by looking for geometric effects of directly imaged exoplanets (Kawahara, 2016), and others. Although it was likely a brown dwarf companion in orbit around an M dwarf star, a recent study actually managed to loosely constrain the brown dwarf's obliquity (Bryan *et al.*, 2020). It is only a matter of time before we gain the capability to do so for exoplanets with future technological advances, where we can then apply what we have learned to make judgements on their habitability based on their obliquity evolution.

Bibliography

Alexander M.E. 1973. The Weak Friction Approximation and Tidal Evolution in Close Binary Systems. Astrophysics and Space Science 23:459–510.

Armstrong J., Barnes R., Domagal-Goldman S., Breiner J., Quinn T., and Meadows V. 2014. Effects of extreme obliquity variations on the habitability of exoplanets. Astrobiology 14:277–291, pMID: 24611714.

Barnes J.W. and Fortney J.J. 2003. Measuring the oblateness and rotation of transiting extrasolar giant planets. The Astrophysical Journal 588:545–556.

Barnes J.W., Quarles B., Lissauer J.J., Chambers J., and Hedman M.M. 2016. Obliquity variability of a potentially habitable early venus. Astrobiology 16:487–499, pMID: 27328026.

Barnes R., Luger R., Deitrick R., Driscoll P., Quinn T.R., Fleming D.P., Smotherman H., McDonald D.V., Wilhelm C., Garcia R., Barth P., Guyer B., Meadows V.S., Bitz C.M., Gupta P., Domagal-Goldman S.D., and Armstrong J. 2020. VPLanet: The virtual planet simulator. Publications of the Astronomical Society of the Pacific 132:024502.

Barnett M.N. and Olson S.L. 2022. Moderately high obliquity promotes biospheric oxygenation. The Planetary Science Journal 3:132.

Blanco-Cuaresma S. and Bolmont E. 2017. Studying Tidal Effects In Planetary Systems With Posidonius. A N-Body Simulator Written In Rust. *In* EWASS Special Session 4 (2017): Star-planet interactions (EWASS-SS4-2017).

Bolmont E., Libert A.S., Leconte J., and Selsis F. 2016. Habitability of planets on eccentric orbits: Limits of the mean flux approximation. Astronomy & Astrophysics 591:A106.

Bolmont E., Raymond S.N., Leconte J., Hersant F., and Correia A.C.M. 2015. Mercury-t: A new code to study tidally evolving multi-planet systems. applications to kepler-62. Astronomy % Astrophysics 583:A116.

Brasser R. and Lee M.H. 2015. Tilting Saturn without Tilting Jupiter: Constraints on Giant Planet Migration. The Astronomical Journal 150:157.

Brasser R. and Walsh K.J. 2011. Stability analysis of the martian obliquity during the noachian era. Icarus 213:423–427.

Bryan M.L., Chiang E., Bowler B.P., Morley C.V., Millholland S., Blunt S., Ashok K.B., Nielsen E., Ngo H., Mawet D., and Knutson H.A. 2020. Obliquity constraints on an extrasolar planetary-mass companion. The Astronomical Journal 159:181.

Cardano G. 1993. Ars magna or the rules of algebra. New York, Dover Publications.

Chambers J.E. 1999. A hybrid symplectic integrator that permits close encounters between massive bodies. Monthly Notices of the Royal Astronomical Society 304:793–799.

Colombo G. 1966. Cassini's Second and Third Laws. SAO Special Report 203.

Colose C.M., Genio A.D.D., and Way M.J. 2019. Enhanced habitability on high obliquity bodies near the outer edge of the habitable zone of sun-like stars. The Astrophysical Journal 884:138.

Deitrick R., Barnes R., Bitz C., Fleming D., Charnay B., Meadows V., Wilhelm C., Armstrong J., and Quinn T.R. 2018b. Exo-milankovitch cycles. II. climates of g-dwarf planets in dynamically hot systems. The Astronomical Journal 155:266.

Deitrick R., Barnes R., Quinn T.R., Armstrong J., Charnay B., and Wilhelm C. 2018a. Exo-milankovitch cycles. i. orbits and rotation states. The Astronomical Journal 155:60.

Dones L. and Tremaine S. 1993. On the origin of planetary spins. Icarus 103:67–92.

Dong C., Huang Z., and Lingam M. 2019. Role of planetary obliquity in regulating atmospheric escape: G-dwarf versus m-dwarf earth-like exoplanets. The Astrophysical Journal 882:L16.

Dressing C.D., Spiegel D.S., Scharf C.A., Menou K., and Raymond S.N. 2010. HAB-ITABLE CLIMATES: THE INFLUENCE OF ECCENTRICITY. The Astrophysical Journal 721:1295–1307.

Eggleton P.P., Kiseleva L.G., and Hut P. 1998. The Equilibrium Tide Model for Tidal Friction. The Astrophysical Journal 499:853–870.

Einstein A. 1916. Die grundlage der allgemeinen relativitätstheorie. Annalen der Physik 354:769–822.

Forget F., Wordsworth R., Millour E., Madeleine J.B., Kerber L., Leconte J., Marcq E., and Haberle R.M. 2013. 3D modelling of the early martian climate under a denser CO_2 atmosphere: Temperatures and CO_2 ice clouds. Icarus 222:81–99.

Gaidos E. and Williams D. 2004. Seasonality on terrestrial extrasolar planets: inferring obliquity and surface conditions from infrared light curves. New Astronomy 10:67 − 77.

Guendelman I. and Kaspi Y. 2019. Atmospheric dynamics on terrestrial planets: The seasonal response to changes in orbital, rotational, and radiative timescales. The Astrophysical Journal 881:67.

Hamilton D.P. and Ward W.R. 2004. Tilting saturn. II. numerical model. The Astronomical Journal 128:2510–2517.

He F., Merrelli A., L'Ecuyer T.S., and Turnbull M.C. 2022. Climate outcomes of earth-similar worlds as a function of obliquity and rotation rate. The Astrophysical Journal 933:62.

Head J., Mustard J., Kreslavsky M., Milliken R., and Marchant D. 2004. Recent ice ages on mars. Nature 426:797–802.

Head J.W., Neukum G., Jaumann R., Hiesinger H., Hauber E., Carr M., Masson P., Foing B., Hoffmann H., Kreslavsky M., Werner S., Milkovich S., van Gasselt S., and HRSC Co-Investigator Team. 2005. Tropical to mid-latitude snow and ice accumulation, flow and glaciation on Mars. Nature 434:346–351.

Henrard J. 1982. Capture into resonance-an extension of the use of adiabatic invariants. Celestial mechanics 27:3–22.

Henrard J. and Murigande C. 1987. Colombo's top. Celestial Mechanics 40:345–366.

Hoffman P.F., Kaufman A.J., Halverson G.P., and Schrag D.P. 1998. A neoproterozoic snowball earth. Science 281:13421346.

Hubbard W.B. 1984. Planetary Interiors. New York, Van Nostrand Reinhold Co.

Hut P. 1981. Tidal evolution in close binary systems. Astronomy & Astrophysics 99:126–140.

Kane S.R. and Torres S.M. 2017. Obliquity and eccentricity constraints for terrestrial exoplanets. The Astronomical Journal 154:204.

Kang W. 2019. Mechanisms leading to a warmer climate on high-obliquity planets. The Astrophysical Journal 876:L1.

Kawahara H. 2016. FREQUENCY MODULATION OF DIRECTLY IMAGED EXO-PLANETS: GEOMETRIC EFFECT AS a PROBE OF PLANETARY OBLIQUITY. The Astrophysical Journal 822:112.

Kilic C., Lunkeit F., Raible C.C., and Stocker T.F. 2018. Stable equatorial ice belts at high obliquity in a coupled atmosphere–ocean model. The Astrophysical Journal 864:106.

Kilic C., Raible C.C., and Stocker T.F. 2017. Multiple climate states of habitable exoplanets: The role of obliquity and irradiance. The Astrophysical Journal 844:147.

Kreyche S.M., Barnes J.W., Quarles B.L., and Chambers J.E. 2021a. Smkreyche/smercury-t: First release of smercury-t.

Kreyche S.M., Barnes J.W., Quarles B.L., and Chambers J.E. 2021b. Exploring tidal obliquity variations with SMERCURY-t. The Planetary Science Journal 2:187.

Kreyche S.M., Barnes J.W., Quarles B.L., Lissauer J.J., Chambers J.E., and Hedman M.M. 2020. Retrograde-rotating exoplanets experience obliquity excitations in an eccentricity-enabled resonance. The Planetary Science Journal 1:8.

Laskar J., Correia A., Gastineau M., Joutel F., Levrard B., and Robutel P. 2004b. Long term evolution and chaotic diffusion of the insolation quantities of mars. Icarus 170:343–364.

Laskar J., Joutel F., and Boudin F. 1993a. Orbital, precessional, and insolation quantities for the earth from -20 Myr to +10 Myr. Astronomy & Astrophysics 270:522–533.

Laskar J. and Robutel P. 1993b. The chaotic obliquity of the planets. Nature 361:608.

Laskar J., Robutel P., Joutel F., Gastineau M., Correia A.C.M., and Levrard B. 2004a. A long-term numerical solution for the insolation quantities of the earth. Astronomy & Astrophysics 428:261–285.

Leconte J., Chabrier G., Baraffe I., and Levrard B. 2010. Is tidal heating sufficient to explain bloated exoplanets? Consistent calculations accounting for finite initial eccentricity. Astronomy & Astrophysics 516:A64.

Li G. and Batygin K. 2014. On the spin-axis dynamics of a moonless earth. The Astrophysical Journal 790:69.

Lissauer J.J., Barnes J.W., and Chambers J.E. 2012. Obliquity variations of a moonless earth. Icarus 217:77 – 87.

Lissauer J.J., Berman A.F., Greenzweig Y., and Kary D.M. 1997. Accretion of mass and spin angular momentum by a planet on an eccentric orbit. Icarus 127:65–92.

Lissauer J.J. and Kary D.M. 1991. The origin of the systematic component of planetary rotation: I. planet on a circular orbit. Icarus 94:126 – 159.

Mardling R.A. and Lin D.N.C. 2004. On the survival of short-period terrestrial planets. The Astrophysical Journal 614:955–959.

Méndez A. and Rivera-Valentín E.G. 2017. The equilibrium temperature of planets in elliptical orbits. The Astrophysical Journal 837:L1.

Mignard F. 1979. The Evolution of the Lunar Orbit Revisited. I. Moon and Planets 20:301–315.

Miguel Y. and Brunini A. 2010. Planet formation: statistics of spin rates and obliquities of extrasolar planets. Monthly Notices of the Royal Astronomical Society 406:1935–1943.

Milanković M. 1998. Canon of Insolation and the Ice-Age Problem. Belgrade, Textbook Publishing Company.

Millholland S. and Batygin K. 2019. Excitation of planetary obliquities through planet–disk interactions. The Astrophysical Journal 876:119.

Millholland S. and Laughlin G. 2019. Obliquity-driven sculpting of exoplanetary systems. Nature Astronomy 3:424–433.

Muller R.A. and MacDonald G.J. 1995. Glacial cycles and orbital inclination. Nature 377:107–108.

Murray C.D. and Dermott S.F. 1999. Solar System Dynamics. Cambridge University Press.

Neron de Surgy O. and Laskar J. 1997a. On the long term evolution of the spin of the Earth. Astronomy & Astrophysics 318:975–989.

Neron de Surgy O. and Laskar J. 1997b. On the long term evolution of the spin of the Earth. Astronomy & Astrophysics 318:975–989.

Olson S.L., Jansen M., and Abbot D.S. 2020. Oceanographic considerations for exoplanet life detection. The Astrophysical Journal 895:19.

Park R.S., Folkner W.M., Konopliv A.S., Williams J.G., Smith D.E., and Zuber M.T. 2017. Precession of mercury's perihelion from ranging to the messenger spacecraft. The Astronomical Journal 153:121.

Peale S.J. 1969. Generalized Cassini's Laws. The Astronomical Journal 74:483.

Quarles B., Barnes J.W., Lissauer J.J., and Chambers J. 2020. Obliquity evolution of the potentially habitable exoplanet kepler-62f. Astrobiology 20:73–90, pMID: 31613645.

Quarles B., Li G., and Lissauer J.J. 2019. Obliquity evolution of circumstellar planets in sun-like stellar binaries. The Astrophysical Journal 886:56.

Rodríguez, A. and Ferraz-Mello, S. 2010. Tidal decay and circularization of the orbits of short-period planets. EAS Publications Series 42:411–418.

Rogoszinski Z. and Hamilton D.P. 2020. Tilting ice giants with a spin–orbit resonance. The Astrophysical Journal 888:60.

Saillenfest M., Lari G., and Boué G. 2021a. The large obliquity of saturn explained by the fast migration of titan. Nature Astronomy pages 1–5.

Saillenfest M., Lari G., and Courtot A. 2020. The future large obliquity of jupiter. Astronomy % Astrophysics 640:A11.

Saillenfest M., Laskar J., and Boué G. 2019. Secular spin-axis dynamics of exoplanets. Astronomy % Astrophysics 623:A4.

Saillenfest, Melaine, Lari, Giacomo, Boué, Gwenaël, and Courtot, Ariane. 2021. The past and future obliquity of saturn as titan migrates. Astronomy % Astrophysics 647:A92.

Šidlichovský M. and Nesvorný D. 1996. Frequency modified fourier transform and its application to asteroids. Celestrial Mechanics and Dynamical Astronomy 65:137.

Spiegl T., Paeth H., and Frimmel H. 2015. Evaluating key parameters for the initiation of a neoproterozoic snowball earth with a single earth system model of intermediate complexity. Earth and Planetary Science Letters 415:100–110.

Su Y. and Lai D. 2020. Dynamics of colombo's top: Generating exoplanet obliquities from planet–disk interactions. The Astrophysical Journal 903:7.

Touma J. and Wisdom J. 1993. The chaotic obliquity of mars. Science 259:1294–1297.

Touma J. and Wisdom J. 1994. Lie-Poisson Integrators for Rigid Body Dynamics in the Solar System. The Astronomical Journal 107:1189.

van den Heuvel E.P.J. 1966. On the Precession as a Cause of Pleistocene Variations of the Atlantic Ocean Water Temperatures. Geophysical Journal International 11:323–336.

Vokrouhlický D. and Nesvorný D. 2015. Tilting jupiter (a bit) and saturn (a lot) during planetary migration. The Astrophysical Journal 806:143.

Ward W.R. and Hamilton D.P. 2004. Tilting saturn. i. analytic model. The Astronomical Journal 128:2501–2509.

Way M.J. and Georgakarakos N. 2017. Effects of variable eccentricity on the climate of an earth-like world. The Astrophysical Journal 835:L1.

Williams D.M. and Kasting J.F. 1997. Habitable planets with high obliquities. Icarus 129:254–267.

Williams D.M. and Pollard D. 2002. Earth-like worlds on eccentric orbits: excursions beyond the habitable zone. International Journal of Astrobiology 1:61–69.

Williams D.M. and Pollard D. 2003. Extraordinary climates of earth-like planets: three-dimensional climate simulations at extreme obliquity. International Journal of Astrobiology 2:1–19.

APPENDIX A

Supplementary Information to Chapter 3

A.1 SCHEME TO UPDATE PLANETARY RADIUS AND J_2

The inclusion of the tidal spin torque module that we discuss in Section 3.4.2 calls for the need to update the values of the spin-tracked planet's equatorial radius, R, and zonal gravity coefficient, J_2, at each time step within a SMERCURY-T simulation (or at an interval set by the "tidal tolerance" parameter). This is necessary because the effects of the tidal torque on the planet's equatorial bulge cause its spin rate, and therefore its equatorial radius and J_2, to decay over time. These parameters are critical for SMERCURY-T to compute the magnitude of the tidal torque following Equation 3.4 as well as to populate the planet's inertia tensor for the N-body torque calculations following Lissauer *et al.* (2012).

Sticking with the rigid body considerations described in Section 3.4.1, we begin an expression for the planet's equatorial radius (like that of Equation 3.3) as

$$R^3 = \frac{Gm_p D}{\omega_p^2} \left(\frac{2 - \sqrt{4 - \frac{30\omega_p^2}{GD\pi\rho}}}{10} \right) \tag{A.1}$$

where m_p, ω_p, and ρ are the planet's mass, spin rate, and average density, respectively. Here G is the universal gravitational constant and

$$D = \frac{25}{4} \left(\frac{3}{2}\overline{C} - 1 \right)^2 + 1 \tag{A.2}$$

where $\overline{C}$ is the planet's normalized polar moment of inertia. Now, we can shuffle the equation $S = I_p \omega_p$ for the planet's rotational angular momentum to get

$$\omega_p = \frac{S}{I_p} = \frac{S}{\overline{C}m_p R^2} \tag{A.3}$$

Here S is the magnitude of the planet's spin angular momentum and I_p its moment of inertia. We plug Equation A.3 into Equation A.1 to work toward a solution for R. This gives

$$R^3 = \frac{Gm_p{}^3 D\overline{C}^2 R^4}{S^2} \left(\frac{2 - \sqrt{4 - \frac{30S^2}{Gm_p{}^2 D\overline{C}^2 \pi \rho R^4}}}{10} \right) \quad \text{(A.4)}$$

Shifting some things around, squaring both sides, and isolating the R terms to one side yields:

$$-\frac{40S^2}{Gm_p{}^3 D\overline{C}^2}R^3 + \frac{100S^4}{G^2 m_p{}^6 D^2 \overline{C}^4}R^2 + \frac{30S^2}{Gm_p{}^2 D\overline{C}^2 \pi \rho} = 0 \quad \text{(A.5)}$$

This reduces to

$$-\frac{4}{m_p}R^3 + \frac{10S^2}{Gm_p{}^4 D\overline{C}^2}R^2 + \frac{3}{\pi \rho} = 0 \quad \text{(A.6)}$$

This equation takes the form $ax^3 + bx^2 + cx + d = 0$, for which we solve for R with the use of Cardano's general cubic formula (Cardano, 1993). We obtain the corresponding value of ω_p by plugging the solution for R back into Equation A.3. Finally, we calculate the planet's J_2 with Equation 3.1.